UNIVERSITY OF ALBERTA

Numerical Simulation of Moisture Movement, Anaerobic Biodegradation, and Dissolved Organic Carbon Transport in Municipal Solid Waste

BY

Robert Brent Mooder

©

A thesis submitted to the Faculty of Graduate Studies and Research in partial fulfillment of the requirements for the degree of Master of Science.

DEPARTMENT OF EARTH AND ATMOSPHERIC SCIENCES

Edmonton, Alberta
Fall 1998

National Library of Canada
Acquisitions and Bibliographic Services
395 Wellington Street
Ottawa ON K1A 0N4
Canada

Bibliothèque nationale du Canada
Acquisitions et services bibliographiques
395, rue Wellington
Ottawa ON K1A 0N4
Canada

Your file Votre référence

Our file Notre référence

The author has granted a non-exclusive licence allowing the National Library of Canada to reproduce, loan, distribute or sell copies of this thesis in microform, paper or electronic formats.

The author retains ownership of the copyright in this thesis. Neither the thesis nor substantial extracts from it may be printed or otherwise reproduced without the author's permission.

L'auteur a accordé une licence non exclusive permettant à la Bibliothèque nationale du Canada de reproduire, prêter, distribuer ou vendre des copies de cette thèse sous la forme de microfiche/film, de reproduction sur papier ou sur format électronique.

L'auteur conserve la propriété du droit d'auteur qui protège cette thèse. Ni la thèse ni des extraits substantiels de celle-ci ne doivent être imprimés ou autrement reproduits sans son autorisation.

0-612-34394-4

Canada

UNIVERSITY OF ALBERTA

FACULTY OF GRADUATE STUDIES AND RESEARCH

The undersigned certify that they have read, and recommend to the Faculty of Graduate Studies and Research for acceptance, a thesis entitled **Numerical Simulation of Moisture Movement, Anaerobic Biodegradation, and Dissolved Organic Carbon Transport in Municipal Solid Waste** submitted by Robert Brent Mooder in partial fulfillment of the requirements for the degree of Master of Science.

Dr. C. A. Mendoza (Supervisor)

Dr. C. A. Zeiss (External)

Dr. A. B. G. Bush (Examiner)

Dr. K. Muehlenbachs (Examiner)

Dr. K. Muehlenbachs (Chair)

Date: Aug 24/98

Abstract

A landfill site is a complex environment characterized by many interacting physical, chemical, and biological processes. This thesis presents a new two-dimensional numerical model, called C-Flow, that simulates variably-saturated, transient moisture movement, anaerobic biodegradation, advective-dispersive dissolved organic carbon (DOC) transport, and gas generation in municipal solid waste (MSW). The model represents MSW as a combination of loose waste and refuse contained in semi-intact garbage bags. Darcy's Law governs moisture movement through the loose waste. Capillary-pressure gradients control moisture redistribution within the refuse-filled garbage bags, which are represented by isolated porous spheres. First-order fluid and mass transfer coefficients couple the two domains.

Numerical simulation results compare well with observations from a previous dumpster-scale experiment. Rapid flow through the loose waste and gradual water transfer into the garbage bags characterizes the moisture movement. Moisture movement is sensitive to water application rate and waste compaction. Results from a sensitivity analysis show that different sets of physical parameters represent the experimental observations equally well.

An example model application illustrates waste biodegradation at the landfill scale. Simulated biodegradation rates are unrealistically insensitive to different leachate pumping and recirculation schemes. These results demonstrate the need for further model development supported by experimental studies at a variety of scales. A second example illustrates groundwater contamination caused by an unlined landfill site. The simulated DOC concentrations within the landfill follow a realistic trend.

A DOC plume persists for more than one hundred years, although the concentrations within the aquifer remain reasonably low.

For my parents,
Norma J. Mooder
and
George A. Mooder

Acknowledgements

First, and most importantly, I thank my supervisor. Carl, you have been an amazing supervisor and a great friend. You are a superb mentor. You have always been enthusiastic about my research and encouraged me to pursue my many (some might say too many) tangential ideas. You gave me the freedom to explore my own ideas and the guidance to have them bear fruit. Thank you.

I thank the Department of Earth and Atmospheric Sciences and the University of Alberta for their support through teaching and research assistantships, as well as scholarships. I also appreciate the funding I received through Carl Mendoza's NSERC award. Thanks also to my instructors, especially Joe Tóth, who has always willingly shared his wisdom.

I need to thank my friends and office cohorts at the U of A. Leroy, István, Adam, and Tannis have all made my time here more enjoyable. Thank you Sheri for gracing me with your stellar wit and charm. You and Leroy gave me hope that finishing was possible. Darlene, you are a great friend. You showed me the perils of trying to finish up while working full time (but did I listen? No.). Melody. What can I say? There is never a dull moment when you are around.

My friends have filled my time at school with far too much revelry. The residents of the evil house gave me the best introduction to Edmonton life that a person could ask for. Ampersand gave me my first chance ever to be a groupie. Wingnut, you kick ass. Jeff, JVH, Pat, Eric, and Autumn, you are all good paddling buddies and great friends. I look forward to our further adventures. Mandy and Joshua, your generosity, support, and friendship are wonderful. Thank you all.

My family has bathed me with love since before I remember. Sue, Doug, Cheryl, Dale, Tracey, Krista, Katie, and Christina, I love you all. Sue, Carl, Cam, and Lexi, you are my Edmonton family. You have helped make Alberta home. Mom and dad, thank you for teaching me to pursue whatever made me happy. You are the best parents anyone could hope for. Mom, we are all sad that you had to leave us this year. This thesis is for you and dad. The two of you made me who I am. Thank you.

Finally, I thank you Karen. You have supported me through all the turmoil of the last two years. I am always amazed at your willingness to listen to me babble on about my latest minor triumph and grateful for your support when life gets rough. Your strength and love amaze me. I love you Karen, and I look forward to our life together.

Contents

1 Introduction 1

2 Theory 4

2.1 Conceptual Models 4

2.1.1 Gas Flow 6

2.1.2 Water Flow 7

2.1.3 Biodegradation 7

2.1.4 Transport 10

2.2 Mathematical Models 11

2.2.1 Moisture Flow 11

2.2.2 Carbon Transformations 22

2.2.3 Aqueous-Phase Transport 26

3 Numerical Implementation 30

3.1 Domain Discretization 30

3.1.1 Primary Domain 30

3.1.2 Secondary Domain 32

3.1.3 Interdomain Coupling 32

3.1.4 Time 33

3.2 Moisture Flow 34

3.2.1 Solution Procedure 36

3.2.2 Fluid Balance 37

3.3 Carbon Transformations 38

3.4 Aqueous-Phase Carbon Transport 39
3.4.1 Solution Procedure 40
3.4.2 Mass Balance 40
3.4.3 Accuracy Criteria 41
3.5 Verification Problems 42
3.5.1 Moisture Movement 42
3.5.2 Reactive Transport 49

4 Experimental Application **55**
4.1 Physical Scenario 55
4.2 Preliminary Observations 56
4.3 Conceptual Model 59
4.4 Modeling Approach 59
4.5 Initial and Boundary Conditions 60
4.6 Domain Discretization 61
4.7 Results 62
4.7.1 Hydraulic Parameters 62
4.7.2 Simulation Results 64
4.8 Discussion 65
4.8.1 Fluid Transfer 70
4.8.2 Waste Compaction 70
4.9 Sensitivity Analysis 71
4.9.1 Waste Density 72
4.9.2 Mode of Water Transfer 75
4.9.3 Matrix Pore-Size Distribution 77
4.9.4 Uniform Infiltration Rate 77
4.9.5 Matrix Accessibility 79
4.10 Summary 80

5 Illustrative Examples **82**

5.1 Landfill-Scale Application 82

5.1.1 Domain Definition 83

5.1.2 Waste Properties 84

5.1.3 Flow Boundary Conditions 84

5.1.4 Transport Boundary and Initial Conditions 87

5.1.5 Simulation Results 88

5.1.6 Discussion 93

5.2 Regional-Scale Application 94

5.2.1 Flow Boundary Conditions 96

5.2.2 Transport Boundary and Initial Conditions 97

5.2.3 Simulation Results 97

5.2.4 Mass Fate 98

5.3 Summary 100

6 Conclusions **103**

A Finite-Element Formulation **109**

A.1 Primary Domain 109

A.1.1 Flow Elemental Matrices 109

A.1.2 Flow Solution Iteration 111

A.1.3 Transport Elemental Matrices 113

A.2 Secondary Domain 115

A.2.1 Flow Elemental Matrices 115

A.2.2 Transport Elemental Matrices 117

References **118**

List of Figures

2.1 Conceptual model of overall landfill site behaviour 5
2.2 Conceptual model of small-scale municipal solid waste behaviour . . . 5
2.3 Conceptual model of anaerobic waste biodegradation 9
2.4 Schematic bounding curves for the capillary pressure–water saturation envelope 18
2.5 Simplified model of anaerobic waste biodegradation 22

3.1 Cartesian coordinate system 31
3.2 Cylindrical coordinate system 31
3.3 Finite elements used for domain discretization 31
3.4 Spherical coordinate system 32
3.5 Comparison of C-Flow results to the Theis (1935) solution 44
3.6 Comparison of C-Flow results to the Neuman (1974) solution 45
3.7 Comparison of C-Flow results to the Moench (1984) solution 46
3.8 Comparison of C-Flow results to FRAC3DVS 48
3.9 Position of the water-table in a draining block as predicted by C-Flow 49
3.10 Comparison of C-Flow results to the van Genuchten (1981) solution . 51
3.11 C-Flow results for the strip source problem at two times 53
3.12 Comparison of C-Flow results to the strip source solution 53
3.13 Comparison of C-Flow results to the analytical solution for transient mass transfer to a sphere 54

4.1 Relationship between water application rate and bulk downward velocity for the dumpster-scale water flow experiments 58
4.2 Comparison of numerical and experimental results for the uncompacted, low infiltration rate cells 66
4.3 Comparison of numerical and experimental results for the compacted, low infiltration rate cells 67
4.4 Comparison of numerical and experimental results for the uncompacted, high infiltration rate cells 68
4.5 Comparison of numerical and experimental results for the compacted, high infiltration rate cells 69
4.6 Sensitivity of the numerical results to differences in waste density . . 74
4.7 Sensitivity of the numerical results to changes in matrix pore-size distribution 76
4.8 Sensitivity of the numerical results to the water-application boundary representation 78

5.1 Annual profiles of DOC versus z during the waste accretion period . . 89
5.2 DOC concentration as a function of time since waste emplacement at the midpoint of each annual waste layer 90
5.3 Profiles of DOC concentration versus z during the stabilization period for all four stabilization scenarios 91
5.4 DOC concentration in the bottom waste layer at a radius of 5.7 m as a function of time for all four waste stabilization scenarios 92
5.5 DOC concentration as a function of time for the pumping and no infiltration stabilization scenarios 92
5.6 Hydraulic head distribution for the regional-scale illustrative example 96
5.7 DOC concentrations for the regional-scale example 99
5.8 DOC concentration within the landfill site versus time 100
5.9 DOC discharge rate to the upper lake as a function of time 101

List of Tables

2.1 Selected physical properties of alcohols and organic acids 11

3.1 Parameters used for the moisture flow model verification problems . . 43
3.2 Spatial and temporal discretization used for the moisture flow model verification problems 43
3.3 Parameters used for the reactive transport model verification problems 50
3.4 Spatial and temporal discretization used for the reactive transport model verification problems 50

4.1 Selected data from the dumpster-scale water flow experiments used to constrain the numerical simulations 58
4.2 Summary of parameters used for numerical simulation of the dumpster-scale unsaturated flow experiments 63
4.3 Comparison of simulated and experimental results 65
4.4 Summary of parameters used for the sensitivity analysis of the dumpster-scale unsaturated flow experiments 73

5.1 Summary of parameters used for the landfill-scale illustrative example 85
5.2 Summary of biodegradation parameters from the literature 86
5.3 Comparison of solids consumption and biomass production for the four stabilization scenarios after seven years of waste stabilization 93
5.4 Summary of parameters for the regional-scale illustrative example . . 95

Notation

General

$(\,)'$	[-]	secondary domain
$(\,)_0$	[-]	initial condition
$(\,)_\Gamma$	[-]	boundary condition
g	[LT^{-2}]	acceleration due to gravity
r	[L]	horizontal radial coordinate direction
s	[L]	general coordinate direction
t	[T]	time
x	[L]	horizontal Cartesian coordinate direction
z	[L]	vertical coordinate direction
Γ	[-]	domain boundary
Γ_1	[-]	a portion of the domain boundary
Γ_2	[-]	a portion of the domain boundary
Γ_3	[-]	a portion of the domain boundary
δ_{ij}	[-]	the Kronecker delta
θ	[-]	porosity
ϕ	[-]	angular coordinate direction
φ	[-]	angular coordinate direction

Moisture Flow

F_t	$[T^{-1}]$	fluid transfer coefficient
h	[L]	hydraulic head
k	$[L^2]$	intrinsic permeability
k_r	[-]	relative permeability
K_{ij}	$[LT^{-1}]$	hydraulic conductivity tensor
m	[-]	van Genuchten shape parameter
n	[-]	van Genuchten shape parameter
P	$[ML^{-1}T^{-2}]$	water pressure
P_0	$[ML^{-1}T^{-2}]$	reference water pressure
P_a	$[ML^{-1}T^{-2}]$	air pressure
q	$[LT^{-1}]$	volumetric moisture flux
q^*	$[T^{-1}]$	volumetric fluid source term
S_s	$[L^{-1}]$	specific storage
S_e	[-]	effective water saturation
S_r	[-]	residual water saturation
S_w	[-]	water saturation
α	$[L^{-1}]$	van Genuchten soil parameter
α	$[LT^2M^{-1}]$	porous medium compressibility (Section 1.1 only)
β	$[LT^2M^{-1}]$	water compressibility
θ_w	[-]	volumetric moisture content
λ	[-]	Brooks-Corey pore-size distribution index
μ_w	$[ML^{-1}T^{-1}]$	viscosity of water
ρ_b	$[ML^{-3}]$	waste dry bulk density
ρ_w	$[ML^{-3}]$	water density
ψ	[L]	pressure head
ψ_c	[L]	capillary pressure head
ψ_d	[L]	Brooks-Corey displacement capillary pressure head

B_a	$[ML^{-3}]$	accessible biodegradable solid carbon concentration
B_p	$[ML^{-3}]$	protected biodegradable solid carbon concentration
C	$[ML^{-3}]$	dissolved organic carbon concentration
D_{ij}	$[L^2T^{-1}]$	hydrodynamic aqueous dispersion tensor
D_w	$[L^2T^{-1}]$	free-solution aqueous diffusion coefficient
G_I	$[ML^{-3}]$	carbon dioxide concentration
G_O	$[ML^{-3}]$	methane concentration
j^*	$[ML^{-3}T^{-1}]$	volumetric mass source term
K_C	$[ML^{-3}]$	dissolved organic carbon half-saturation constant
M_t	$[T^{-1}]$	mass transfer coefficient
R	[-]	linear retardation factor
X	$[ML^{-3}]$	methanogenic bacteria concentration
Y_C	[-]	dissolved organic carbon yield coefficient
Y_I	[-]	carbon dioxide yield coefficient
Y_O	[-]	methane yield coefficient
Y_X	[-]	methanogenic bacteria yield coefficient
α_l	[L]	longitudinal dispersivity
α_t	[L]	transverse dispersivity
γ	$[ML^{-3}T^{-1}]$	zero-order mass production rate
κ	$[T^{-1}]$	general decay rate constant
κ_a	$[T^{-1}]$	accessible biodegradable solid carbon decay rate constant
κ_p	$[T^{-1}]$	protected biodegradable solid carbon decay rate constant
κ_d	$[T^{-1}]$	methanogenic bacteria decay rate constant
μ	$[T^{-1}]$	maximum methanogenesis rate
τ	[-]	tortuosity

Numerical Model (matrix notation)

$[H]$	$[L^2T^{-1}]$	conductance matrix
$\{J\}$	$[MT^{-1}]$	dissolved organic carbon input array
$[M]$	$[L^2T^{-1}]$	dissolved organic carbon consumption matrix
$\{P\}$	$[MT^{-1}]$	dissolved organic carbon production array
$\{Q_{in}\}$	$[L^3T^{-1}]$	fluid input array
$[R]$	$[L^2T^{-1}]$	advection-dispersion matrix
$[T]$	$[L^2]$	transport capacitance matrix
$[U]$	$[L^3]$	unsaturated fluid storage matrix
$[V]$	$[L^2]$	flow capacitance matrix

Numerical Model (general variables)

$()^i$	[-]	iteration level indicator
$()^j$	[-]	time level indicator
$\bar{()}$	[-]	elemental average
J_V	[L^3]	source carbon mass input
J_Γ	[L^3]	boundary carbon mass input
M_c	[L^3]	mass of carbon within model domain
Q_V	[L^3]	volumetric source fluid input
Q_Γ	[L^3]	volumetric boundary fluid input
V_w	[L^3]	volume of fluid within model domain
Δl	[L]	generalized grid spacing
Δt	[T]	time step size
Δt_{old}	[T]	time step size from previous step
ϵ_c	[L^3]	carbon mass balance error
ϵ_c^*	[-]	normalized carbon mass balance error
ϵ_w	[L^3]	fluid balance error
ϵ_w^*	[-]	normalized fluid balance error
ϵ_κ^*	[-]	normalized reaction rate error due to time discretization
Ψ_c	[L]	capillary pressure head constant
Ω	[-]	transport time-weighting factor
ω	[-]	flow time-weighting factor

Applications

t_{bt}	[T]	fluid breakthrough time
Z	[L]	waste column height
θ_{bulk}	[-]	bulk porosity
θ_{eff}	[-]	effective moisture content

Chapter 1

Introduction

Moisture flows through variably-saturated porous media in a multitude of near-surface environments. Water, gas, and solid particles interact in a wide variety of natural and human-influenced systems. Natural systems include soils, karst terrain, and regions with thick unsaturated zones, while human-influenced systems include landfill sites, mine tailings impoundments, land farms, and compost piles. Multispecies reactive transport in these environments may be important to predict weathering, mineral dissolution, and transport in various geological settings. An understanding of the key transport processes is also needed to predict contaminant dissolution, interaction with porous media, transformation, transport, and precipitation in natural or anthropogenic porous media. Landfill sites have been selected for detailed investigation in this thesis.

Decomposition of the biodegradable waste components in landfill sites is important for many reasons. Biodegradation generates gases, primarily carbon dioxide and methane, that may escape to the atmosphere to cause air pollution or accumulate in structures, such as residential basements, to cause health and explosion hazards. Furthermore, the methane generated at landfill sites during waste biodegradation is increasingly being used as an energy source in North America, Europe, and Asia. Additionally, water that percolates through the waste accumulates dissolved contaminants that are released during waste decay. This leachate may escape to aquifers or surface water near the landfill, polluting the water. Finally, waste decomposition

substantially reduces the waste volume, causing subsidence of the landfill site. Land reclamation and reuse is complicated by the differential settlement of landfills that may occur over many years after waste input has stopped.

An ongoing experimental research program at the University of Alberta has focused on the detailed study of water movement through municipal solid waste (MSW) as well as waste decomposition and settlement behavior. The scale of investigation is on the order of a few cubic metres. The main objectives of this thesis are to

- explore some of the processes that occur during waste decomposition;
- develop tools to aid in the analysis of the experimental results; and
- provide insight into the applicability of results at the present scale of investigation to larger scales, particularly the field or landfill scale.

Results from this thesis, and the larger research program, should lead to improved landfill site management and design techniques.

The processes thought to control moisture movement and decomposition in municipal solid waste are presented in Chapter 2. Since the physical structure of waste largely controls patterns of water movement, a conceptual model of the waste structure is discussed first. Next, mechanisms of gas and water movement are explained, followed by the main processes controlling anaerobic waste biodegradation and dissolved organic carbon (DOC) transport. In order to limit the scope of investigation, other kinds of decomposition, such as salt dissolution and aerobic biodegradation, are not considered in this thesis. A set of mathematical equations is derived from the conceptual models in the second part of Chapter 2.

A numerical simulator, called C-Flow, developed from the mathematical models derived in Chapter 2 is discussed in Chapter 3. The numerical formulation is described in the chapter, with additional details provided in Appendix A. A series of simulations is presented at the end of Chapter 3 in order to demonstrate that the model solves the set of mathematical equations accurately. The simulation results are compared to analytical solutions or independent numerical solutions.

Once the model has been shown to accurately solve the equations that it was designed to solve, it is used to simulate a set of moisture movement experiments (Chapter 4). The simulated results are compared to the experimental observations to assess whether or not the conceptual models are reasonable approximations to reality.

Two field-scale examples are presented in Chapter 5 to illustrate some of the capabilities and limitations of the numerical simulator. Although these examples are intended primarily as illustrative tools, it is possible to draw some broad conclusions regarding the influence that the scale of investigation exerts on moisture movement and waste decomposition. These conclusions should help guide future research efforts.

Chapter 2

Theory

This chapter describes the conceptual and mathematical models that form the basis of this thesis. First, the conceptual models of moisture flow, biodegradation, and dissolved organic carbon transport in municipal solid waste are discussed. The mathematical models developed from the conceptual models are presented at the end of the chapter.

2.1 Conceptual Models

A generalized cross-section of a typical landfill site and the surrounding environment is illustrated in Figure 2.1. The landfill has a large unsaturated zone where both gases and leachate (contaminated landfill water) are present and mobile. A significant saturated zone has also developed due to infiltration of water through the top of the landfill. Leachate is being pumped from below the water table for treatment or recirculation through the waste. Infiltrating water and recirculating leachate are commingling and percolating downward through the unsaturated zone. The figure also illustrates the possible scenario in which leachate escapes through the bottom of the landfill, causing a leachate plume to develop in the groundwater below and downgradient of the landfill site.

Figure 2.2 illustrates a section through a small volume of a landfill site containing typical municipal solid waste. Waste-filled garbage bags have been placed in a landfill;

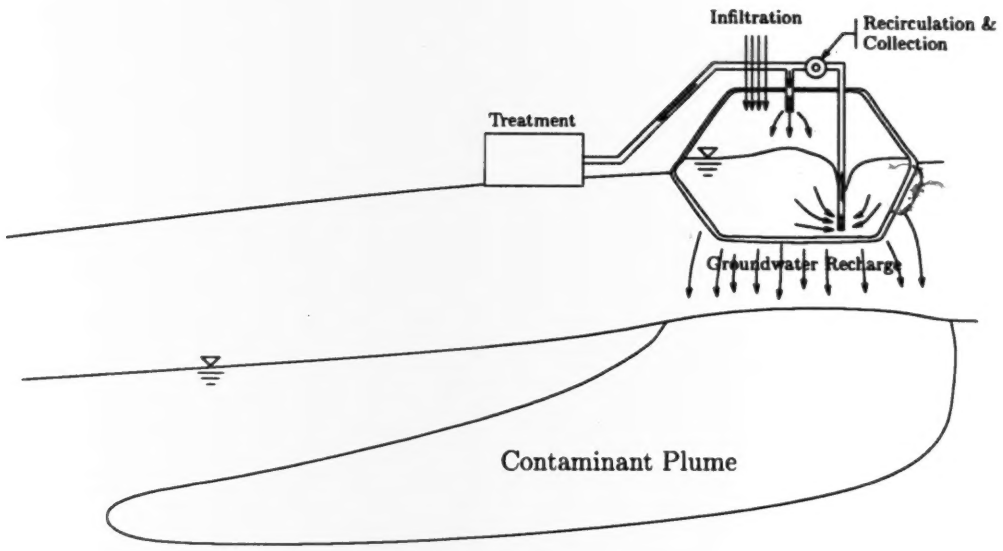

Figure 2.1: Conceptual model of overall landfill site behaviour

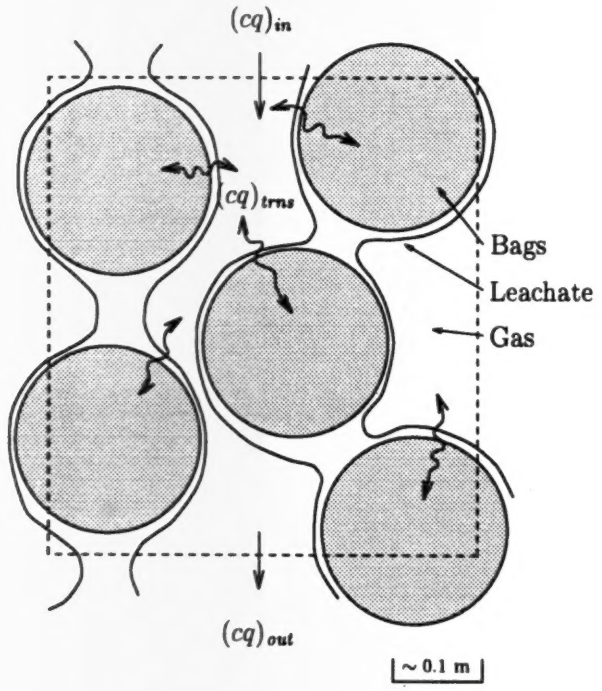

Figure 2.2: Conceptual model of small-scale municipal solid waste behaviour. The circles represent waste-filled garbage bags. The term (cq) represents fluid and mass transfer between bags and channels. See text for further discussion.

the waste has begun to biodegrade to various aqueous-phase and gaseous products. The primary solid waste biodegradation products may undergo further decay. Moving leachate acts both as a medium for biochemical reactions and as a transport agent, moving dissolved nutrients, biodegradation products and possibly bacteria from one region of the landfill to another.

The conceptual, mathematical, and numerical models developed in this thesis use a two-domain or dual-porosity approach. In the two-domain approach, the waste is separated into two interacting continua, one which conducts fluid rapidly but stores little, and one which stores large volumes of fluid but does not readily transport it. In municipal solid waste, inter-bag channels constitute the conductive domain. These form interconnected pathways that allow water to flow through the waste. The garbage bags themselves form the storative domain; water is stored in the pore spaces between waste particles within each garbage bag. The garbage bags are largely isolated from each other, limiting water movement from garbage bag to garbage bag. Biodegradation may occur in either the conductive or the storative domain, although most of the biodegradable solids are likely contained within garbage bags. In this thesis, the conductive domain is called the primary domain while the storative domain is called the secondary domain.

2.1.1 Gas Flow

The landfill atmosphere is composed mainly of nitrogen, carbon dioxide, and methane (Barlaz *et al.*, 1990). These low-viscosity gases flow readily through the unsaturated zone under very small pressure gradients (Celia and Binning, 1992). Therefore, gas pressure gradients are not expected to influence water flow within the landfill. The fate of gaseous-phase biodegradation products is not the focus of the present study, so details of gas transport are not important. Thus, the gas pressure is considered to be constant in the landfill and gas flow is neglected.

2.1.2 Water Flow

Waste placed in a landfill site is usually at an initial moisture content below the residual moisture content. Thus, water initially present in the waste is redistributed very slowly. Furthermore, a saturated zone can only form and leakage of leachate from the landfill site can only occur if the landfill is recharged by infiltration of water.

The structure of the waste complicates water movement. The landfill domain is considered to be primarily composed of waste-filled garbage bags, although the typical landfill also contains a variety of other materials, such as construction debris, yard waste, scrap metal, and others. For garbage bags, inter-bag voids are much larger and more permeable than the pores within the garbage bags; hence bulk water flow occurs mainly through the inter-bag voids. Water can move into or out of the garbage bags through tears in plastic bags or by direct seepage through paper or mesh bags. Little direct bag-to-bag flow is expected due to the small direct contact area and the high resistance to water movement across a garbage bag interface.

Water may flow through the large inter-bag voids as films, droplets, or through water-filled conduits. Flow occurs due to gravitational forces and hydraulic head gradients. The void spaces in the waste within a garbage bag are assumed to be so small that capillary forces dominate all other driving forces, including gravity, for water redistribution within a bag.

2.1.3 Biodegradation

Fresh municipal solid waste is composed of a wide variety of materials of highly variable biodegradability. Some materials, such as simple carbohydrates, are readily biodegradable in the landfill environment whereas others, such as glass and many plastics, are practically inert. According to Barlaz *et al.* (1990), cellulose and hemicellulose make up approximately 91% of the biodegradable fraction of typical municipal solid waste, with proteins contributing another 8%. Therefore, the elemental composition of the biodegradable material present at landfill sites is reasonably uni-

form. However, the molecular structure of the material, such as degree of branching, chain length, and degree of secondary chemical bonding, dramatically influences its biodegradation rate. Physical accessibility can also limit biodegradability. For example, balled-up sheets of paper are expected to degrade much more quickly than intact books or bundled newspapers because of differences in exposed surface areas.

Biodegradation proceeds through a series of complex biochemical reactions. The landfill environment is a dynamic ecosystem that contains diverse bacterial populations (Westlake *et al.*, 1995) that compete and cooperate in deriving energy from the decomposition of solid waste. It is exceedingly difficult, if not impossible, to quantify the full complexity of the ecosystem; certainly no such attempt is made in this thesis. Instead, a simplified conceptual model is presented to represent the gross ecosystem behaviour.

The biodegradation process within a landfill site is generally broken into a series of four steps (Barlaz *et al.*, 1990):

- Aerobic biodegradation;
- Hydrolysis and fermentation;
- Acetogenesis; and
- Methanogenesis.

Aerobic biodegradation is very fast; therefore, aerobic bacteria rapidly consume all the oxygen present within fresh waste. Oxygen may be replenished slowly at the margins of the landfill site by diffusion of atmospheric oxygen; however, most of the landfill environment is anaerobic (e.g., Lee *et al.*, 1994; Nozhevnikova *et al.*, 1993; Barlaz *et al.*, 1990; Farquhar, 1989). Thus, although aerobic biodegradation is fast, it is often unimportant at landfill sites due to the lack of oxygen.

Anaerobic biodegradation begins once the free oxygen has been consumed (Figure 2.3). Hydrolytic and fermentive bacteria convert biodegradable solids (cellulose, hemicellulose, and proteins) and any soluble organic carbon (e.g., sugars) to organic

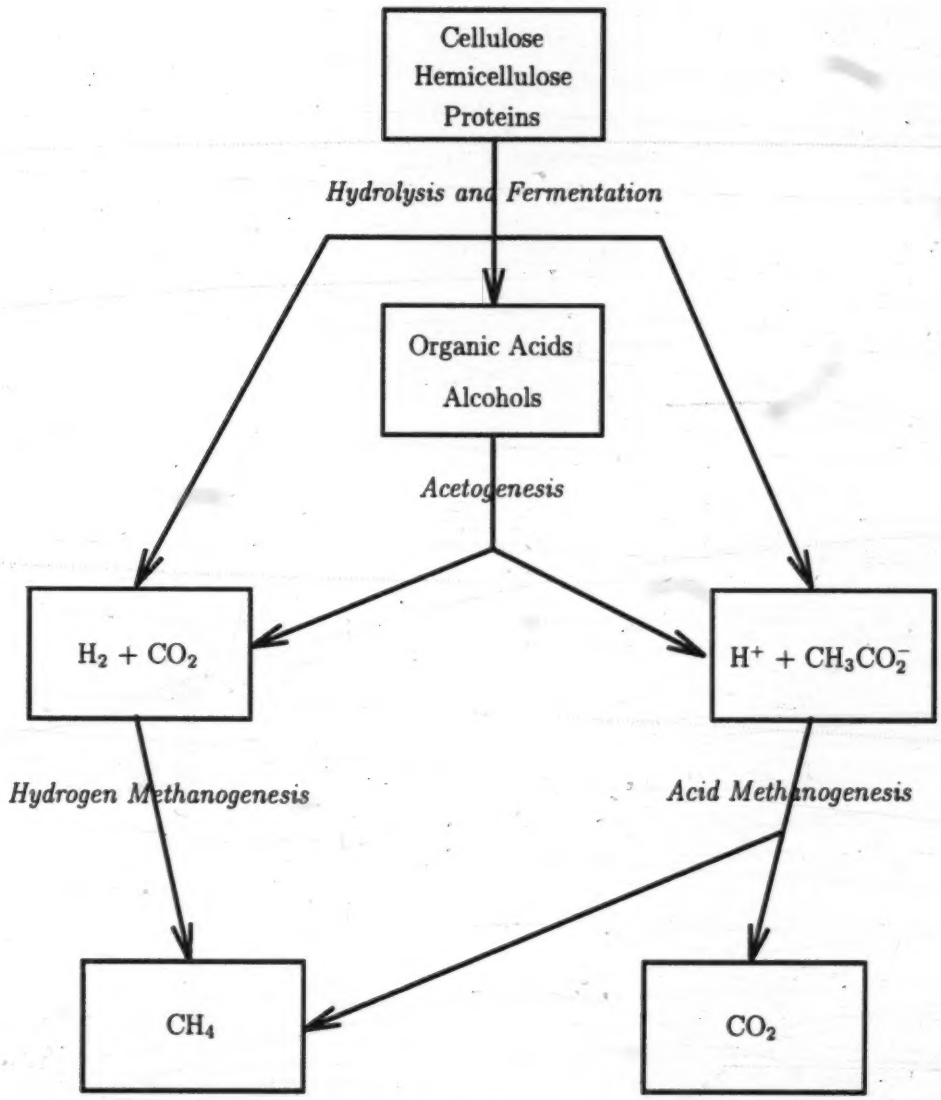

Figure 2.3: Conceptual model of anaerobic waste biodegradation. (modified from Barlaz *et al.*, 1990)

acids and alcohols, hydrogen, carbon dioxide, and methane. Acetogenic bacteria convert the aqueous-phase alcohols and acids to acetic acid, along with more hydrogen and carbon dioxide. The hydrogen (and some carbon dioxide) is rapidly converted to methane, although hydrogen concentrations may reach several percent of an atmosphere during the early stages of anaerobic waste decomposition (e.g., Lee *et al.*, 1993, Nozhevnikova *et al.*, 1993). The pH decreases due to acid production until the onset of methanogenesis. Acetic acid dissociates to hydrogen and acetate ions in the landfill leachate:

$$CH_3CO_2H \longleftrightarrow H^+ + CH_3CO_2^-. \tag{2.1}$$

Methanogenic bacteria consume acetic acid, converting it to methane and carbon dioxide, the terminal biodegradation products.

Bacterial populations increase dramatically during biodegradation; for example, Barlaz *et al.* (1989) observed a 6 order of magnitude increase in bacterial population over the duration of a laboratory-scale experiment. Population changes in the field may not be the same as in the laboratory, but substantial population increases are still expected as waste decomposes. These population increases result in some fraction of the organic carbon being stored in biomass.

2.1.4 Transport

The aqueous-phase intermediate products may by transported by advection and dispersion through the groundwater as they biodegrade. The alcohols and short-chain organic acids that make up the aqueous-phase have low vapour pressures (i.e., high boiling points) and high water solubilities, as summarized in Table 2.1. Thus, the dissolved organic carbon is not expected to be lost to the landfill atmosphere nor adsorbed to solid waste particles to any significant degree. Mass transfer between the primary and secondary domains occurs by advection with the moving leachate or by molecular diffusion.

Name	*Molec. Formula*	*Boiling Point* (°C)	*Aq. Solubility* (g/ℓ)
	Alcohols		
methyl alcohol	CH_3OH	64.5	∞
ethyl alcohol	CH_3CH_2OH	78.3	∞
propyl alcohol	$CH_3CH_2CH_2OH$	97.2	∞
isopropyl alcohol	$(CH_3)_2CHOH$	82.3	∞
butyl alcohol	$CH_3(CH_2)_3OH$	117	83
	Organic Acids		
formic acid	HCO_2H	100.5	∞
acetic acid	CH_3CO_2H	118	∞
propionic acid	$CH_3CH_2CO_2H$	141	∞
butyric acid	$CH_3(CH_2)_2CO_2H$	165.5	∞
valeric acid	$CH_3(CH_2)_3CO_2H$	187	37

Table 2.1: Selected physical properties of alcohols and organic acids (Fessenden and Fessenden, 1986)

2.2 Mathematical Models

The conceptual models of water flow and solid waste biodegradation described above were used to guide the development of a set of deterministic mathematical equations. The water flow equations are presented first, followed by the biodegradation and transport equations.

2.2.1 Moisture Flow

Darcy's Law

Darcy's Law is one of the fundamental equations of groundwater flow (Freeze and Cherry, 1979) and is used as the constitutive model for nearly all the equations of viscous flow through porous media. A one-dimensional form of Darcy's law is (Freeze and Cherry, 1979)

$$q_s = -K\frac{dh}{ds} \tag{2.2}$$

where q_s is the volumetric water flux in the direction of increasing s, h is the hydraulic head, and K is the hydraulic conductivity.

The hydraulic conductivity defined above is a function of the porous medium structure (grain-size distribution and packing), the physical properties of water (density and viscosity), and water saturation. It is often convenient to separate the contribution of each of these three factors as follows:

$$K = k_r(S_w)\frac{\rho_w g}{\mu_w}k \qquad (2.3)$$

where k_r is the relative permeability of the porous medium to water at the water saturation S_w, ρ_w is the density of water, μ_w is the viscosity of water, k is the intrinsic permeability of the porous medium, and g is the gravitational acceleration, which is essentially constant near the surface of the earth.

The hydraulic head is the sum of the elevation and pressure heads:

$$h = z + \psi \qquad (2.4)$$

where the elevation head, z, is the elevation of the point of measurement above a fixed (but arbitrary) datum. The pressure head, ψ, is defined as

$$\psi = \frac{P - P_0}{\rho_w g} \qquad (2.5)$$

where P is the absolute water pressure and P_0 is a constant (but arbitrary) reference pressure which is usually taken to be standard atmospheric pressure. Equation 2.5 is valid only for essentially incompressible fluids without significant density variation.

For landfill leachate, spatial density variations may be large enough to cause significant density-induced leachate transport. Accounting for density-induced advection introduces stronger nonlinearities to the mathematical formulation of flow and increased coupling between water flow and aqueous-phase transport. Since no experimental evidence of density-induced transport was encountered during the present study, the added effort required to account for density-induced transport was not considered to be warranted. The ability to account for density-induced transport could be added as a future mathematical model enhancement, if necessary.

The hydraulic head is the the total fluid energy potential only when certain conditions are met. First, the fluid velocities must be small enough that viscous forces dominate inertial forces. This requirement is satisfied when the Reynolds number based on the average grain diameter, d, is less than 10 (Freeze and Cherry, 1979). This Reynolds number is defined as

$$Re_d = \frac{\rho_w q d}{\mu_w} \tag{2.6}$$

where q is the magnitude of the water flux. Second, all gradients (e.g., electrical, thermal, or chemical) other than the hydraulic head gradient must be negligibly small (Freeze and Cherry, 1979). Since Darcy's Law is used for the following water flow derivation, these conditions must be satisfied for the flow equations to hold.

Primary Domain

The primary flow domain is treated as a continuum. Moisture flow is assumed to be governed by Darcy's Law and is thus limited to the conditions described above. The mass continuity equation is simplified by requiring that the fluid (water) and the porous medium are only slightly compressible, such that neither the fluid nor the porous medium deform much in response to fluid pressure changes. While it is acknowledged that municipal solid waste is typically rather compressible (Wall and Zeiss, 1995), it is necessary to assume that the waste is only slightly compressible to render the present problem tractable within the scope of this thesis.

Uniform fluid density is assumed for the derivation. Thus, the model cannot account for buoyancy-driven flow that may occur due to fluid density gradients caused by chemical concentration gradients or thermal gradients, for example. No significant buoyancy-driven flow is expected in situations where active pumping takes place because the hydraulic head gradients are so large. However, spatial density contrasts may be important in other situations; clearly, the mathematical model would need to be modified to accommodate such scenarios.

Some researchers have suggested that relative permeability is a tensor (e.g., Bear and Braester, 1987). However, limited information is available regarding the func-

tional relationships between the relative permeability tensor and the water saturation (Springer *et al.*, 1987), whereas a wealth of literature is available that relates a scalar relative permeability to water saturation for many different porous media (e.g., van Genuchten, 1980; Mualem, 1976; Brooks and Corey, 1964). Thus, without further data, it seems justified to treat the relative permeability as a scalar quantity. Relative permeability is probably not strongly anisotropic for porous media with isotropic intrinsic permeabilities, but may be in other cases (Brooks and Corey, 1964).

Based on the above conditions, the general partial differential equation describing the flow of water in a slightly-compressible, variably-saturated porous medium is (Bear, 1979)

$$-\frac{1}{r}\frac{\partial}{\partial x_i}\left(rk_r K_{ij}\frac{\partial h}{\partial x_j}\right) + S_w S_s \frac{\partial h}{\partial t} + \theta\frac{\partial S_w}{\partial t} = q^* \quad i,j = 1,2,3 \tag{2.7}$$

where K_{ij} is the saturated hydraulic conductivity tensor, S_s is the specific storage, θ is the porosity, and q^* is a volumetric fluid source term. Equation 2.7 applies to one, two, or three-dimensional flow. For one dimensional flow, $x_1 = x$; for two-dimensional flow, $x_1 = x$ (Cartesian coordinates) or $x_1 = r$ (axisymmetric coordinates) and $x_2 = z$. Three dimensional flow is not considered in this study. Note that the r's appearing in Equation 2.7 cancel for all but the radial coordinate direction. The specific storage is defined in the usual way (Freeze and Cherry, 1979):

$$S_s = \rho_w g\,(\alpha + \theta\beta)\,. \tag{2.8}$$

where α is, here only, the compressibility of the porous medium and β is the compressibility of water.

Secondary Domain

The secondary flow domain is treated as a one-dimensional, spherical continuum. The spherical coordinate system was selected to represent the garbage bags for its geometric simplicity. Thin, extensive slabs are also simple geometric shapes suitable for a one-dimensional mathematical approximation. Treating the bags as thin slabs,

rather than spheres, would result in a slightly different set of equations. Spheres are used in the present study because they are thought to approximate the shape of the garbage bags more closely than slabs.

Pressure head gradients are implicitly assumed to be much larger than elevation head gradients in the one-dimensional formulation, so only reasonably small, low-permeability spheres can be well-represented. An exception occurs in situations where the secondary domain is so permeable that the primary-secondary domain interface provides the only resistance to fluid transfer; the mathematical model represents such situations accurately.

The secondary-domain flow equation was derived by converting Equation 2.7 to spherical coordinates (Spiegel, 1968), dropping the elevation heads, and considering only the radial coordinate direction:

$$-\frac{1}{r^2}\frac{\partial}{\partial r}\left(r^2 k_r' K' \frac{\partial \psi'}{\partial r}\right) + S_w' S_s' \frac{\partial \psi'}{\partial t} + \theta' \frac{\partial S_w'}{\partial t} = 0 \tag{2.9}$$

where the variables are as described above and the primes denote the secondary domain. The centre of the sphere is a symmetry boundary:

$$\frac{\partial \psi'}{\partial r} = 0, \; r = 0. \tag{2.10}$$

The surface of the sphere is a first-order fluid transfer boundary:

$$q_0' = F_t(\psi - \psi')_0, \; r = r_0 \tag{2.11}$$

where q_0' is the volumetric flux of water into the secondary domain from the primary domain, r_0 is the outer sphere radius, F_t is the fluid transfer coefficient, and $(\psi - \psi')_0$ is the difference between the primary pressure head and the secondary pressure head at the primary–secondary domain interface.

The fluid-transfer coefficient represents the ease of water movement across the primary domain–secondary domain interface. The lower the resistance to fluid transfer across the interface, the larger the coefficient. A fluid-transfer coefficient of zero would represent a completely impervious interface, while an infinitely large coefficient would represent perfect hydraulic connection across the domain interface (i.e., negligible resistance to water transfer).

The source term for the secondary domain corresponds to a volumetric sink term in the primary domain. Therefore, the secondary domain makes a negative contribution to the primary domain source term:

$$q^* = -\frac{3}{r_0} q_0' V_s^* \tag{2.12}$$

where V_s^* is the fraction of the bulk porous medium occupied by the secondary domain. The factor $3/r_0$ in Equation 2.12 is the ratio of surface area to volume for a sphere.

Constitutive Unsaturated Relationships

Relative permeability and water saturation in Equations 2.7 and 2.9 are variable under unsaturated flow conditions. Constitutive relationships are thus required to relate relative permeability and water saturation to the state of the porous medium.

The water saturation is commonly taken to be a function of the equilibrium capillary pressure head, defined by

$$\psi_c = \frac{P_a - P_w}{\rho_w g} \tag{2.13}$$

where ψ_c is the equilibrium capillary pressure head and P_a is the air pressure. It must be stressed that the the capillary pressure head defined by Equation 2.13 is only the true capillary pressure head at thermodynamic equilibrium (Hassanizadeh and Gray, 1993); thus, it can only be taken as a state variable, as defined, for static or quasi-static conditions. Many practical situations, including variably-saturated flow through fine-textured materials, meet the quasi-static requirement. Water tends to flow slowly through saturated capillary tubes in such situations, with water retreating into smaller and smaller pores as capillary pressure increases (Jury *et al.*, 1991). However, in other situations, such as flow through coarse materials at low water saturations, water may flow as films that wet the porous medium solids rather than through saturated capillary tubes. In the case of film flow, the system may be far from pressure equilibrium so Equation 2.13 may not hold.

Brooks and Corey (1964) developed an empirical equation that relates water saturation to capillary pressure head based on the observation that effective water saturation–capillary pressure data often fall on a straight line on a log-log plot. Effective saturation is defined as the drainable saturation, varying from one at maximum water saturation to zero at the minimum drainable water saturation (see below). The constitutive equation is

$$S_e = \frac{S_w - S_r}{1 - S_r} = \begin{cases} \left(\frac{\psi_c}{\psi_d}\right)^{-\lambda}, & \psi_c > \psi_d \\ 1, & \psi_c \leq \psi_d \end{cases} \tag{2.14}$$

where S_e is the effective saturation, S_r is the residual saturation, ψ_d is the displacement capillary pressure head, and λ is the pore-size distribution index. Another commonly used equation is given by van Genuchten (1980):

$$S_e = \begin{cases} [1 + (\alpha\psi_c)^n]^{-m}, & \psi_c > 0 \\ 1, & \psi_c \leq 0 \end{cases} \tag{2.15}$$

where α, m, and n are shape parameters, and usually $m = 1 - 1/n$, although other values may be chosen (van Genuchten, 1980). The shape parameters α, m, and n are related to the shape parameters λ and ψ_d. For large values of the capillary pressure head, Equation 2.15 reduces to

$$S_e = (\alpha\psi_c)^{-mn}. \tag{2.16}$$

Thus, $\psi_d = 1/\alpha$ and, for $m = 1 - 1/n$, $\lambda = n - 1$ at large capillary pressure heads (van Genuchten, 1980).

Equations 2.14 and 2.15 may imply that water saturation is a single-valued function of capillary pressure for a given porous medium. It is not. The water saturation–capillary pressure relationship is hysteretic (Freeze and Cherry, 1979). The water saturation at a given capillary pressure is higher during drainage (removal of water from the porous medium) than during wetting (addition of water to the porous medium) (see Figure 2.4). Furthermore, the initial state of the porous medium dictates which curve is followed during drainage or wetting. Drainage of an initially saturated porous medium follows the initial drainage curve in Figure 2.4. Some residual

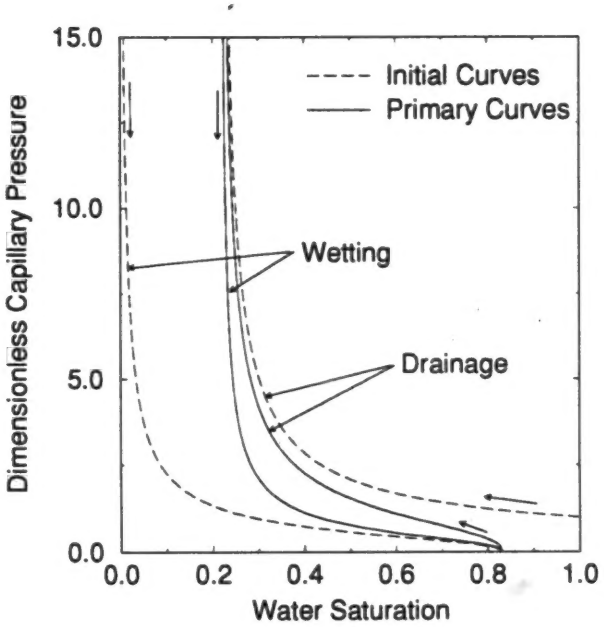

Figure 2.4: Schematic bounding curves for the capillary pressure–water saturation envelope. As indicated by the arrows, water saturation increases and capillary pressure decreases during wetting while water saturation decreases and capillary pressure increases during drainage.

water remains even at high capillary pressures. Subsequent wetting of the fully-drained medium follows the primary wetting curve, but some air becomes trapped as water saturation increases so the new maximum saturation is lower than the initial saturation. Subsequent wetting/drainage cycles remain within the envelope bounded by the primary wetting curve and the primary drainage curve (solid lines). Wetting of a dessicated porous medium follows the initial wetting curve. As for drainage, air becomes trapped as wetting proceeds. Subsequent drainage/wetting cycles again remain within the closed envelope. Water saturation can fall below the residual water saturation when water is lost by evaporation or to plant roots, for example (Jury *et al.*, 1991). Trapped air can dissipate by dissolution into water and subsequent transport in the aqueous phase.

Equation 2.14 can be adapted to account for hysteresis by treating the fitting parameters ψ_d and λ as functions of the wetting history. Similarly, the parameters α and n in Equation 2.15 can be varied. Initial wetting and initial drainage can be accommodated by modifying the definition of S_e:

$$S_e = \frac{S_w^* - S_r^*}{1 - S_r^*} \tag{2.17}$$

where S_r^* is 0 for a completely dessicated porous medium, increasing toward a maximum of S_r as wetting progresses. The modified water saturation is

$$S_w^* = S_w + S_{at} \tag{2.18}$$

where S_{at} is the trapped air saturation (Parker and Lenhard, 1987).

Lenhard *et al.* (1991) accounted for hysteretic flow behaviour by setting α to be twice as large for drainage as for imbibition and by defining an apparent water saturation to account for air entrapment during wetting. They applied their variably-saturated flow model to a laboratory experiment involving cyclic wetting and drainage of a porous medium. The model matched the observed water saturation history significantly better when hysteresis was accounted for in the constitutive relations (i.e., ψ_c–S_e and S_e–k_r) than when single-valued functions were used. Application of the hysteretic approach is limited by the availability of separate primary wetting

and drainage curves since only the drainage curve is usually measured. Furthermore, the variably-saturated flow problem is more mathematically and numerically complex when hysteretic constitutive equations are used instead of single-valued functions due to the extra parameters and increased overhead required to track the water saturation history.

Non-hysteretic constitutive relations are used in this thesis to reduce the complexity of the mathematical and numerical models. Simulations involving wetting/drainage cycles use average water saturation–capillary pressure curves to minimize the error introduced by neglecting hysteresis. Simulations involving strictly drainage or strictly wetting are not hysteretic; appropriate wetting or drainage curves are used for those simulations.

Wetting-fluid relative permeability is a weakly-hysteretic function of the water saturation (Lenhard and Parker, 1987). Single-valued water saturation–relative permeability curves are considered to adequately represent the porous medium behaviour. Relative permeability–effective saturation functions can be derived from the effective saturation–capillary pressure functions and knowledge of the flow-path tortuosity (Mualem, 1976). Equation 2.14 leads to (Brooks and Corey, 1964)

$$k_r = S_e^{(2+3\lambda)/\lambda} \tag{2.19}$$

and Equation 2.15 leads to (van Genuchten, 1980)

$$k_r = S_e^{1/2}\left[1-\left(1-S_e^{1/m}\right)^m\right]^2. \tag{2.20}$$

Boundary and Initial Conditions

Equation 2.7 describes a transient boundary value problem. Thus, boundary conditions must be specified for the entire domain boundary,

$$\Gamma = \Gamma_1 + \Gamma_2. \tag{2.21}$$

On Γ_1 (Type I, Dirichlet),

$$h = h_\Gamma \tag{2.22}$$

where h_Γ is the specified hydraulic head on Γ_1; on Γ_2 (Type II, Neuman),

$$\frac{\partial h}{\partial n} = f_\Gamma \tag{2.23}$$

where f_Γ is the specified gradient on Γ_2 and n designates the outward normal direction to the domain boundary. The initial condition must also be specified over the entire domain:

$$h = h_0 \tag{2.24}$$

where h_0 is the initial hydraulic head distribution. The initial pressure head must also be specified for the secondary domain:

$$\psi' = \psi'_0 \tag{2.25}$$

where ψ'_0 is the initial secondary-domain pressure head distribution. For simplicity, the initial pressure head is assumed to be uniform within each sphere in the secondary flow domain in the present study, but any initial pressure head distribution is theoretically permissible. Initial water saturations are calculated from capillary pressure heads using Equation 2.14 or 2.15 where the capillary pressure heads are calculated from the known pressure heads (calculated using hydraulic and elevation heads, if necessary).

A seepage face is a special type of boundary that can occur during variably-saturated flow (Cooley, 1983). Seepage faces form wherever the porous medium is exposed to the atmosphere and the pressure head inside the domain is greater than atmospheric pressure. In such a case the hydraulic head inside the domain is greater than that just outside the domain, causing water to flow out across the boundary. Since the region outside the domain is dry, no water is available to enter the domain across the boundary when the pressure head inside the domain falls below atmospheric pressure. In mathematical terms

$$h = z, \ \frac{\partial h}{\partial n} \leq 0 \tag{2.26}$$

$$\frac{\partial h}{\partial n} = 0, \ h \leq z. \tag{2.27}$$

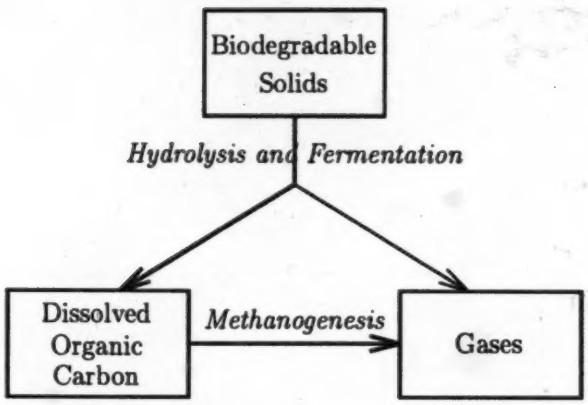

Figure 2.5: Simplified model of anaerobic waste biodegradation

Thus, portions of the seepage face below the water table ($\psi > 0$) are specified head boundaries while portions above ($\psi < 0$) are no flow boundaries.

The present formulation generalizes the seepage face boundary to a threshold hydraulic head boundary:

$$h = h_t, \ \frac{\partial h}{\partial n} \leq 0 \tag{2.28}$$

$$\frac{\partial h}{\partial n} = 0, \ h \leq h_t \tag{2.29}$$

where h_t is any fixed value of hydraulic head. The threshold head boundary is identical to the seepage face boundary when $h_t = z$.

2.2.2 Carbon Transformations

The chemical reactions involving carbon that occur during anaerobic waste biodegradation are described by a series of coupled partial differential equations based on the conceptual model presented in Section 2.1.3. The biodegradable carbon is transformed from the solid phase to an intermediate dissolved phase and, ultimately, to the gas phase (see Figure 2.5). Advective-dispersive mass transport may occur in the aqueous phase and gas phase; however, only aqueous-phase transport is considered here. The mathematical model describing the carbon transformations follows.

Hydrolysis and Fermentation

The mathematical model accounts for two classes of biodegradable solid organic carbon: accessible carbon and protected carbon. The accessible class includes carbon that is readily biodegradable by virtue of its chemical composition (e.g., short chains with minimal branching), molecular structure (e.g., weak secondary bonds), or physical accessibility (e.g., balled up paper). The protected class consists of the more recalcitrant materials (e.g., long, branched chains; intensive secondary bonding; bundled paper or intact books). The transformation rate of each component of the solid phase to the gaseous and aqueous phases is approximated by a first-order kinetic reaction:

$$\frac{\partial B_i}{\partial t} = -\theta_w \kappa_i B_i \tag{2.30}$$

where B_i is the bulk biodegradable carbon concentration (with dimensions of mass of carbon per unit volume of waste) and κ_i is the first-order hydrolysis/fermentation rate constant for phase i, with $i = a$ for the accessible carbon and $i = p$ for the protected carbon.

The volumetric moisture content, θ_w, is defined as

$$\theta_w = S_w\theta + S_s \int_0^{\psi} S_w d\psi. \tag{2.31}$$

The last term in Equation 2.31 represents moisture stored due to porous medium expansion and water compression as the pressure head increases. It is usually negligibly small because S_s is generally very small. The reaction rate is directly proportional to the moisture content in order to account for the observed increase in biodegradation rate with increasing moisture content (Gurijala and Suflita, 1993).

The first-order kinetic model was chosen over more complex models because of the difficulty in accurately quantifying the many factors that control hydrolysis and fermentation at a landfill site. As hydrolysis and fermentation proceed, the remaining biodegradable solids will be increasingly recalcitrant (Barlaz *et al.*, 1990), both chemically and physically. Thus, despite the fact that the hydrolytic and fermentative bacterial populations increase with time, biodegradation rates are expected to

decrease due to the decreasing biodegradability of the solids. Laboratory (Barlaz *et al.*, 1989) and field observations (Marticorena *et al.*, 1993) seem to indicate that solid organic carbon biodegradation does obey a first-order rate law. Therefore, the first-order, two-class model is considered to be a reasonable approximation.

Equation 2.30 is subject to the initial condition

$$B_i = B_{i,0} \tag{2.32}$$

where $B_{i,0}$ is the initial concentration distribution of biodegradable carbon in solid phase i.

Methanogenesis

Microbial populations can increase by several orders of magnitude due to the biodegradation of municipal solid waste (Barlaz *et al.*, 1989). Biodegradation rates generally increase with increasing microbial population. Factors other than the microbial population may limit biodegradation rates, as discussed above, but the size of the bacterial population is expected to be important during methanogenesis because the substrate (acetic acid) is in the aqueous phase. Thus, the availability of the substrate to the microbes should mainly be a function of its aqueous-phase concentration.

Monod kinetics account for changes in biodegradation rate due to changes in both substrate concentration and biomass concentration and so are commonly used when the two concentrations are expected to change significantly (e.g., Gilmour, 1996; Gönüllü, 1994; Lee *et al.*, 1993). Therefore, Monod kinetics are also used in the current study.

The biomass production equation is (Fetter, 1993)

$$\frac{\partial X}{\partial t} = Y_X \frac{\mu C}{K_C + C} X - \kappa_d X, \tag{2.33}$$

where X is the bulk biomass concentration (as carbon), C is the dissolved organic carbon concentration (as mass of carbon per unit volume of water), Y_X is the biomass yield coefficient, μ is the maximum methanogenesis rate, K_C is the half-saturation

constant, and κ_d is the first-order biomass decay rate. The biomass decay rate is usually insignificant relative to the growth rate (Gilmour, 1996), except when DOC concentrations are very small; therefore, the first-order approximation is considered to be adequate.

The initial biomass distribution must be specified:

$$X = X_0 \tag{2.34}$$

where X_0 is the initial biomass concentration.

Gas Production

Methane and carbon dioxide are the terminal carbon transformation products in anaerobic environments (Barlaz *et al.*, 1990). Hydrolysis/fermentation and methanogenesis both generate gases. Transport of methane and carbon dioxide would require the explicit consideration of gas flow and is beyond the scope of this study. Gas production is defined by

$$\frac{\partial G_i}{\partial t} = Y_i \theta_w (\kappa_a B_a + \kappa_p B_p) + \frac{1}{2}\left[(1 - Y_X)\frac{\mu C}{K_C + C} X + \kappa_d X\right] \tag{2.35}$$

where $i = I$ for the inorganic gas (CO_2) and $i = O$ for the organic gas (CH_4), G_i is the bulk concentration of gas i (as carbon), and Y_i is the fraction of the solid phase converted directly to gas i. The 1/2 in Equation 2.35 is derived from the stoichiometry of acid methanogenesis:

$$H^+ + CH_3CO_2^- \longrightarrow CH_4 + CO_2. \tag{2.36}$$

As discussed below, acetic acid is the only intermediate product considered in the present mathematical formulation. Since each mole of acetic acid (CH_3CO_2H) contains two moles of organic carbon (C), each mole of dissolved organic carbon contains 1/2 mole of acetic acid.

The initial gas concentrations must be specified:

$$G_i = G_{i,0} \tag{2.37}$$

where $G_{i,0}$ is the initial concentration distribution of gas i.

2.2.3 Aqueous-Phase Transport

The dissolved organic carbon generated as a byproduct of hydrolysis and fermentation exists primarily as short-chain acids and alcohols at typical landfill sites (Barlaz *et al.*, 1989). Lee *et al.* (1993) considered two classes of dissolved organic carbon: alcohols/organic acids and acetic acid. Acetic acid was produced both from direct solids biodegradation and from the conversion of alcohols and acids to acetic acid. Gönüllü (1994) considered a single dissolved species. Both studies treated transport as a simple one-dimensional advective process. Acetic acid alone is used in this thesis to represent the range of organic compounds present in the aqueous phase because it can be utilized directly by methanogenic bacteria. A more complete accounting of dissolved organic carbon would require a separate transport equation for each species considered, increasing both the computational burden and amount of information required to solve the landfill stabilization problem. Due to the poor characterization of most landfill sites and rapid acetogenesis relative to methanogenesis, the single aqueous-phase species model is thought to be adequate.

Primary Domain

The transport of acetic acid in the primary domain is described by the advection-dispersion equation, with a source term due to hydrolysis/fermentation of biodegradable carbon, a sink term due to methanogenesis of the dissolved organic carbon, and a source term due to mass transfer from the secondary domain. Since organic acids and alcohols have such high aqueous solubilities and low vapour pressures (see Table 2.1), adsorption onto the porous medium and volatilization to the vapour phase can be neglected. The resulting aqueous-phase transport equation is

$$-\frac{1}{r}\frac{\partial}{\partial x_i}\left(r\theta_w D_{ij}\frac{\partial C}{\partial x_j}\right) + \theta_w v_i \frac{\partial C}{\partial x_i} + \theta_w \frac{\partial C}{\partial t} =$$

$$\theta_w Y_C(\kappa_a B_a + \kappa_p B_p) - \frac{\mu X C}{K_C + C} + j^*, \quad i,j = 1,2,3 \qquad (2.38)$$

where v_i is the bulk average (macroscopic) linear velocity vector, Y_C is the fraction of solid organic carbon transformed to acetic acid, and j^* is a volumetric mass source

term, defined in the next section. The bulk velocity is obtained from the volumetric water flux, q_i, and the moisture content, θ_w:

$$v_i = \frac{q_i}{\theta_w}. \tag{2.39}$$

The dispersion tensor, D_{ij}, is defined as (Bear, 1979)

$$D_{ij} = \alpha_t v \delta_{ij} + (\alpha_l - \alpha_t)\frac{v_i v_j}{v} + \tau D_w \delta_{ij}, \quad i,j = 1,2,3 \tag{2.40}$$

where α_l and α_t are the longitudinal and transverse dispersivities, respectively, δ_{ij} is the Kronecker delta, τ is the water-phase tortuosity factor, and D_w is the aqueous-phase diffusion coefficient. The tortuosity is calculated using the equation developed by Millington and Quirk (1961):

$$\tau = \frac{{\theta_w}^{7/3}}{\theta^2}. \tag{2.41}$$

Secondary Domain

The same transformation used to convert Equation 2.7 to one-dimensional spherical coordinates can be applied to Equation 2.38. The transformation results in the following advection-dispersion equation, applicable for the secondary domain:

$$-\frac{1}{r^2}\frac{\partial}{\partial r}\left(r^2 \theta_w' D_{rr}' \frac{\partial C'}{\partial r}\right) + \theta_w' v_r' \frac{\partial C'}{\partial r} + \theta_w' \frac{\partial C'}{\partial t} =$$

$$\theta_w' Y_C' (\kappa_a' B_a' + \kappa_p' B_p') - \frac{\mu' X' C'}{K_C' + C'} \tag{2.42}$$

where the variables are described above and, as for the flow equation, the primes denote the secondary domain. The centre of the sphere is a symmetry boundary:

$$\frac{\partial C'}{\partial r} = 0, \; r = 0. \tag{2.43}$$

Advective mass transport across the sphere boundary is defined by

$$j_{0,adv}' = \begin{cases} q_0' C', & q_0' < 0 \\ 0, & q_0' = 0 \\ q_0' C, & q_0' > 0 \end{cases} \tag{2.44}$$

where $j'_{0,adv}$ is the advective mass flux into the secondary domain from the primary domain. Dispersive mass transport across the sphere boundary is via first-order mass transfer:

$$j'_{0,disp} = M_t(C - C')_0, \; r = r_0 \tag{2.45}$$

where $j'_{0,disp}$ is the dispersive mass flux into the secondary domain from the primary domain, M_t is the mass transfer coefficient, and $(C - C')_0$ is the difference between the primary concentration and the secondary concentration at the primary–secondary domain interface. The total mass flux into the sphere is given by

$$j'_0 = j'_{0,adv} + j'_{0,disp}. \tag{2.46}$$

As was the case for water transfer, the source term for the secondary domain corresponds to a volumetric sink term in the primary domain. Therefore, the secondary domain makes a negative contribution to the primary domain source term:

$$j^* = -\frac{3}{r_0} j'_0 V_s^*. \tag{2.47}$$

Initial and Boundary Conditions

Equation 2.38 describes a transient boundary-value problem. Thus, boundary conditions must be specified on the entire boundary,

$$\Gamma = \Gamma_1 + \Gamma_2 + \Gamma_3. \tag{2.48}$$

On Γ_1 (Type I, Dirichlet),

$$C = C_\Gamma \tag{2.49}$$

where C_Γ is the specified concentration on Γ_1; on Γ_2 (Type II, Neuman),

$$\frac{\partial C}{\partial n} = g_\Gamma \tag{2.50}$$

where g_Γ is the specified concentration gradient on Γ_2; and on Γ_3 (Type III, Cauchy),

$$q_n C - \theta_w D_n \frac{\partial C}{\partial n} = (qC)_\Gamma \tag{2.51}$$

where $(qC)_\Gamma$ is the specified total carbon mass flux on Γ_3. The initial concentration must also be specified over the entire domain:

$$C = C_0 \tag{2.52}$$

where C_0 is the initial dissolved organic carbon concentration distribution in the primary domain and

$$C' = C'_0 \tag{2.53}$$

where C'_0 is the initial dissolved organic carbon concentration in the secondary domain. For simplicity, the initial dissolved organic carbon concentration is assumed to be uniform in each sphere.

Chapter 3

Numerical Implementation

The mathematical model described in the previous chapter was implemented in a two-dimensional, two-domain numerical simulator called C-Flow. The following sections present the numerical model and a series of verification problems. Subsequent chapters discuss the application of C-Flow to the study of moisture flow, biodegradation, and dissolved organic carbon transport in municipal solid waste under a variety of conditions.

3.1 Domain Discretization

3.1.1 Primary Domain

The primary domain is a two-dimensional cross section. Gravity points in the negative z-direction. For Cartesian coordinates, the x-y-z coordinate system is used and all flow and transport occur in the x-z plane (Figure 3.1), with the domain thickness being arbitrary. For axisymmetric coordinates, the r-ϕ-z coordinate system is used and all flow and transport occur in the r-z plane (Figure 3.2). The domain is discretized using three-node triangular finite elements (Figure 3.3a) for both cases.

Two-node line elements (Figure 3.3b) can be used to represent explicit fractures or pumping wells. The line element represents a fracture of arbitrary width with one-dimensional flow and transport along the fracture in the x-z or r-z plane. In the axisymmetric coordinate system, vertical line elements can be placed near the z-axis

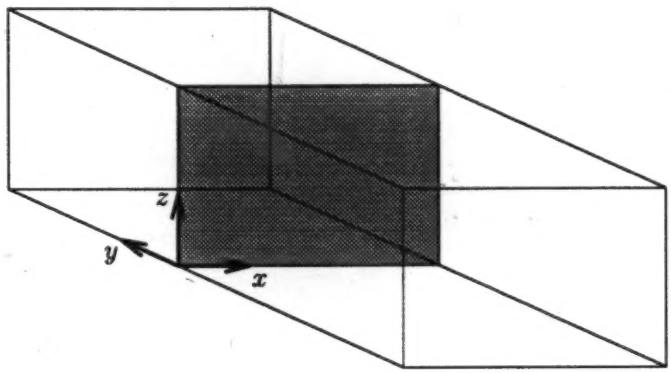

Figure 3.1: Cartesian coordinate system. The shaded region is the two-dimensional solution domain.

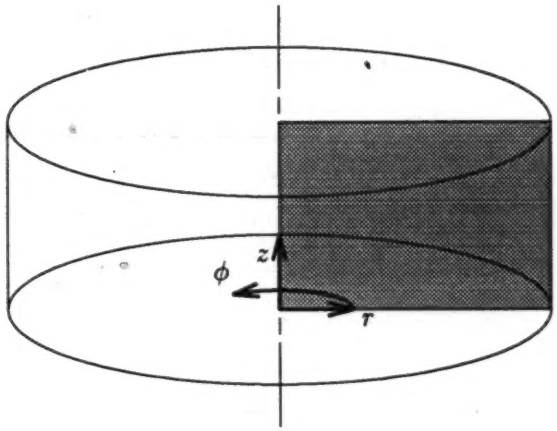

Figure 3.2: Cylindrical coordinate system. The shaded region is the two-dimensional axisymmetric solution domain.

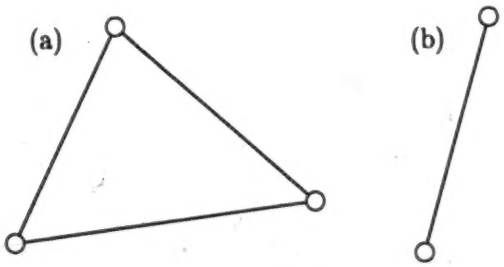

Figure 3.3: Finite elements used for domain discretization: (a) a three-node triangular element and (b) a two-node line element.

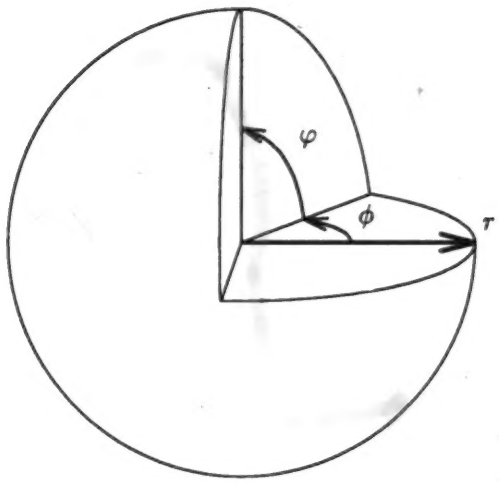

Figure 3.4: Spherical coordinate system. The thick line (r-axis) is the one-dimensional spherical solution domain.

to represent pumping wells. Although line elements are used exclusively to represent pumping wells in this thesis, they could be used to represent explicit fractures with no (or minimal) modification to C-Flow.

3.1.2 Secondary Domain

The secondary domain uses a spherical (r-ϕ-φ) coordinate system (Figure 3.4). Purely radial flow and transport are considered. One-dimensional spherical shell elements are used to discretize the domain. Each element is composed of two nodes, just as the line elements are (Figure 3.3b). The cross-sectional area of the shell element is a function of r; thus, the area varies along the element.

3.1.3 Interdomain Coupling

As outlined in Chapter 2, the two domains exchange fluid and mass through coupling terms (Equations 2.12 and 2.47). The coupling terms appear as volumetric source

terms for the primary domain and boundary conditions for the secondary domain. In the numerical implementation, each triangular finite element in the primary domain is associated with its own secondary domain, independent of all other elements. The elemental average pressure head and dissolved organic carbon concentration in the primary domain are imposed as boundary conditions on the secondary domain. No secondary domain is associated with a line element.

The resulting fluid and mass surface fluxes across the secondary-domain boundary are converted to primary-domain source terms (volumetric fluxes) via Equations 2.12 and 2.47, respectively. This conversion process automatically accounts for the relative sizes and volumes of the secondary and primary domains.

The two domains are independent of one another, other than the coupling at the interdomain boundary described above. The secondary domain does not see the primary domain directly, only through fluid input (or output) at the surface of a sphere. The flow equations are solved separately for the secondary domain associated with each primary-domain element using the boundary condition imposed by the primary domain pressure head.

The flow and transport equations are solved for the primary domain using the sources (or sinks) of fluid calculated for the secondary-domain in each primary-domain element. The sequence of secondary domain and primary domain calculations is repeated until the pressure heads and fluid fluxes stabilize.

Once the correct hydraulic heads have been calculated, the sequence is repeated for DOC transport and reactions. Further details of the flow and transport calculations are presented in the following sections.

3.1.4 Time

The flow, biodegradation, and transport equations are transient. Thus, discretization in time is required in addition to the previously discussed discretization in space. C-Flow is a time-marching program. The simulation begins with the initial condition and solves the equations at successive time levels until the end time is reached. Finite

differences are used to discretize the time derivatives at each time level (Huyakorn and Pinder, 1983). For example, the time derivative in Equation 2.7 is discretized by

$$\frac{\partial h}{\partial t} \approx \frac{h^{j+1} - h^{j}}{\Delta t} \tag{3.1}$$

where the superscript j denotes the previous time level, $j+1$ denotes the current time level, and Δt is the time-step size. Equation 3.1 holds for the entire interval between j and $j+1$.

The spatial derivatives may be evaluated at any time level, $j+\omega$, between j and $j+1$, where ω is a time-weighting factor that ranges from 0 to 1. As discussed by Huyakorn and Pinder (1983), evaluation of the spatial derivatives at j (i.e., $\omega = 0$) leads to the fully-explicit formulation, so named because the resulting set of matrix equations may be solved directly for the variables at the new time level. The explicit formulation is only conditionally stable, meaning that the error grows exponentially when a threshold Δt is reached. Evaluation of the spatial derivatives at a time level greater than or equal to $j + 1/2$ results in an unconditionally stable solution. Crank-Nicolson time weighting ($\omega = 1/2$) is formally the most accurate, but causes oscillations in the solution under some conditions. Fully-implicit time weighting ($\omega = 1$) leads to less accurate, but oscillation-free solutions.

3.2 Moisture Flow

The water flow equations (Equations 2.7 and 2.9) are discretized by a method similar to Celia *et al.* (1990). They achieved a practically perfect fluid balance by defining water saturations to be nodal quantities in their finite-element formulation, rather than using elemental fluid capacitances. The fluid balance definition will be discussed in Section 3.2.2; briefly, it is a measure of how well a numerical model accounts for fluid input to, output from, and storage within the solution domain. Some numerical formulations are not rigorous in their fluid accounting, while other fluid balance errors may arise from rounding during calculations. Celia *et al.* (1990) provide a detailed discussion of fluid balance errors as well as a summary of several numerical

formulations.

The final set of discretized equations describing water flow in the primary domain is

$$[H]\{h^{j+\omega}\} + \frac{1}{\Delta t}[V]\{h^{j+1} - h^{j}\} + \frac{1}{\Delta t}[U]\{S_w{}^{j+1} - S_w{}^{j}\} = \{Q_{in}\}. \qquad (3.2)$$

The global stiffness matrix $[H]$, capacitance matrix $[V]$, and unsaturated storage matrix $[U]$, are assembled from the elemental matrices, given in Appendix A. The vector $\{Q_{in}\}$ accounts for the contribution of water from the secondary domain.

The model allows either a uniform, constant time weighting factor or a variable time weighting factor based on the pressure heads from the previous time step. For variable time weighting, a separate flow time-weighting factor is defined for each node:

$$\omega = \begin{cases} 1 - \frac{1}{2}\frac{\Psi_c}{\Psi_c + \psi_c}, & \psi_c > 0 \\ 1, & \psi_c \leq 0 \end{cases} \qquad (3.3)$$

where Ψ_c is a positive constant. The function was chosen to balance the oscillation-free solutions obtained using fully-implicit time weighting against the reduction in iteration-to-iteration oscillations obtained by retaining part of the previous solution. Thus, the function uses fully-implicit time weighting ($\omega = 1$) under saturated or nearly-saturated conditions when the problem is linear, and evolves toward Crank-Nicolson time weighting ($\omega = 1/2$) at low water saturations when the problem becomes highly nonlinear. Setting Ψ_c to be on the order of ψ_d or $1/\alpha$ (or somewhat larger) yields a well-behaved solution for the problems tested. Experience with C-Flow indicates that variable time weighting may be more efficient and accurate than constant time weighting for some variably-saturated flow problems.

The matrix equations for the secondary domain are obtained by substituting the hydraulic heads in Equation 3.2 with pressure heads and dropping $\{Q_{in}\}$. The resulting set of secondary-domain matrix equations is

$$[H']\{\psi'^{j+\omega}\} + \frac{1}{\Delta t}[V']\{\psi'^{j+1} - \psi'^{j}\} + \frac{1}{\Delta t}[U']\{S_w'^{j+1} - S_w'^{j}\} = 0 \qquad (3.4)$$

where the primes denote the secondary domain. The elemental matrices for one-dimensional, spherical shell elements are derived in Appendix A.

3.2.1 Solution Procedure

The set of linearized equations is solved at each time level. Either Picard iteration or Newton-Raphson iteration is used within each time level to update $[H]$ and $[V]$ based on the solution from the previous iteration (Huyakorn and Pinder, 1983). The iteration scheme requires an initial estimate of the solution at each time step. This estimate is extrapolated from the previous solutions using the formulae first suggested by Cooley (1971) and also used by Huyakorn *et al.* (1984):

$$h^{0,j+1} = \begin{cases} h^0, & j = 0 \\ h^1 + \frac{1}{2}(h^1 - h^0)\Delta t/\Delta t_{old}, & j = 1 \\ h^j + (h^j - h^{j-1}) \log\left(\frac{t+\Delta t}{t}\right) / \log\left(\frac{t}{t-\Delta t_{old}}\right), & j > 1 \end{cases} \tag{3.5}$$

where Δt_{old} is the previous time step size and $h^0 = h_0$, the prescribed initial condition. This extrapolation reflects the solution behaviour expected for a transient problem as it approaches equilibrium.

The solution is iteratively updated, as described in Appendix A, until it has converged to within some acceptable error tolerance. If the maximum allowable number of iterations is exceeded before the solution converges then the time step size is decreased and the time step is repeated. The time step size is decreased for the next time step if the solution converges slowly. When the flow solution converges very quickly, the time step size is increased for the next time step as long as the transport solution also converges quickly. By default, Δt is halved and the time step is repeated if the solution has not converged within 25 iterations, Δt is halved for the next time step if the solution requires 12 - 25 iterations to converge, and Δt is increased by a factor of 1.1 for the next time step if the solution converges within 4 iterations. Different convergence parameters can be specified by the user if desired. Minimum and maximum time step sizes are also specified. The minimum step size is set to ensure that the the simulation runs to completion in a finite number of steps. The maximum step size may be used to control time-discretization errors for linear or mildly nonlinear problems.

3.2.2 Fluid Balance

Fluid-balance calculations are performed to ensure that the numerical model correctly accounts for water added to or removed from the flow domain. A poor fluid balance usually indicates that the numerical formulation is flawed, the code contains errors, or the solution convergence tolerance is too lax. An excellent fluid balance, however, does not guarantee solution accuracy. The fluid balance error for the primary domain is defined as follows:

$$\epsilon_w = Q_\Gamma + Q_V + V_{w,0} - V_w \tag{3.6}$$

where Q_Γ is the volume of water added to the domain across the domain boundary, Q_V is the volume from volumetric sources (i.e., the secondary domain), $V_{w,0}$ is the volume initially in the domain, and V_w is the volume currently in the domain. A perfect fluid balance yields an error of 0. The water balance may be normalized by dividing Equation 3.6 by $Q_\Gamma + Q_V$. The corresponding secondary-domain fluid balance is

$$\epsilon'_w = Q'_\Gamma + V'_{w,0} - V'_w. \tag{3.7}$$

The numerical formulation conserves water by its nature. Thus, fluid balance errors arise only from residual errors in the flow solution. For relatively simple variably-saturated flow simulations, normalized fluid balance errors are readily held to 10^{-10} or better. For more complex simulations, the convergence criteria commonly need to be relaxed to obtain a solution within an acceptable period of time because heterogeneities and sharp wetting fronts are difficult to resolve with the discrete nature of the grid. The resulting fluid balance errors for these complicated simulations may be as great as 10^{-2}. Experience with C-Flow indicates that the numerical results for highly nonlinear problems are usually insensitive to fluid balance errors up to a few percent.

3.3 Carbon Transformations

The organic carbon transformation reactions described in the previous chapter are discretized below. Numerical stability and computational efficiency are emphasized in order to compensate for nonlinearities introduced to the transport model by the Monod-kinetic term.

Fully-implicit time weighting is used for the hydrolysis/fermentation reactions to guarantee smooth solution behaviour. The biodegradable solid carbon concentrations are specified as piecewise constant over an element, so each element has an independent set of equations. The hydrolysis/fermentation equation (Equation 2.30) is discretized for each element using finite differences in time, resulting in

$$\bar{B}_i^{j+1} = \frac{\bar{B}_i^j}{1 + \Delta t \bar{\theta}_w \kappa_i} \tag{3.8}$$

where $i = a$ for the accessible carbon and $i = p$ for the protected carbon. Overbars are used both here and below to indicate that a variable is constant within an element.

The elemental biomass concentrations, like the biodegradable solids concentrations, are piecewise constant. Fully-implicit time weighting is used for the first-order decay term to ensure smooth solution behaviour. Fully-explicit time weighting is used for the production term, also to ensure that the solution is smooth. The explicit formulation has the further benefit of decoupling the biomass growth equation (Equation 2.33) from the transport equations (Equations 2.38 and 2.42). Known biomass concentrations are used in the discretized transport equations and the growth equations are solved only once at the end of each time step, using the converged, time-weighted, aqueous-phase concentrations. The discretized biomass growth equation is

$$\frac{\bar{X}^{j+1} - \bar{X}^j}{\Delta t} = \left(\frac{Y_X \mu \bar{C}^{j+\Omega}}{K_C + |\bar{C}^{j+\Omega}|} \right) \bar{X}^j - \kappa_d \bar{X}^{j+1} \tag{3.9}$$

where $\bar{C}^{j+\Omega}$ is the elementally-averaged aqueous-phase carbon concentration, evaluated at the time dictated by the transport time-weighting factor, Ω, discussed below. Equation 3.9 can be solved directly for the new elemental biomass concentration:

$$\bar{X}^{j+1} = \left[\Delta t \left(\frac{Y_X \mu \bar{C}^{j+\Omega}}{K_C + |\bar{C}^{j+\Omega}|} \right) + 1 \right] \frac{\bar{X}^j}{(1 + \kappa_d \Delta t)}. \tag{3.10}$$

Equation 3.10 is unconditionally stable as long as the aqueous-phase carbon concentration remains in the physical range, as it will for any stable transport time-weighting factor (i.e., $\Omega \geq 1/2$).

Carbon dioxide and methane are the terminal biodegradation products. The gas concentrations are piecewise constant in each element and are updated at the end of each time step. The elemental gas production equation, derived from Equation 2.35, is

$$\bar{G}_i^{j+1} = \bar{G}_i^j + Y_i \bar{\theta}_w (\kappa_a \bar{B}_a^{j+1} + \kappa_p \bar{B}_p^{j+1}) \Delta t + \frac{1}{2}\left[(1 - Y_X)\left(\frac{Y_X \mu \bar{C}^{j+\Omega}}{K_C + |\bar{C}^{j+\Omega}|}\right)\bar{X}^j + \kappa_d \bar{X}^{j+1}\right]\Delta t \qquad (3.11)$$

where $i = I$ for carbon dioxide and $i = O$ for methane.

3.4 Aqueous-Phase Carbon Transport

The advection-dispersion equations (Equations 2.38 and 2.42) are discretized by the Galerkin finite-element method used by Frind (1982) with additional source and sink terms to account for the biodegradation reactions. The resulting set of discretized equations that describe transport in the primary-domain is

$$[R]\{C^{j+\Omega}\} + \frac{1}{\Delta t}[T]\{C^{j+1} - C^j\} = \{P\} - [M]\{C^{j+\Omega}\} + \{J\} \qquad (3.12)$$

where $[R]$ is the advective-dispersive transport matrix, $[T]$ is the mass storage matrix, $\{P\}$ is the source term due to hydrolysis/fermentation, $[M]$ is the linearized sink term due to biological activity, and $\{J\}$ is the source term due to mass transfer from the secondary domain. The transport formulation uses a uniform time-weighting factor (Ω). In most simulations, either Crank-Nicolson time weighting ($\Omega = 1/2$) or fully-implicit time weighting ($\Omega = 1$) is used, although any time weighting factor in the range of 1/2 to 1 results in an unconditionally-stable transport solution. The global matrices are assembled from the elemental matrices defined in Appendix A.

Equation 3.12 can be rearranged to separate the known and unknown concentra-

tions. The resulting set of equations is

$$\left(\Omega[R] + \Omega[M] + \frac{1}{\Delta t}[T]\right)\{C^{j+1}\} =$$

$$\left(-(1-\Omega)[R] - (1-\Omega)[M] + \frac{1}{\Delta t}[T]\right)\{C^{j}\} + \{P\} + \{J\}. \tag{3.13}$$

The set of discretized secondary-domain equations is obtained by adding primes to the relevant primary-domain variables in Equation 3.13 and dropping $\{J\}$:

$$\left(\Omega[R'] + \Omega[M'] + \frac{1}{\Delta t}[T']\right)\{C'^{j+1}\} =$$

$$\left(-(1-\Omega)[R'] - (1-\Omega)[M'] + \frac{1}{\Delta t}[T']\right)\{C'^{j}\} + \{P'\}. \tag{3.14}$$

The secondary-domain elemental matrices are defined in Appendix A.

3.4.1 Solution Procedure

The transport-solution procedure is similar to the flow-solution procedure. The initial estimate for the transport solution is extrapolated in the same manner as for flow. The time step control is also identical. Typically, the transport solution converges in fewer iterations than the flow solution for problems involving transient, variably-saturated flow. When the transport solution alone is used to control time-step sizes, the step sizes are usually limited by accuracy and stability criteria (see Section 3.4.3) rather than solution tractability.

3.4.2 Mass Balance

The carbon-mass balance is calculated in a manner analogous to the water balance (Equation 3.6):

$$\epsilon_c = J_\Gamma + J_V + M_{c,0} - M_c \tag{3.15}$$

where J_Γ is the mass of carbon added to the domain across the domain boundary, J_V is the mass from volumetric sources (i.e., the secondary domain), $M_{c,0}$ is the mass initially in the domain, and M_c is the mass currently in the domain. The

carbon-mass balance may be normalized by dividing Equation 3.15 by $J_\Gamma + J_V$. The secondary-domain mass balance is

$$\epsilon_c' = J_\Gamma' + M_{c,0}' - M_c'. \tag{3.16}$$

Normalized mass balance errors are typically on the same order as fluid balance errors. For transport in a transient flow field, mass balance errors are influenced by fluid-balance errors because the aqueous-phase mass is the product of the concentration and the moisture content. Thus, fluid-balance errors can accentuate mass-balance errors. For transport in a steady-state flow field, mass balance errors are easily controlled because time step sizes required to obtain an accurate solution usually result in convergence within a few iterations even when tight convergence criteria are used.

3.4.3 Accuracy Criteria

The Peclet and Courant numbers are calculated during each transport simulation as guides to solution accuracy. For linear, one-dimensional advective-dispersive transport, the Peclet criterion is

$$Pe = \frac{v\Delta l}{D} \leq 2 \tag{3.17}$$

and the Courant criterion is

$$Cr = \frac{v\Delta t}{\Delta l} \leq \frac{Pe}{2} \tag{3.18}$$

where Δl is the grid spacing in the flow direction (Huyakorn and Pinder, 1983). These criteria are only approximate for multidimensional transport, but serve as useful guides to mesh design and time-step control. Huyakorn and Pinder (1983) suggest that accurate solutions may be obtained with Peclet numbers up to approximately 10. For any problem, the only sure way to guarantee that the solution is accurate is to repeat the simulation with successively finer grids and smaller time steps until the numerical results no longer vary with the discretization.

The error in the approximate biodegradable solids reaction equation (Equation 3.8) can be calculated by performing a Taylor-series expansion of the exact partial

differential equation (Equation 2.30). The temporal discretization error, written for the accessible carbon, is

$$\epsilon_\kappa = \frac{\kappa_a^2 \Delta t^2 B_a}{2}. \tag{3.19}$$

Equation 3.19 can be normalized by dividing by B_a:

$$\epsilon_\kappa^* = \frac{\kappa^2 \Delta t^2}{2} \tag{3.20}$$

where ϵ_κ^* is the normalized error and κ is a generalized first-order reaction coefficient, applicable to any of the reactions.

3.5 Verification Problems

A series of simulations were performed to compare output from C-Flow to available analytical solutions or other numerical simulators. In the numerical simulations, analytically infinite boundaries were placed far away from regions of interest so that they did not influence the numerical results. For all cases, results from C-Flow closely agreed with the analytical or independent numerical solutions. The verification problems are presented below.

3.5.1 Moisture Movement

The physical parameters used in the moisture movement verification problems are summarized in Table 3.1. Discretization information is summarized in Table 3.2. The fluid balance was excellent for all simulations.

Theis Solution

Theis (1935) derived an analytical solution to the single-domain flow equation (Equation 2.7) for radial flow to a pumping well in a uniform confined aquifer of infinite extent. The initial condition is

$$h(r, 0) = h_0 \text{ for all } r. \tag{3.21}$$

Param.	*Value*	*Units*	*Param.*	*Value*	*Units*
		Theis (1935)			
K_r	1.0×10^{-4}	(m/s)	S_s	1.0×10^{-5}	(m^{-1})
b	1.0	(m)	Q	1.0×10^{-4}	(m^3/s)
		Neuman (1974)			
K_r	1.0×10^{-3}	(m/s)	K_z	1.0×10^{-3}	(m/s)
S_s	1.0×10^{-5}	(m^{-1})	S_y	0.3	(–)
b	100.0	(m)	Q	1.0×10^{-2}	(m^3/s)
		Moench (1984)			
K_r	0.1	(m/s)	K'	0.1	(m/s)
S_s	1.0×10^{-5}	(m^{-1})	S'_s	1.0×10^{-3}	(m^{-1})
F_l	1.0×10^{-5}	(s^{-1})	r_0	10.0	(m)
b	1.0	(m)	r_w	0.1	(m)
Q	1.0	(m^3/s)			
		Therrien (1992)			
K_z	0.1	(m/day)	θ	0.45	(–)
S_s	0.0	(m^{-1})	S_r	0.333	(–)
		Cooley (1983)			
K_x	0.01	(–)	K_z	0.01	(–)
S_s	1.0×10^{-4}	(–)	θ	0.25	(–)
S_r	0.2	(–)			

Table 3.1: Parameters used for the moisture flow model verification problems

	x/r-direction		*z-direction*		time
simulation	*# nodes*	*spacing*	*# nodes*	*spacing*	*step size*
Theis (1935)	51	0.1 – 800 m[a]	2	1.0 m	$0.1 - 9 \times 10^4$ s
Neuman (1974)	38	$0.05 - 8 \times 10^3$ m[b]	20	0.5 – 15 m	$10^{-4} - 2 \times 10^5$ s
Moench (1984)	42	$0.01 - 2 \times 10^3$ m[b]	2	1.0 m	10^{-3} – 500 s
Therrien (1992)	2	0.5 m	41	0.05 m	10^{-3} – 0.4 days
Cooley (1983)	21	0.5	21	0.5	0.01 – 9

[a]with spacing increasing by a geometric factor of 1.2 away from the well
[b]with spacing increasing by a geometric factor of 1.4 away from the well

Table 3.2: Spatial and temporal discretization used for the moisture flow model verification problems

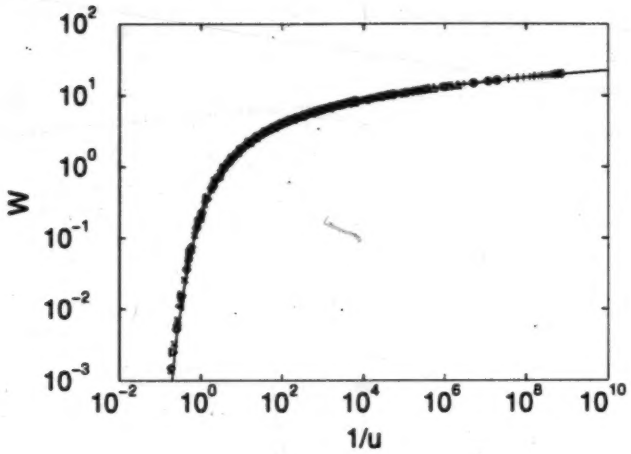

Figure 3.5: Comparison of C-Flow results to the Theis (1935) solution. The solid line is the analytical solution; symbols are numerical results at radii ranging from 1 to 1000 m. The analytical curve was obtained from tabular data in Freeze and Cherry (1979). Refer to the text for the problem description.

The boundary conditions are

$$h(\infty, t) = h_0 \text{ for all } t \tag{3.22}$$

and

$$\lim_{r \to 0} \left(r \frac{\partial h}{\partial r} \right) = \left(\frac{Q}{2\pi K_r b} \right) \text{ for } t > 0 \tag{3.23}$$

where b is the aquifer thickness and Q is the uniform pumping rate. Theis' solution to Equation 2.7, subject to the above boundary and initial conditions, is

$$h_0 - h(r, t) = \frac{Q}{4\pi K_r b} W(u) \tag{3.24}$$

where

$$u = \frac{r^2 S_s}{4 K_r t} \tag{3.25}$$

and $W(u)$ is the exponential integral, also known as the well function in hydrogeology. $W(u)$ is a dimensionless drawdown and $1/u$ is a dimensionless time. Figure 3.5 clearly demonstrates the accuracy of the numerical simulation.

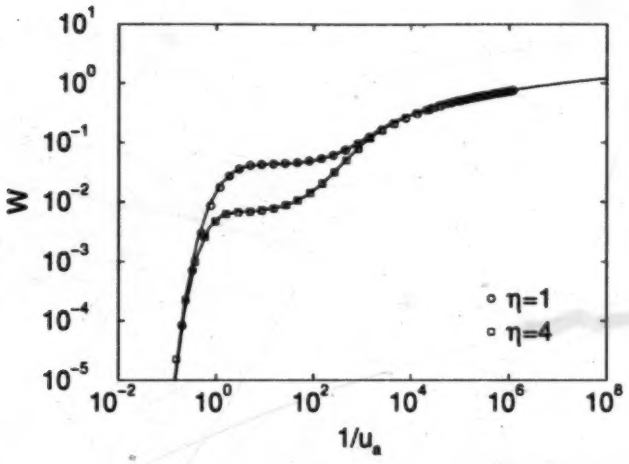

Figure 3.6: Comparison of C-Flow results to the Neuman (1974) solution. The solid lines are analytical results; symbols are numerical results; $u_b/u_a = 300$. Analytical results generated by AQTESOLV v1.15 (HydroSOLV, 1996). Refer to the text for the problem description.

Neuman Solution

Neuman (1974) derived an analytical solution describing the transient response of an unconfined aquifer to pumping from a well. His solution can be written in the same form as the Theis (1935) solution (Equation 3.24) where $(h_0 - h)$ is averaged through the aquifer thickness and $W(u)$ becomes $W(u_a, u_b, \eta)$ where $u_a = u$,

$$u_b = \frac{r^2 S_y}{4 K_r b t}, \tag{3.26}$$

and

$$\eta = \frac{r^2 K_z}{b^2 K_r}. \tag{3.27}$$

The specific yield of the aquifer, S_y, is defined as the volume of water released from storage in the aquifer per unit surface area of aquifer per unit decline in the water table (Freeze and Cherry, 1979). Figure 3.6 clearly demonstrates the accuracy of the numerical simulation.

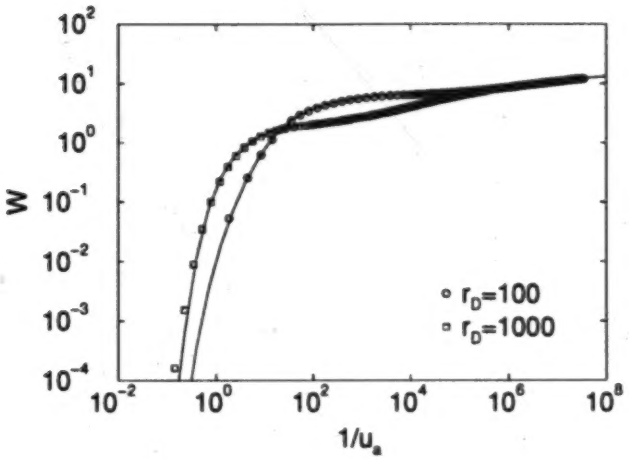

Figure 3.7: Comparison of C-Flow results to the Moench (1984) solution. The solid lines are analytical results; symbols are numerical results. Analytical results are generated by AQTESOLV v1.15 (HydroSOLV, 1996). Refer to the text for the problem description.

Moench Solution

Moench (1984) derived an analytical solution that describes radial flow to a well in a confined, fractured aquifer. His solution accounts for transient aquifer response in a two-domain system with either slab-shaped or spherical matrix blocks. The solution for spherical matrix blocks is used in the present comparison. Moench's solution also includes the effects of well-bore storage on observed drawdown. He used the well-bore radius to non-dimensionalize the radial-coordinate direction:

$$r_D = r/r_w \tag{3.28}$$

where r_D is the dimensionless radius and r_w is the well-bore radius. Resistance to fluid transfer due to fracture coatings is accounted for by considering a dimensionless fracture skin:

$$S_f = \frac{K'}{r_0 F_t}. \tag{3.29}$$

Figure 3.7 compares C-Flow to the analytical solution. The excellent agreement lends confidence to the numerical implementation of the two-domain model.

Advance of a Wetting Front

C-Flow was also used to simulate a vertical infiltration event in order to test its ability to model transient unsaturated moisture flow. The problem was taken from a verification example in Therrien (1992). The domain consisted of a 0.5 m by 0.5 m by 2.0 m high porous medium column. Water was added to the top of the column at a rate of 0.05 m/day for a period of ten days. The water table was fixed at the bottom of the column. The initial pressure head was -0.97 m, except at the upper surface where the initial pressure head was -0.90 m. The unsaturated constitutive relationships are defined by

$$S_e = \frac{\psi_c}{1.0\ \text{m}},\ \psi_c < 0 \tag{3.30}$$

and

$$k_r = S_e. \tag{3.31}$$

The agreement between the two models is excellent, as illustrated by Figure 3.8.

Two-Dimensional Transient Flow

The final variably-saturated flow verification problem involves two-dimensional, transient flow through a porous medium block. The problem is described in Cooley (1983). The domain consists of a 10.0 by 10.0 unit block of porous medium with all parameters being dimensionless. The top, bottom, and left domain boundaries are no-flow boundaries. The right boundary is a seepage face: zero pressure head is specified below the water table and no flow occurs above the water table. The block has an initial uniform hydraulic head of 10.0 units. The unsaturated constitutive relations are defined by

$$S_e = \frac{10}{10 + \psi_c^4},\ \psi_c < 0 \tag{3.32}$$

and

$$k_r = S_e. \tag{3.33}$$

The results obtained from C-Flow, showing the water table location at three times, are illustrated in Figure 3.9. They closely match results obtained by Cooley (1983),

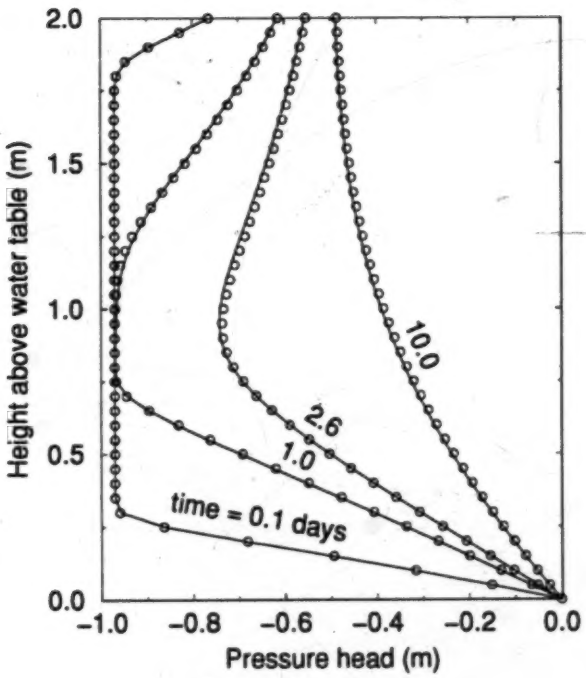

Figure 3.8: Comparison of C-Flow results to FRAC3DVS v1.3 (Therrien, 1992) for the vertical infiltration problem. The solid lines are FRAC3DVS results; symbols are C-Flow results. Refer to the text for the problem description.

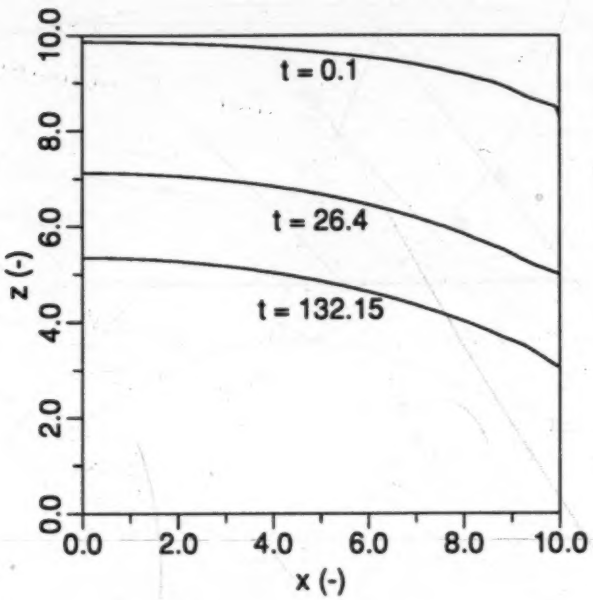

Figure 3.9: Position of the water-table in a draining block as predicted by C-Flow. Problem definition given by Cooley (1983) in his Example 3. Refer to the text for the problem description.

although his results are not reproduced here.

3.5.2 Reactive Transport

The physical parameters used in the transport verification problems are summarized in Table 3.3. Discretization information is summarized in Table 3.4. The mass balance was excellent for all simulations.

One-Dimensional Reactive Transport

Van Genuchten (1981) derived a series of analytical solutions to the one-dimensional advection-dispersion equation:

$$-D\frac{\partial^2 C}{\partial x^2} + v\frac{\partial C}{\partial x} + R\frac{\partial C}{\partial t} = \gamma - \kappa C \tag{3.34}$$

where R is the retardation factor, γ is a zero-order production term, and κ is a first-order decay term. The advection-dispersion equation presented in Chapter 2

Param.	*Value*	*Units*	*Param.*	*Value*	*Units*
		van Genuchten (1981)			
D	0.125	(m^2/day)	v	0.080	(m/day)
γ	0.080	(mg/ℓ·day)	κ	0.016	(day^{-1})
		Waterloo Hydrogeologic (1994)			
D_l	0.1	(m^2/day)	D_t	0.01	(m^2/day)
v	1.0	(m/day)	κ	0.02	(day^{-1})
		Bejan (1993)			
D	4.0	(m^2/day)	τ_0	0.01	(m)
M_t	0.4	(day^{-1})	θ	0.2	(–)

Table 3.3: Parameters used for the reactive transport model verification problems

	x/r-direction		*z-direction*		*time*
simulation	*# nodes*	*spacing* (m)	*# nodes*	*spacing* (m)	*step size* (days)
van Genuchten (1981)	101	5.0	2	1.0	0.1
Waterloo Hydro. (1994)	116	0.2 – 0.4	21	0.1 – 0.25	0.2
Bejan (1993)	21[a]	2×10^{-3} – 0.2[b]	N/A	N/A	10^{-3} – 0.5

[a]sphere discretization

[b]with spacing increasing by a geometric factor of 1.4 away from the surface of the sphere

Table 3.4: Spatial and temporal discretization used for the reactive transport model verification problems

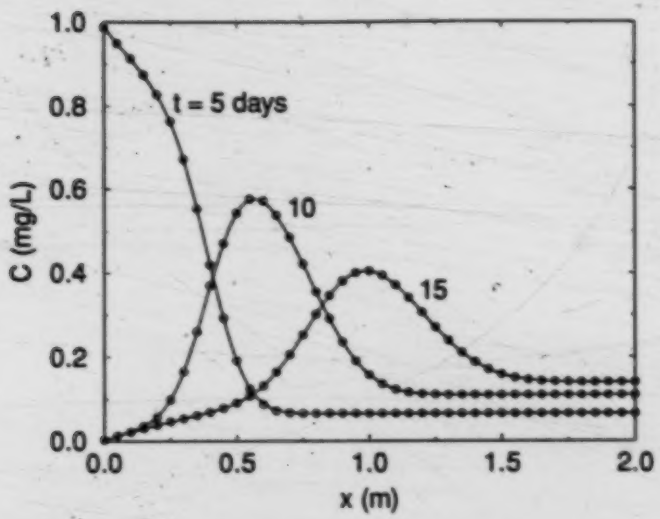

Figure 3.10: Comparison of C-Flow results to the van Genuchten (1981) solution. The solid lines are analytical results; symbols are numerical results. Analytical results are calculated. Refer to the text for the problem description.

(Equation 2.38) can be cast in the form of Equation 3.34 by dividing by θ_w and considering only unretarded transport ($R = 1$). The hydrolysis/fermentation term in Equation 2.38 can be used to account for zero-order mass production by setting $B_p = 0$, $\kappa_p = 0$, selecting a large initial value for B_a, and choosing a correspondingly small value for κ_a to obtain the desired zero-order production rate:

$$\gamma \approx Y_C \kappa_a B_a, \ \kappa_a \ll 1/t, \ \kappa_b = 0. \tag{3.35}$$

The Monod-kinetic decay term can be modified to represent first-order decay by holding X constant, choosing K_c to be much larger than the maximum aqueous-phase concentration, and selecting an appropriate value for μ:

$$\kappa \approx \frac{\mu}{\theta_w K_C}, \ K_C \gg C. \tag{3.36}$$

The domain is semi-infinite; the left boundary is Type III, with a boundary concentration of 1.0 mg/ℓ and the right boundary ($x \to \infty$) is zero-gradient. The initial concentration is zero everywhere in the domain. Figure 3.10 compares the C-Flow results to the analytical solution. The excellent agreement gives confidence to the coding of the reactive transport routines.

Two-Dimensional Reactive Transport

In order to test multidimensional transport, C-Flow results were compared to an an analytical solution describing reactive mass transport from a strip source (Waterloo Hydrogeologic, 1994). The solution accounts for one-dimensional flow, advective-dispersive transport, and first-order decay. The numerical domain is illustrated in Figure 3.11, which also shows the numerical results for the verification problem discussed below. Water flow is parallel to the x-axis. The left boundary is a fixed concentration boundary (Type I) with $C_0 = 0$ except for the strip source, indicated by the thick line on Figure 3.11, where $C_0 = 1$ mg/ℓ for $t = 0$ to 10 days. After ten days, the strip source is removed and the entire left-hand boundary reverts to zero concentration. The top and right-hand side boundaries are zero gradient; they behave as infinite boundaries over the duration of the simulation. The bottom boundary is a symmetry (zero gradient) boundary (the x-axis falls on the midpoint of the strip). The results of the numerical simulation are compared to the analytical solution in Figure 3.12. The excellent agreement shows that C-Flow correctly represents two-dimensional advective-dispersive transport.

Mass Transfer to a Sphere

The final verification problem was conducted to test the numerical implementation of mass transport in the secondary domain. The primary-domain concentration was fixed at 1.0 mg/ℓ. The concentration in the sphere was initially 0.0 and increased toward 1.0 mg/ℓ over time as mass was transferred to to the sphere from the primary domain. Mass transport was by diffusion alone. The analytical solution is the solution to the analogous heat-transfer problem (Bejan, 1993). Figure 3.13 illustrates the accuracy of the two-domain model implementation.

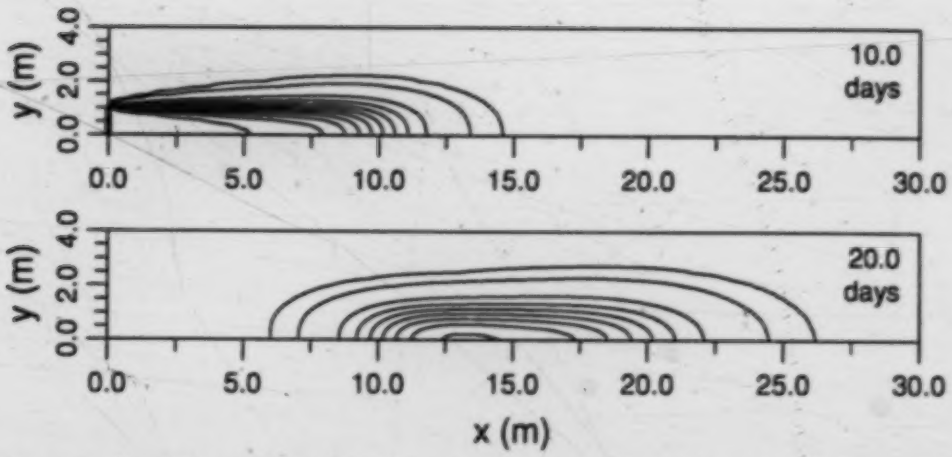

Figure 3.11: C-Flow results for the strip source problem (Waterloo Hydrogeologic, 1994) at two times. The lines are concentration contours; the concentrations are 0.001, 0.01, 0.1, 0.2, ..., 0.9 mg/ℓ, increasing from top to bottom in each plot. Refer to the text for the problem description.

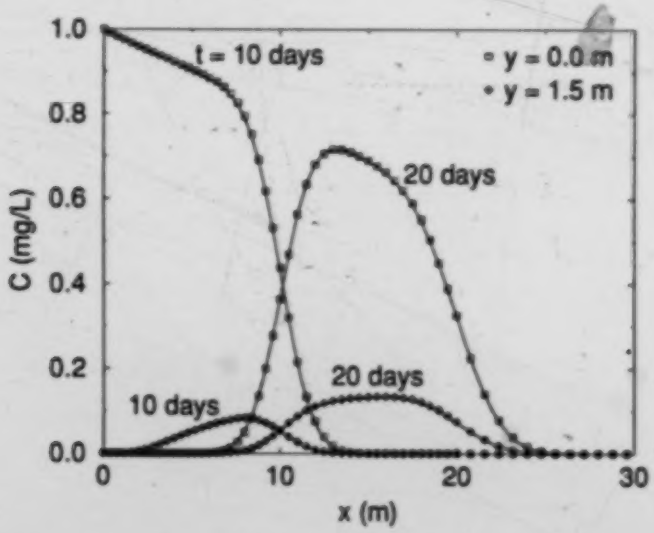

Figure 3.12: Comparison of C-Flow results to the strip source solution. The solid lines are analytical results; symbols are numerical results, with every second node omitted for clarity. Analytical results are generated by PRINCE v3.0 (Waterloo Hydrogeologic, 1994). Refer to the text for the problem description.

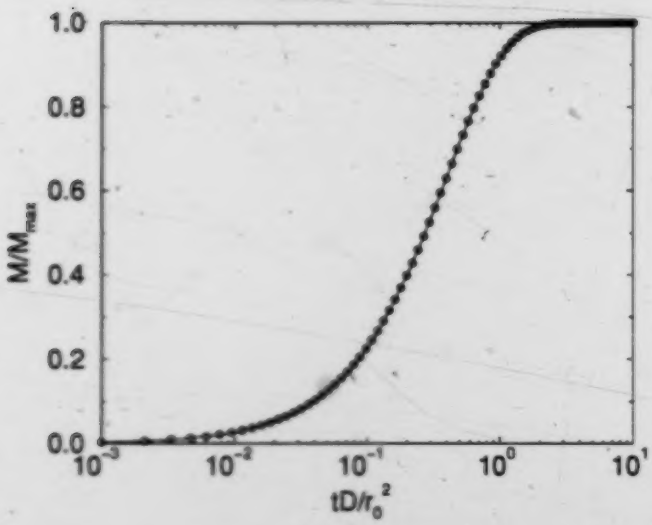

Figure 3.13: Comparison of C-Flow results to the analytical solution for transient mass transfer to a sphere. The solid line is the analytical solution; symbols are numerical results. Analytical results are calculated. Refer to the text for the problem description.

Chapter 4

Experimental Application

This chapter describes the application of C-Flow to a set of dumpster-scale experiments in which flow through municipal solid waste was investigated. The experimental observations helped guide the development of C-Flow. Subsequently, C-Flow was used to simulate the water-flow experiments. A brief overview of the experiment is presented below, followed by a discussion of the numerical simulations. Finally, an analysis of the model's sensitivity to changes in the various hydraulic parameters is presented.

4.1 Physical Scenario

Uguccioni (1995) performed a set of transient, unsaturated fluid flow experiments to investigate moisture movement characteristics in municipal solid waste. Fresh household waste was loaded into eight instrumented steel dumpsters that each measured approximately 1.6 m by 1.8 m by 1.5 m high. Waste was compacted with a hydraulic ram in four of the dumpsters to increase its bulk density. Each dumpster was then covered with a plastic sheet to prevent evaporation. The waste was then allowed to settle for ten days before the first application of water.

The instrumentation for each cell consisted of three tensiometer nests and a flow-cup grid. Each tensiometer nest included a shallow, intermediate, and deep measurement point. Rather than dedicate a tensiometer to each sampling point, Uguccioni

(1995) moved the tensiometers between measurements. He used PVC pipe to keep a path open that allowed easy insertion and removal of the tensiometers. Care was taken to ensure that the pipe did not create any preferential pathways for water flow. The flow-cup grid consisted of a three by three array of small water containers placed at the bottom of the waste layer. Water falling into each cup was collected in a 2 ℓ PET bottle. Refer to Uguccioni (1995) for further details of the experimental setup.

Water was applied to each test cell for thirty minutes each day, five days a week, for two to eight weeks, depending on the cell. The application rates varied both from cell to cell and over time for a given cell, ranging from about 3 to 25 mm/hr (corresponding to 4 – 36 ℓ/day). Since evaporation was minimized, essentially all water applied at the surface of the waste percolated downward, either being stored within the waste or draining freely from the bottom of each dumpster. The elapsed time from the first application of water to the first drainage from the bottom of the column was measured, as were the volumes of water that discharged each day. The cumulative volume of water discharged was summed from the discrete daily discharges; water storage was calculated by subtracting the volume of water discharged from the volume applied. The experimental results will be presented later, alongside the numerical predictions.

Uguccioni (1995) found extensive evidence of nonuniform infiltration of water through the waste columns from tensiometer and flow-cup data. Low-intensity water application resulted in more uniform infiltration than did high-intensity application. In addition, flow was more uniform for the compacted cells than the uncompacted ones. Statistical analysis showed that application intensity was a key parameter, influencing both breakthrough times and water storage. Waste compaction was shown to most influence cumulative water storage.

4.2 Preliminary Observations

The wetting front breakthrough data was analyzed to estimate the effective moisture content at first breakthrough. The bulk vertical water velocity was calculated for

each cell as follows:

$$v = \frac{Z}{t_{bt}} \tag{4.1}$$

where Z is the thickness of the waste layer at the time of first drainage and t_{bt} is the breakthrough time, defined as the time elapsed from the first application of water at the top of the waste layer to the time of first drainage from the bottom. For the cells with breakthrough times greater than one day (i.e., Cells 2, 3, and 4; see Table 4.1), only the time during which water application occurred was considered in t_{bt}.

The velocity is related to the infiltration rate through the effective moisture content:

$$v \approx \frac{q}{\theta_{eff}} \tag{4.2}$$

where the effective moisture content, θ_{eff}, is here defined as the volume of water participating in active flow, per unit bulk volume of waste. The velocity is plotted versus infiltration rate in Figure 4.1 using the data summarized in Table 4.1. The effective moisture contents for the experimental data range from 0.44% to 0.90%, with a best fit moisture content of 0.64% obtained by linear regression. The calculated moisture contents are not correlated to the infiltration rate or compaction, suggesting that the small bin-to-bin moisture content variation is caused primarily by random variations in the waste properties and differences in packing.

The calculated effective initial moisture contents were more than an order of magnitude smaller than the measured initial bulk moisture contents, which averaged about 12% (Table 4.1). Clearly, a small fraction of the waste volume conducted virtually all of the water. Over the duration of the experiments (weeks to months), moisture contents increased substantially in several of the experimental cells (Table 4.1). This large increase in moisture content required that water was being stored throughout the waste volume, not only in the primary water conduits.

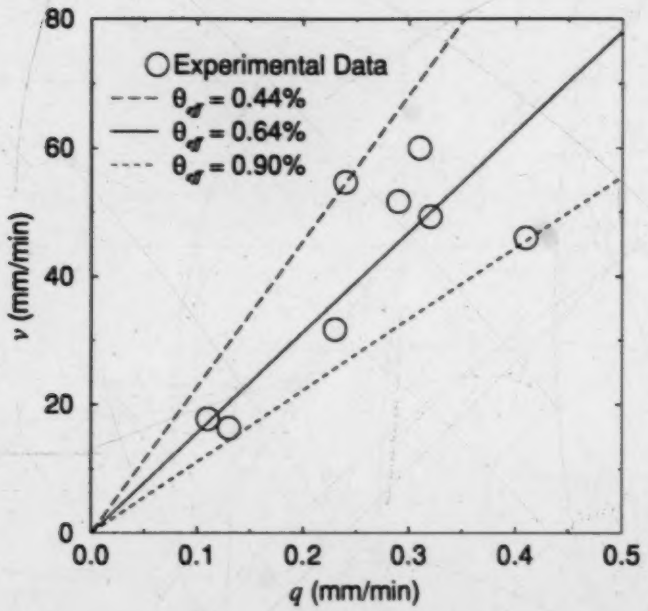

Figure 4.1: Relationship between water application rate, q, and bulk downward velocity, v, for the dumpster-scale water flow experiments. The curves are calculated using Equation 4.2 based on the indicated values of effective moisture content, θ_{eff}.

Cell	q (mm/min)	t_{bt} (min)	Z_i (m)	Z_0 (m)	Z_f (m)	θ_{w0} (%)	θ_{wf} (%)	$\Delta\theta_w$ (%)
1	0.24	15	1.05	0.82	0.68	8.8	12.6	3.8
2	0.13	60	1.05	0.98	0.95	12.2	21.1	8.9
3	0.11	45	1.10	0.80	0.64	12.5	22.5	10.0
4	0.23	30	1.05	0.92	0.90	12.7	20.7	8.0
5	0.29	15	1.05	0.78	0.65	11.2	13.4	2.2
6	0.41	20	1.00	0.92	0.78	11.7	19.0	7.3
7	0.32	15	1.00	0.74	0.62	10.3	10.3	0.0
8	0.31	15	1.00	0.90	0.86	13.0	16.5	3.5

Table 4.1: Selected data from the dumpster-scale water flow experiments used to constrain the numerical simulations. The subscripts on Z and θ_w indicate the initial values (i), the values on the first day of water application (0), and the final values (f). Modified from Uguccioni (1995).

4.3 Conceptual Model

The simplest model capable of representing the gross system behaviour was sought. Complex models produce a wide range of complex and tunable output; thus the model parameters risk losing much of their intended physical meaning. Uguccioni (1995) found that no single-domain, homogeneous porous medium flow model, including the HELP model (Schroeder, *et al.*, 1994) was capable of reproducing the experimentally observed behaviour. Two domains were necessary to reproduce both rapid initial breakthrough and high long-term storage capacity. Therefore, the waste was treated as a two-domain porous medium in the present study. Water storage was assumed to occur mainly in waste-filled garbage bags while bulk water movement was assumed to be through inter-bag channels. Thus, the channels were considered to make up the primary domain and the bags, the secondary domain. Water was assumed to move between the two domains through tears in the plastic garbage bags and by seepage through paper bags, as discussed previously.

The waste-filled garbage bags were modeled as isolated spheres with one-dimensional (spherical) moisture redistribution driven by pressure-head gradients. Bulk downward flow was assumed to occur through the network of inter-bag channels, which was treated as a variably-saturated porous medium. Since the test-cell walls limited the degree of lateral movement, horizontal flow could be neglected in the primary domain. Brooks–Corey parameters were used to relate capillary pressure to water saturation and water saturation to relative permeability in both domains; hysteresis was neglected. Uniform hydraulic properties were used for each domain. Water transfer between the two domains was via a first-order fluid-transfer coefficient.

4.4 Modeling Approach

Hydraulic porous medium properties, such as porosity, permeability, and capillary pressure–saturation relationships, are functions of the particle size distribution and packing in a porous medium (Freeze and Cherry, 1979). The particle size distributions

were similar for the waste placed in each of the eight experimental cells (Uguccioni, 1995). Packing may have depended on whether or not the waste was compacted initially. However, since the final dry bulk waste densities of all cells were similar and most waste compaction occurred early in the experiment (Uguccioni, 1995), the pore size distributions were likely also similar. The most important result of waste compaction was probably the tearing open of garbage bags, improving the hydraulic communication between the matrix and channels. Therefore, only the fluid-transfer coefficient was expected to vary significantly from bin to bin, being relatively small for uncompacted waste and relatively large for compacted waste. All other fluid flow parameters were held constant among the eight cells.

It is an approximation to treat all cells as being hydraulically identical. Such an approach has the benefit of keeping the number of tunable parameters small. Thus, confidence in the validity of the underlying mathematical model is increased if a single set of hydraulic parameters can be used to approximate the behaviour of all eight experiments. Conversely, no single set of parameters will exactly reproduce all of the experimental results since there is bound to be some bin-to-bin variability in the physical parameters, as well as experimental error. Furthermore, different combinations of hydraulic parameters produce similar output. Thus, it is unrealistic to seek the unique set of parameters that "best" describes the system. Instead, ranges of physically realistic parameters will be presented, along with a particular set of parameters that reasonably approximates the experimental data.

4.5 Initial and Boundary Conditions

The maximum capillary pressure head measured in any of the test cells was 0.8 m (Uguccioni, 1995). However, the tensiometers that were used to measure the capillary pressures were relocated between readings (*pers. comm.* Uguccioni, 1997) and may not have had time to reach equilibrium with the surrounding waste moisture. Cassell and Klute (1986) indicate that tensiometers may require several hours to equilibrate with their surroundings upon initial installation. Disequilibrium between the waste

moisture and tensiometers may have also explained some of the unexpected, and seemingly random, fluctuations in capillary-pressure readings that continued even after water addition had stopped (Uguccioni, 1995). The initial capillary pressure was chosen to be 4 m, which corresponded to the maximum capillary pressure observed in a similar experiment (Korfiatis, 1984).

No flow occurred across the top boundary, except during the discrete periods of water addition. Water addition was set to occur for 30 minutes per day at the same time of day for all days of water addition to match the experimental conditions. Free drainage was allowed to occur across the bottom boundary as long as the capillary pressure head was less than 0.33 m, corresponding to the capillary pressure head at field capacity for municipal solid waste (Zeiss and Major, 1993). No flow was permitted when the capillary pressure head was greater than 0.33 m. The lateral boundaries were no-flow boundaries, so that bulk water flow was constrained to be vertical.

4.6 Domain Discretization

C-Flow was used for the numerical simulations. The primary domain was discretized by a single column of 40 rectangles, each divided into two triangles, for a total of 80 triangular elements. A uniform vertical grid spacing was used for each simulation, with the spacing being adjusted to obtain the correct waste-column height for each experiment. Since one of the calibration variables was day-one water storage, each column height was set to Z_0 (Table 4.1). The width and thickness of each column were adjusted to obtain the correct cross-sectional area.

The secondary domain was composed of isolated spheres. Each sphere was discretized using 20 spherical-shell elements. The outermost shell element was the shortest. Element length increased exponentially by a factor of 1.4 toward the centre of the sphere, for the first twelve elements. Uniform spacing was used for the eight elements closest to the centre of each sphere. The resulting node spacing increased from 3.4×10^{-4} m to 1.9×10^{-2} m for the 0.2 m radius spheres. The size of the

spheres was in the middle of the range given in Table 4.2, discussed below.

Fully-implicit time weighting was used for all numerical simulations for maximum numerical stability. The time step sizes were automatically adjusted based on the number of nonlinear iterations required to converge on a solution at each time step. The time step size was decreased when more than 15 iterations were required for the solution to converge to within an absolute tolerance of 10^{-8} m error and increased when fewer than 4 iterations were required. Time step sizes varied from slightly less than 1 second to greater than 10 hours over the course of a typical simulation. The resulting cumulative mass balance errors were all less than 0.02 ℓ. To test the accuracy of the numerical simulations that used this convergence tolerance, the Cell 5 simulation was repeated with a convergence tolerance of 10^{-11} m; the predicted volumes of water stored changed by less than 0.4%, even though much smaller time steps were required. On the basis of the Cell 5 error analysis, it was assumed that errors arising from using the chosen convergence tolerance were negligible for all numerical simulations.

4.7 Results

4.7.1 Hydraulic Parameters

The results of the parameter estimation exercise are presented in Table 4.2 along with ranges for the physical parameters. The parameter ranges were estimated based on literature values where they existed and physical reasoning otherwise. One of the problems with the dual-porosity approach is that it is not commonly applied to municipal solid waste (Uguccioni and Zeiss, 1997). Thus, physical waste properties are reported in the literature as bulk averages, rather than in terms of separate matrix and channel properties.

Channel hydraulic conductivity is identical to bulk hydraulic conductivity when the channels provide the only significant bulk water flow pathway. The bulk hydraulic conductivity of municipal solid waste is in the range of 10^{-5} to 10^{-4} m/s (Oweis *et*

Channel Properties

Parameter	Units	Range	Best Estimate
K	(m/s)	$10^{-5} - 10^{-3}$	6.0×10^{-4}
θ	(%)	1 – 4	2.0
λ	(-)	0.5 – 2.0	1.0
ψ_d	(m)	0.01 – 0.15	0.07
S_r	(-)	0.0 – 0.5	0.25

Matrix Properties

Parameter	Units	Range	Best Estimate
K'	(m/s)	$10^{-8} - 10^{-6}$	1.2×10^{-7}
θ'	(%)	48 – 51	50.0
λ'	(-)	0.5 – 0.8	0.65
ψ'_d	(m)	0.06 – 0.21	0.12
S'_r	(-)	0.0 – 0.7	0.15
R_0	(m)	0.15 – 0.25	0.20
F_t (compacted)	(s^{-1})	$0 - \infty$	2×10^{-6}
F_t (uncompacted)	(s^{-1})	$0 - \infty$	1×10^{-7}

Table 4.2: Summary of parameters used for numerical simulation of the dumpster-scale unsaturated flow experiments. See text for further discussion.

al., 1990). The saturated hydraulic conductivity of the waste in the experimental cells may have been higher because the waste was undecomposed and less highly compacted than waste at typical landfill sites (Uguccioni, 1995). Furthermore, most municipal solid waste is landfilled along with thin layers of low-permeability geologic material, such as soil, silt, or fine sand (Oweis *et al.*, 1990), resulting in a reduced landfill-scale hydraulic conductivity relative to that of raw waste. Thus, the maximum channel hydraulic conductivity reported in Table 4.2 is higher than the value usually cited for landfilled waste.

The channel porosity was estimated from the effective moisture contents of Figure 4.1; a porosity of 1% corresponds to nearly saturated conditions while a porosity of 4% corresponds to a low water saturation in the channels, since

$$S_w = \frac{\theta_{eff}}{\theta}. \tag{4.3}$$

The selection of unsaturated constitutive-relation parameters (λ, ψ_d, and S_r) was

based on the assumptions that the channel widths were rather large (small ψ_d) and quite variable (small λ) (Brooks and Corey, 1964). A residual saturation of 0.0 represents primary wetting of initially dry waste and a value of 0.5 is an estimate of the maximum residual saturation from primary drainage of initially saturated waste.

Because no estimates of matrix hydraulic conductivity were found in the literature, the saturated matrix hydraulic conductivity was estimated to be in the range of silt–silty sand (Freeze and Cherry, 1979). The bulk waste porosity was experimentally measured to be 52% (Uguccioni, 1995). In the two-domain formulation, the bulk porosity is composed of both channel and matrix porosity; i.e.,

$$\theta_{bulk} = \theta + V_s^* \theta' . \tag{4.4}$$

The matrix porosity was only slightly smaller than the total porosity due to the low channel porosity. Ranges for matrix capillary pressure–water saturation curves were estimated from experimentally determined values for bulk waste (Zeiss and Major, 1993; Korfiatis *et al.*, 1984). The matrix parameters were expected to be similar to the bulk parameters because a much greater volume of water was stored in the matrix than in the channels. The residual saturation range was chosen to represent the range from primary wetting to primary drainage. The range of radii of the waste-filled spheres was chosen to be from approximately plastic shopping bag size (about 0.15 m) to green garbage bag size (about 0.25 m). Since no measurements or literature values were available for the channel–matrix fluid-transfer coefficient, it was used as a fitting parameter. The physical meaning of the fluid-transfer coefficient was discussed in Chapter 2.

4.7.2 Simulation Results

The cumulative volumes of water stored that were predicted by the numerical simulations (solid lines) for the eight cells are illustrated in Figures 4.2 to 4.5. The experimental results (dotted lines) and total volumes of water added (dashed lines) are included for comparison. The best estimate parameters were used for all simu-

Cell	Breakthrough Time				Day One				Cumulative			
	Model		Exp.		Model Stor. (ℓ)	Exp. Stor. (ℓ)	Vol. Appl. (ℓ)	Error (%)	Model Stor. (ℓ)	Exp. Stor. (ℓ)	Vol. Appl. (ℓ)	Error (%)
1	18	min	15	min	9	11	21	-10	129	90	331	+12
2	10	days	3	days	11	11	11	0	245	250	353	-1
3	1	days	2	days	6	8	8	-20	119	190	282	-25
4	2	days	1	days	19	19	19	0	204	210	304	-2
5	15	min	15	min	9	12	25	-12	73	50	303	+8
6	19	min	20	min	24	32	35	-23	154	190	422	-9
7	13	min	15	min	9	10	28	-4	69	0	332	+21
8	28	min	15	min	23	21	27	+7	157	90	320	+21

Table 4.3: Comparison of simulated and experimental results. Errors are normalized to volume of water applied.

lations (Table 4.2), with the larger F_t being used for the compacted cells (even cell numbers) and the smaller F_t being used for the uncompacted cells (odd cell numbers). A comparison of some of the key behaviour is presented in Table 4.3. The error is given as percent of water applied on day one (Day One column) or the total volume of water applied (Cumulative column).

4.8 Discussion

The model was able to simulate the behaviour of the experimental cells reasonably well. The maximum error in cumulative water storage was less than 25% of the volume of water applied for each of the eight experimental cells, and was substantially lower for Cells 1, 2, 4, and 5 (see Table 4.3 and Figures 4.2 to 4.5). In addition to representing the substantial increase in storage observed in many of the cells, the numerical model also reproduced the rapid initial breakthrough, approximating both breakthrough times and volumes (Table 4.3). The model predicted a much later breakthrough time than observed for Cell 2, but the total experimental discharge up to day 10 was less than 2% of the input. Although it would have been possible to improve the match for each one of the experimental curves by using a separate set of parameters for each cell, such tuning was considered to be unwarranted given the

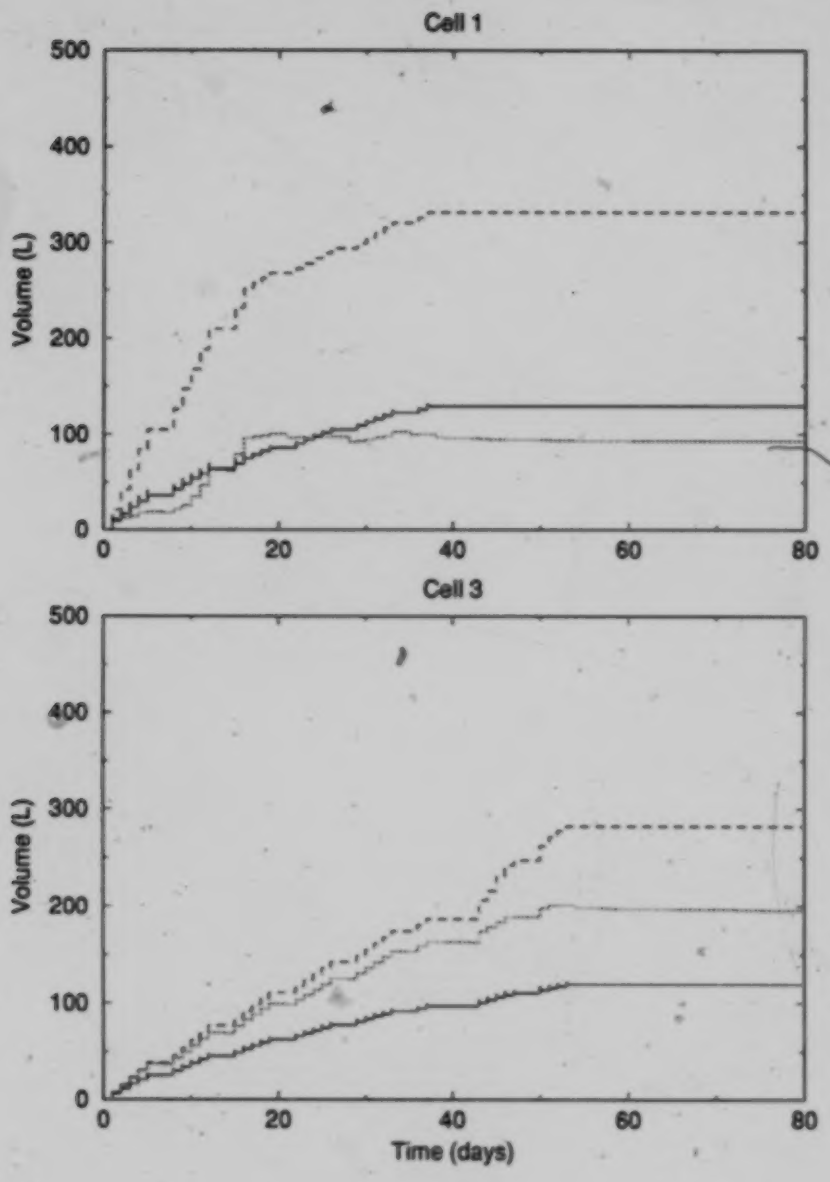

Figure 4.2: Comparison of numerical and experimental results for the uncompacted, low infiltration rate cells. Solid lines are predicted cumulative volumes of water stored, dotted lines are measured. Dashed lines are cumulative volumes of water applied to the cells.

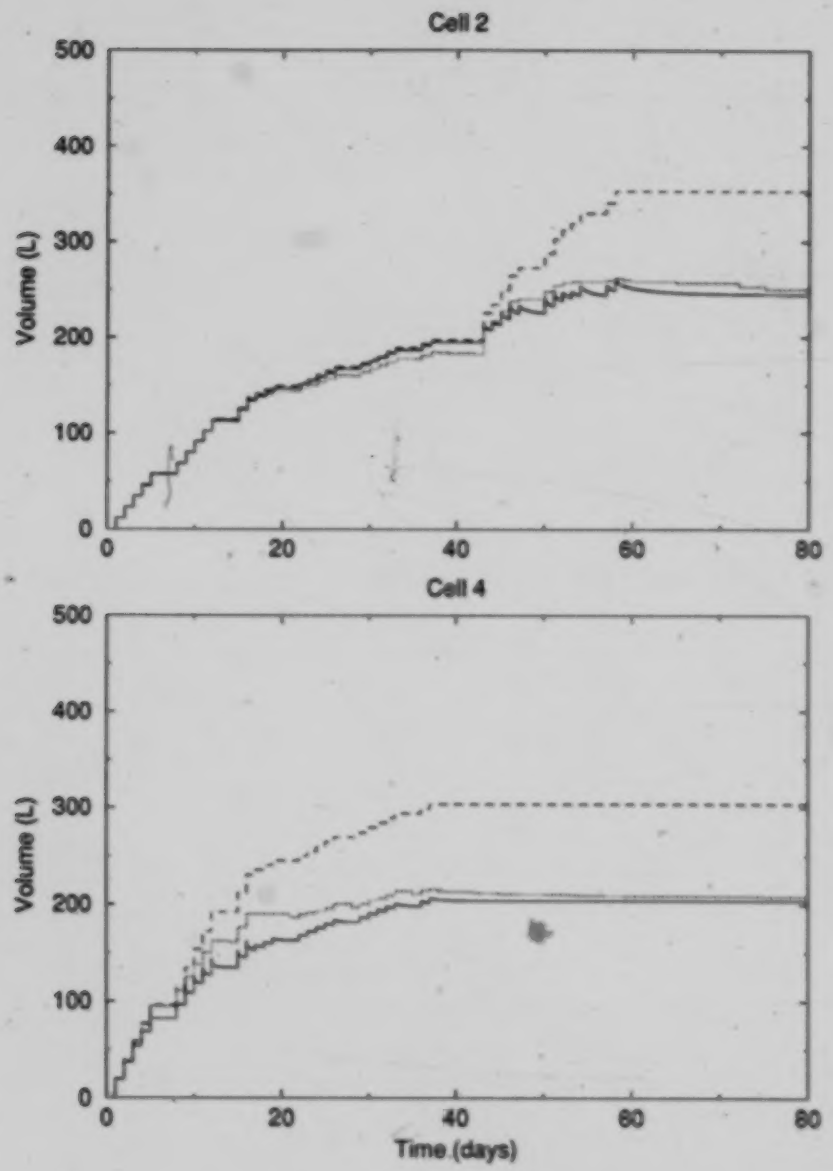

Figure 4.3: Comparison of numerical and experimental results for the compacted, low infiltration rate cells. Solid lines are predicted cumulative volumes of water stored, dotted lines are measured. Dashed lines are cumulative volumes of water applied to the cells.

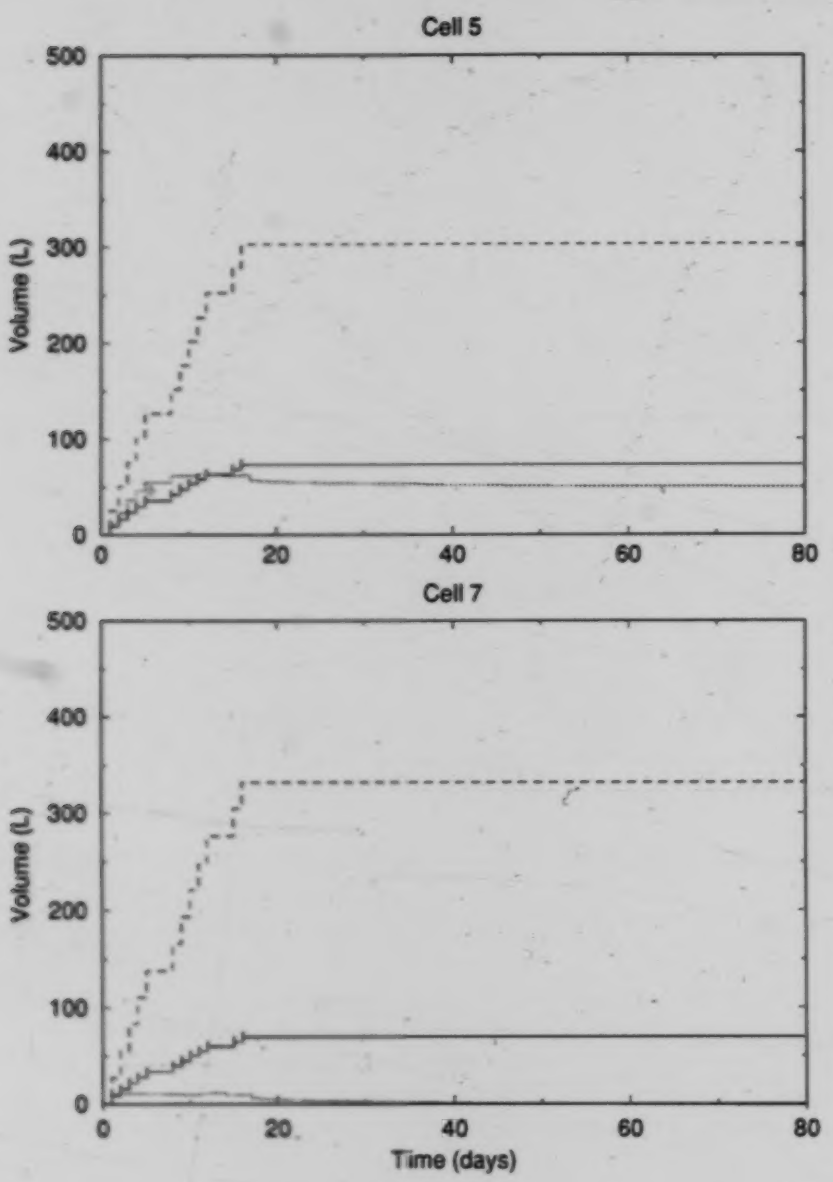

Figure 4.4: Comparison of numerical and experimental results for the uncompacted, high infiltration rate cells. Solid lines are predicted cumulative volumes of water stored, dotted lines are measured. Dashed lines are cumulative volumes of water applied to the cells.

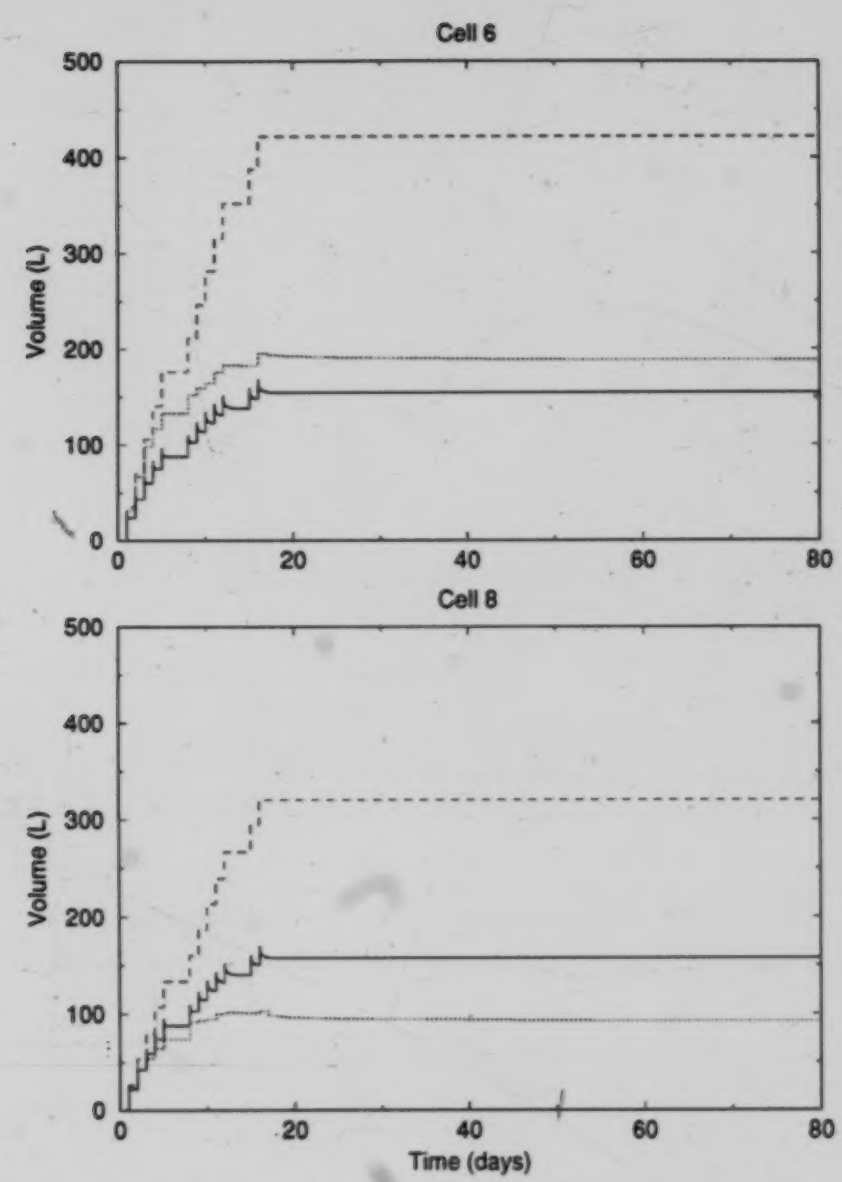

Figure 4.5: Comparison of numerical and experimental results for the compacted, high infiltration rate cells. Solid lines are predicted cumulative volumes of water stored, dotted lines are measured. Dashed lines are cumulative volumes of water applied to the cells.

limited number of experimentally measured hydraulic parameters.

4.8.1 Fluid Transfer

The model tended to overpredict water transfer from the channels to the matrix at low infiltration rates and underpredict transfer at high rates. No combination of model parameters could overcome this limitation. It was speculated that the fluid-transfer coefficient implemented in the model failed to fully capture the physical mechanism of water transfer from the channels to the matrix.

Water flowing through household waste is likely transferred from inter-bag channels to the waste within the bags primarily through tears in the plastic garbage bags. Highly torn bags present virtually no resistance to water transfer; the numerical model represents such behaviour accurately. However, water transfer to bags containing a few discrete tears may be highly sensitive to the water application rate since most of the surface of those bags is impermeable to water. Thus, water may preferentially flow along paths that intersect only a few tears at low application rates, whereas higher application rates cause water to flow over a larger bag surface area, intersecting more tears. The numerical model treats the torn garbage bags as a uniform resistance to water transfer. The driving force for water transfer increases slightly with flow rate as the hydraulic head in the channels increases but no new pathways for water transfer appear. The accurate representation of hydraulic channel–matrix coupling in municipal solid waste is a rich and interesting topic for future research.

4.8.2 Waste Compaction

The experimental results from the uncompacted cells were more variable than from the compacted ones. Low compaction, low infiltration rate cells, Cells 1 and 3, (Figure 4.2) stored nearly the same volume of water over the first 20 days of infiltration, despite significantly different total application rates. Nearly all of the water added to Cell 1 after day 20 was discharged, indicating that the available storage had been used. Conversely, a substantial fraction of the water applied to Cell 3 continued to be

stored until the end of the experiment, indicating a continuing availability of storage. In contrast, the high compaction, low infiltration rate cells, Cells 2 and 4 (Figure 4.3) showed much less variability.

A similar trend was observed for the high infiltration rate cells. The low compaction cells, Cells 5 and 7, (Figure 4.4) showed much inter-bin variability, with Cell 5 storing more water than Cell 7, even though Cell 7 had the higher application rate. In fact, Cell 7 had a net water loss over the duration of the experiment. In contrast, the high compaction cells, Cells 6 and 8, (Figure 4.5) showed the expected increase in storage with increasing infiltration rate.

Several factors may have contributed to the apparent increase in bin-to-bin variability for the uncompacted cells, relative to the compacted ones. The differences in final heights of the uncompacted and compacted cells likely played a role in controlling variability. All the waste column heights were initially about the same (1.00 – 1.10 m: Table 4.1) but the waste settled much more in the uncompacted cells than in the compacted cells. The final uncompacted waste column heights were 0.62 – 0.68 m compared to 0.78 – 0.95 m for the compacted cells (Table 4.1). The longer water flow path length in the compacted cells likely contributed to the reduced variability. Variability in the degree of bag tearing may have been another factor. Compaction may have resulted in garbage bags that were torn more uniformly than the uncompacted bags, resulting in a more uniform coupling between the matrix and channels.

4.9 Sensitivity Analysis

The sensitivity of the numerical model to the hydraulic parameters was investigated by varying the parameters from the best estimate values in a series of simulations. In some simulations, several parameters were adjusted to represent different physical waste configurations; in others, a single parameter was varied to determine the sensitivity of the model to that parameter. Generic application rates were used, either high or low, to simplify interpretation of the results. The results of the sensitivity analysis are presented and discussed in the following sections.

For all cases considered for the sensitivity analysis, the height of the waste column was set to 0.80 m. The high infiltration rate was set to 6.0×10^{-6} m/s (21.6 mm/hr) and the low infiltration rate was set to 2.0×10^{-6} m/s (7.2 mm/hr); the 30 minute per day water application period was retained from the detailed simulations, except for Case 7 as discussed below. The parameters used in each simulation are summarized in Table 4.4.

4.9.1 Waste Density

Cases 1 and 2 were used to investigate the sensitivity of the model to changes in waste compaction. The Case 1 parameters were chosen to represent highly compacted waste. Hydraulic conductivities and porosities were decreased, and displacement pressures and residual saturations were increased to reflect the decrease in pore volume and size expected for increased waste density. Conversely, the Case 2 parameters were selected to represent waste with decreased density relative to the Base Case.

The simulation results were much more sensitive to a decrease in waste compaction than to an increase, as illustrated by Figure 4.6. In fact, the Case 1 results are nearly the same as the Base Case results, suggesting that the Case 1 parameters, with minor adjustment, could have been used for the 'best estimate' simulations. The similarity between the Case 1 and Base Case results, despite substantial parameter differences, demonstrates the danger of treating a single set of results as the right answer. As well, these results suggest that the experimental results are likely to be applicable to the highly-compacted waste found at many landfill sites.

Water storage increased significantly relative to the Base Case for all four Case 2 simulations. The increase in hydraulic conductivity resulted in a decrease in water saturation in the channels. However, the decrease in water saturation was insufficient to compensate for the increase in channel porosity. Thus, the moisture content in the channels increased overall, resulting in a slower wetting front and more water transfer to the garbage bags. Furthermore, the high matrix conductivity resulted in

Case	K (m/s)	θ (%)	λ (-)	ψ_d (m)	S_r (-)	K' (m/s)	θ' (%)	λ' (-)	ψ_d' (m)	S_r' (-)	R_0 (m)	F_l (comp.) (s^{-1})	F_l (uncomp.) (s^{-1})
Base	6.0×10^{-4}	2.0	1.0	0.07	0.25	1.2×10^{-7}	50.0	0.65	0.12	0.15	0.20	1.0×10^{-7}	2.0×10^{-6}
1	1.0×10^{-5}	1.0	–	0.14	0.50	1.0×10^{-8}	45.0	–	0.21	0.30	–	–	–
2	1.0×10^{-3}	4.0	–	0.05	0.20	1.0×10^{-6}	55.0	–	0.08	0.10	–	–	–
3	–	–	–	–	–	–	–	–	–	–	–	1.0	N/A
4	–	–	–	–	–	1.0	–	–	–	–	–	–	–
5	–	–	–	–	–	–	–	0.80	–	–	–	–	–
6	–	–	–	–	–	–	–	0.50	–	–	–	–	–
7	*continuous infiltration*												
8	*volume fraction reduced from 0.98 to 0.50*												

Table 4.4: Summary of parameters used for the sensitivity analysis of the dumpster-scale unsaturated flow experiments. Dashes indicate that the base case parameter was used. See text for discussion.

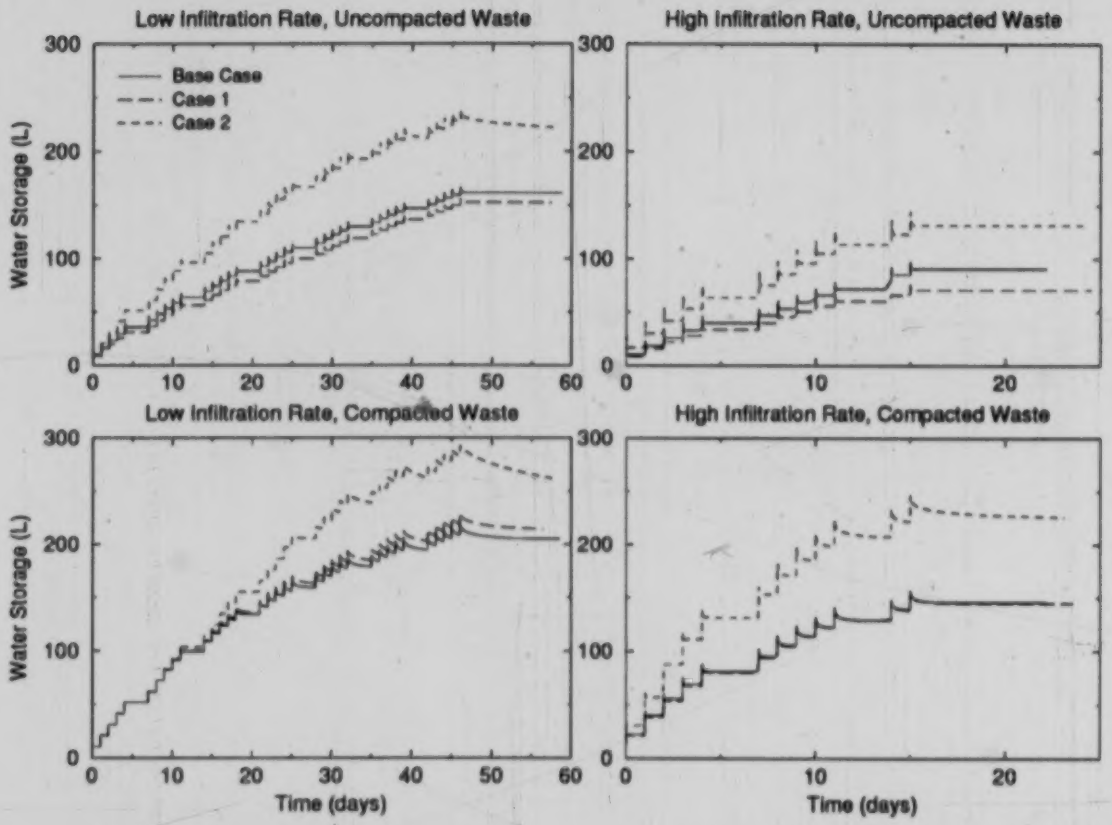

Figure 4.6: Sensitivity of the numerical results to differences in waste density. Case 1 represents highly compacted waste and Case 2 represents extremely low-compaction waste. Refer to Table 4.4 for simulation parameters. Refer to text for discussion.

more rapid movement of water through the garbage bags.

4.9.2 Mode of Water Transfer

Water transfer from the channels to the garbage bag is controlled by two factors: the resistance to water transfer across the channel–bag interface and how fast water is redistributed within a garbage bag. The interface resistance is governed by the fluid-transfer coefficient whereas water redistribution is controlled by the hydraulic conductivity of the matrix.

The numerical results are clearly sensitive to the fluid-transfer coefficient value; otherwise, the compacted-waste simulations would have yielded the same results as the uncompacted-waste simulations. However, the sensitivity to the fluid-transfer coefficient is expected to decrease as the coefficient increases and the channel–matrix interface resistance decreases. For a large enough fluid-transfer coefficient, the interface resistance becomes negligible relative to the redistribution resistance. The Case 3 results (not shown) support the above reasoning. Setting the fluid-transfer coefficient to 1.0 s^{-1} increased water storage only slightly for the compacted-waste cells. Water storage increased by 5% and 19% for the low and high infiltration rate cells, respectively, indicating that most of the resistance to water transfer was due to the slow redistribution of moisture for the compacted-waste cells.

The Case 4 simulations (results not shown) reinforced the above conclusion. The low-compaction cells were about equally sensitive to a large increase in K' (Case 4) as to a large increase in F_t (Case 3). The high-compaction cells behaved like a single-domain system for Case 4; no water was discharged for either the low or high infiltration rate until the storage capacity was exhausted. Moisture redistribution within the waste matrix is therefore important in limiting the rate of channel–matrix water transfer for all combinations of infiltration rate and waste compaction investigated.

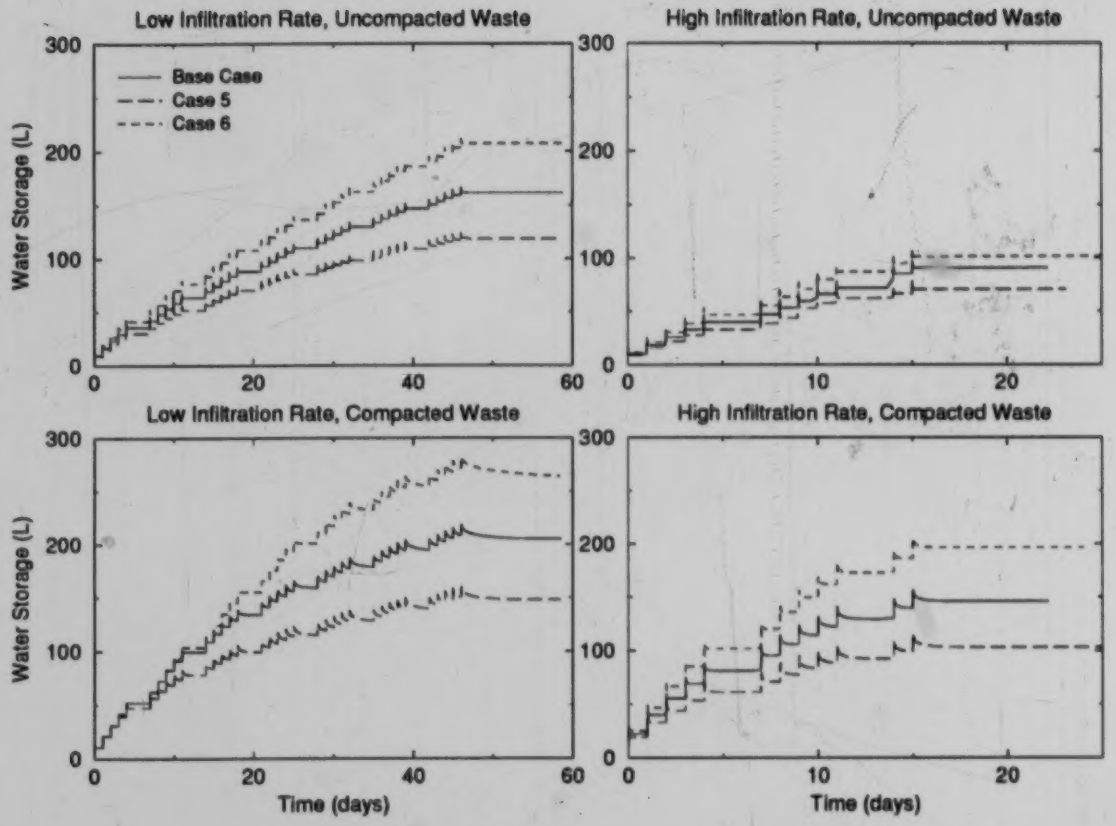

Figure 4.7: Sensitivity of the numerical results to changes in matrix pore-size distribution. The the matrix pore sizes are most uniform for Case 5 and least uniform for Case 6. Refer to Table 4.4 for simulation parameters. Refer to text for discussion.

4.9.3 Matrix Pore-Size Distribution

The matrix pore-size distribution index was varied for Cases 5 and 6 to investigate the influence of this parameter alone on water storage. As illustrated by Figure 4.7, an increase in λ' (Case 5) caused a reduction in water storage and breakthrough time, while a decrease (Case 6) caused an increase in water storage and breakthrough time. The reasons for this behaviour can be deduced from the Brooks–Corey relations, Equations 2.14 and 2.19.

The channel capillary pressure, ψ_c, is not sensitive to λ' at equilibrium. Furthermore, the matrix capillary pressure, ψ_c', tends toward ψ_c over time. Thus, ψ_c' is also insensitive to λ', except possibly at early times. Equation 2.14 relates the effective water saturation to the capillary pressure. Since ψ_c' is essentially unaffected by a change in λ', S_e', and thus the water storage, decreases as λ' increases. Equation 2.19 can be written in terms of the capillary pressure. For the matrix,

$$k_r' = S_e'^{(2+3\lambda')/\lambda'} = \left(\frac{\psi_c'}{\psi_d'}\right)^{-(2+3\lambda')} . \tag{4.5}$$

Equation 4.5 shows that k_r', and thus the rate of water transfer to the matrix, decreases as λ' increases. This decrease in water-transfer rate explains the faster breakthrough time obtained for the high-λ' simulations, relative to the low-λ' ones. The Case 5 and 6 curves could be made to closely match the Base Case curves by adjusting S_r' and ψ_d' to compensate for the change in λ (results not shown). Therefore, while the model is sensitive to the change of a single Brooks–Corey parameter, it is much less sensitive when all three parameters are simultaneously adjusted. Similar reasoning holds for the channel parameters.

4.9.4 Uniform Infiltration Rate

Uguccioni's (1995) experiments involved the periodic addition of water in order to represent natural (nonuniform) rainfall. The numerical simulations performed for the present study represented the water application exactly. However, it is common

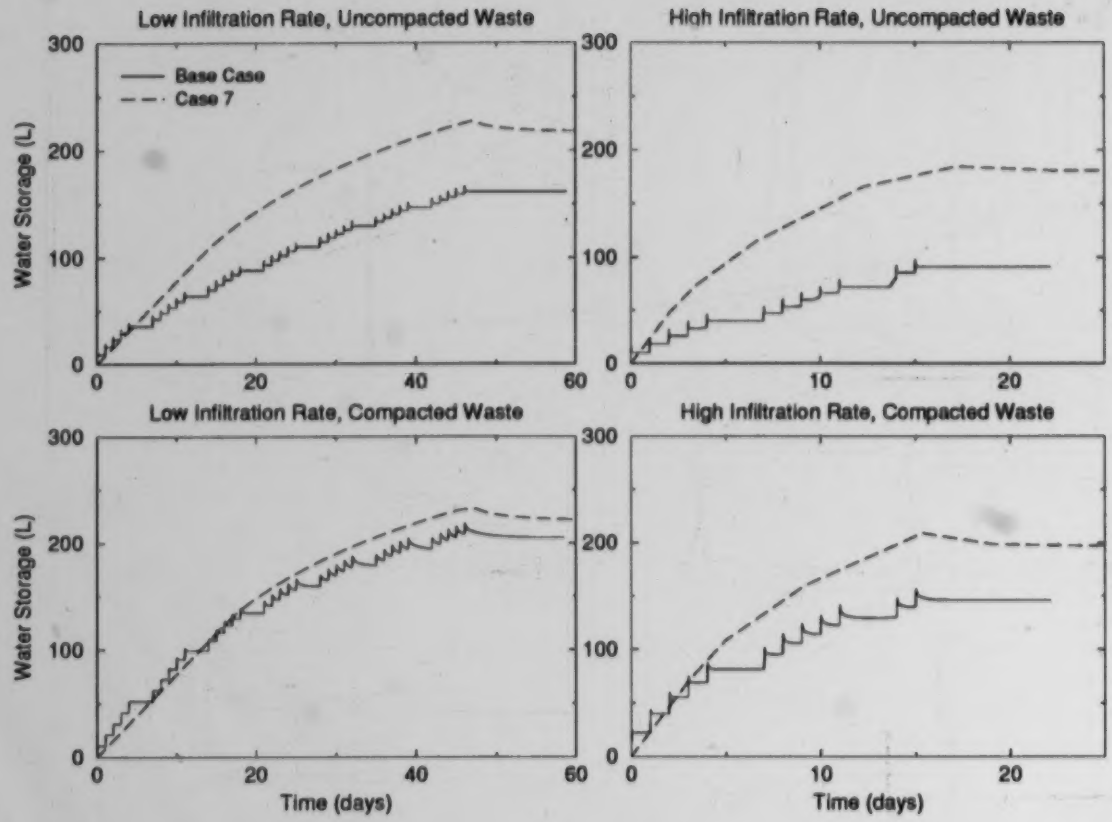

Figure 4.8: Sensitivity of the numerical results to the water-application boundary representation. A uniform water application rate was used in each Case 9 simulation. Refer to text for discussion.

practice in numerical modeling to specify infiltration using constant flux boundary conditions, partly because the exact temporal and spatial distributions of flux, such as rainfall rate over a year, are not known, and partly because of the added computational complexity required to resolve the variable fluxes accurately.

A set of simulations was performed (Case 7) to evaluate the error introduced by steadily adding water to the top of the domain rather than periodically. The total volume of water added to the domain was the same for each Case 9 simulation as for the corresponding Base Case simulation. Nonetheless, water storage and breakthrough times between Case 9 and the Base Case are significantly different (Figure 4.8) except for the high compaction, low infiltration rate simulations, which agree quite well. It should be noted that the Case 9 simulations ran in 20% of the time required for the Base Case simulations. Clearly, it is desirable to use the simplified boundary condition when possible.

The breakthrough time was several days for the Base Case high compaction, low infiltration rate simulation. Thus, the rate of transfer of water from the channels to the matrix was less sensitive to the exact representation of water application than for the other simulations. Therefore, the breakthrough time should be used to determine the resolution required for the accurate simulation of time-varying infiltration rates.

4.9.5 Matrix Accessibility

Intact plastic garbage bags are impermeable to water. Therefore, if some fraction of the garbage bags in a dumpster were free from rips, the volume fraction of the matrix would be reduced. The experimental cells containing uncompacted waste (Cells 1, 3, 5, and 7) may have contained some intact bags. In that case, the effective fraction of the bulk porous medium volume occupied by the secondary domain (V_s^*) would be reduced. Case 8 was designed to investigate the influence of V_s^* on the system behaviour.

Water storage for the Case 8 simulations was halved for all four combinations of waste compaction and infiltration rate relative to the Base Case (results not shown),

indicating that the relationship between V_s^* and water storage is essentially linear. Breakthrough times were also somewhat faster. The volume fraction of the matrix could have been reduced for the low-compaction cell simulations as an alternative to reducing the fluid-transfer coefficient. The water storage versus time plots would have been the same shape as the high-compaction simulations, but with reduced water storage. Some of the experimental curves (Figures 4.2 and 4.4) are rounded while others are quite sharp; it is not clear which approach is more appropriate.

4.10 Summary

This chapter presented an application of C-Flow to a moisture movement experiment. The experiment was designed to explore the importance of channelled flow in municipal solid waste, using a set of eight dumpster-scale flow cells. The experimental results showed that flow was characterized by rapid breakthrough followed by substantial increases in water storage over time. Water application rate and waste compaction were identified as key parameters influencing moisture flow through solid waste.

C-Flow was used to simulate the experiments. The numerical model was able to reproduce the experimental results reasonably well. The good agreement between experiment and model suggests that the model captures the essence of flow through waste at the dumpster scale despite the many simplifications needed to formulate a tractable mathematical description of the flow processes.

Results from the sensitivity analysis led to several conclusions:

- matrix hydraulic conductivity, K' is the main parameter controlling the rate of water storage at the dumpster scale;
- the model is sensitive to variations in individual Brooks-Corey parameters, although not necessarily to variations in the Brooks-Corey parameters as a group;

- the waste used in the experiments seems to be representative of the highly compacted waste that would be found in a typical modern landfill; and
- finer resolution of water application rate is required for shorter breakthrough times for the accurate simulation of water flow through a two-domain porous medium.

Future experimental programs should address the lack of detailed measurement of the key water flow parameters. Saturated hydraulic conductivity should be measured for both the bulk medium and for the finer-textured waste within the garbage bags. Unsaturated flow relationships also need to be experimentally determined. The usefulness of a numerical model as a predictive tool is greatly hampered when physical parameters have not been measured. Furthermore, the capillary-pressure measurement method should be modified to ensure that accurate capillary pressure data is obtained.

Chapter 5

Illustrative Examples

Two applications of C-Flow are presented in this chapter to illustrate potential uses of the model at the field scale. The first example considers water movement and biodegradation of waste within a landfill. The second example illustrates groundwater contamination of an unconfined aquifer from an unlined landfill site. Neither example is based on a particular field site; rather, the examples are intended to show some of the capabilities of C-Flow using realistic flow and transport parameters.

The results presented below should not be used to make any landfill site design or operational decisions. Site specific, landfill-scale data is required before C-Flow can be reliably used as a decision making tool for any particular landfill.

5.1 Landfill-Scale Application

In the first example, the life of a landfill is simulated in two phases: waste accretion, followed by stabilization. During the accretion phase, waste is added to the landfill in annual four metre increments over six years, resulting in a total of 24 m of waste being emplaced. During the stabilization phase, the waste gradually decomposes. Four waste-stabilization scenarios are presented in order to explore the influence of infiltration, pumping, and leachate recirculation on waste decomposition rates. The landfill site is assumed to be underlain by a 4 m thick water-saturated clayey aquitard.

5.1.1 Domain Definition

The domain is defined to represent a cylindrical portion of a landfill. The waste layer grows from a height of 4 m at the beginning of the active landfilling phase to a final height of 24 m at the end of the active landfilling phase. Since waste compaction is not represented by C-Flow, the waste layer thickness should be taken as a time-weighted average or perhaps a final compacted thickness. The radius of the domain is 50 m to allow for the representation of pumping during the stabilization phase. Wells are presumed to be regularly spaced 100 m apart throughout the landfill. Thus, the radius of influence for any well is one half of the well spacing, or 50 m.

The well spacing was calculated using a method suggested by Rowe and Nadarajah (1996). They provide diagrams to estimate the maximum well spacing required to limit the maximum hydraulic head buildup, or leachate mound, to an acceptable level based on the well radius, infiltration rate, and hydraulic conductivity. The 100 m well spacing was chosen to limit the leachate mound to a maximum height of 1 m.

The domain is discretized with 57 rows and 21 columns of nodes, for a total of 1197 nodes connected by 2240 triangular (axisymmetric) finite elements. The vertical node spacing is 0.5 m. The horizontal spacing increases exponentially from 0.1 m at the axis of rotation to 4.3 m over the first 10 spaces; uniform spacing of 4.3 m is used for the last 10 increments.

Highly transmissive line elements are placed at a radius of 0.4 m from the top of the aquitard ($z = 4$ m) to the top of the landfill ($z = 28$ m) to represent a pumping well which is used during the waste stabilization period. Thus, a total of 48 0.5 m high line elements are used to represent the pumping well. Due to the high transmissivity of the line elements, a negligibly small hydraulic head gradient is required for water flow along the elements.

5.1.2 Waste Properties

The waste properties are summarized in Table 5.1. The moisture movement parameters are based on the dumpster-scale results summarized in Table 4.2, but have been modified to reflect the lower hydraulic conductivity and greater heterogeneity typical of the landfill scale (Oweis *et al.*, 1990). Biodegradation parameters are based on values derived from a literature review. Table 5.2 summarizes the observed parameter ranges and the sources of literature information.

The range for biological oxygen demand (BOD) reported in the literature must be converted into an equivalent DOC concentration range to compare with C-Flow results. Theoretically, each mole of organic carbon (C) requires one mole of oxygen (O_2) for complete oxidation to carbon dioxide (CO_2). Therefore, 32 mg/ℓ of BOD is equivalent to 12 mg/ℓ of C, resulting in the relationship DOC = 0.375 $\times$ BOD.

5.1.3 Flow Boundary Conditions

The bottom of the clayey aquitard is defined as a fixed-head boundary. The hydraulic head is set to 1.0 m to represent the top of a confined aquifer. The lateral boundaries are symmetry boundaries, i.e. no flow or zero gradient boundaries. The top of the waste layer is a fixed-flux boundary to represent infiltration of water from the land surface. The infiltration rate is taken to be 1.0 mm/day (365 mm/year).

Waste accretion is handled by specifying which finite elements are to be active at any time. Elements are deactivated until the waste they represent has been added to the landfill. Each year of simulation time, another four metres of elements are activated. The upper boundary condition is adjusted each year so that it is always at the active waste surface. All of the elements used to represent the pumping well are deactivated for the entire waste accretion period because no pumping takes place during this stage.

The landfill site has a 1.6 m thick leachate mound at the end of the accretion period due to infiltration during waste addition. Four scenarios are simulated for the

Flow Parameters

Parameter	Units	Channel	Matrix	Liner
K_r	(m/day)	2.0	0.01	1.0×10^{-5}
K_z	(m/day)	1.0	n/a	1.0×10^{-6}
S_s	(m^{-1})	1.0×10^{-5}	1.0×10^{-5}	1.0×10^{-4}
θ	(%)	2.0	50.0	50.0
λ	(-)	0.65	0.65	n/a
ψ_d	(m)	0.1	0.12	n/a
S_r	(-)	0.25	0.15	n/a
R_0	(m)	n/a	0.20	n/a
F_t	(day^{-1})	n/a	0.10	n/a

Transport Parameters

Parameter	Units	Channel	Matrix	Liner
D_w	(m^2/day)	7×10^{-5}	7×10^{-5}	7×10^{-5}
α_l	(m)	4.0	0.02	4.0
α_t	(m)	0.4	n/a	0.4

Biodegradation Parameters

Parameter	Units	Channel	Matrix	Liner
M_t	(day^{-1})	n/a	1×10^{-3}	n/a
κ_a	(day^{-1})	n/a	2×10^{-3}	n/a
κ_p	(day^{-1})	n/a	5×10^{-4}	n/a
μ	(day^{-1})	1.0	1.0	1.0
K_C	(mg/ℓ)	20 000	20 000	20 000
Y_C	(-)	0.73	0.73	0.73
Y_X	(-)	0.02	0.02	0.02
Y_O	(-)	0.27	0.27	0.27
Y_I	(-)	0.0	0.0	0.0
κ_d	(day^{-1})	0	0	0

Initial Conditions

Parameter	Units	Channel	Matrix	Liner
$B_{0,a}$	(kg/m^3)	0.0	20.0	0.0
$B_{0,p}$	(kg/m^3)	0.0	10.0	0.0
X_0	(kg/m^3)	1.0×10^{-3}	1.0×10^{-2}	1.0×10^{-4}

Table 5.1: Summary of parameters used for the landfill-scale illustrative example

Parameter	Range	References
κ	$10^{-4} - 10^{-2}$ day^{-1}	Gönüllü (1994) Gurijala and Suflita (1993) Marticorena *et al.* (1993) Arigala *et al.* (1995) Nozhevnikova (1993)
μ	*fitting parameter*	
K_C	10 000 mg/ℓ	Lee *et al.* (1993)
Y_C	0.73	Barlaz *et al.* (1990)
Y_X	$0 - 0.05$	Barlaz *et al.* (1990)
Y_O	0.27	Barlaz *et al.* (1990)
Y_I	0.0	Barlaz *et al.* (1990)
κ_d	$0 - 0.022$ day^{-1}	Lee *et al.* (1993)
$\rho_{b,d}$*	$320 - 600$ kg/m^3	Uguccioni (1995) Gönüllü (1994) Nozhevnikova (1993)
B_0	3% – 10% of dry mass ($10 - 60$ kg/m^3)	Farquhar (1989) Attal *et al.* (1992) Marticorena *et al.* (1993) Owens and Chynoweth (1993)
X_0	$0.002 - 0.02$ kg/m^3	Gönüllü (1994) Barlaz *et al.* (1990)
time to max. C	80 days – 5 years	Farquhar (1989) Ross (1990)
max. BOD	$4 - 40$ g/ℓ	Farquhar (1989)

*dry bulk density (used to calculate B_0)

Table 5.2: Summary of biodegradation parameters from the literature

ensuing stabilization period:

1. Passive stabilization (Nonpumping);
2. Leachate recirculation (Recirculation);
3. Leachate extraction (Pumping); and
4. Leachate extraction with no infiltration (No Infiltration).

In all four cases, a clay cap is assumed to be installed at the end of the waste accretion period. For the first three cases, the cap is assumed to leak uniformly at a constant rate of 1.0 mm/day. For the fourth case, the cap is assumed to be impermeable to water.

For all but the nonpumping case, water is removed from a single node at the bottom of the well. As described above, water flows down the well bore along the high-transmissivity line elements. The node is a threshold pressure head node. The maximum pressure head in the well is limited to 0.1 m above the top of the aquitard. Water is automatically pumped from the well at a rate sufficient to maintain this pressure head.

For the leachate recirculation case, the extracted leachate is applied uniformly to the top of the landfill in addition to the infiltrating water. It is assumed that the leachate is mixed completely and that appropriate pH buffers are used to maintain a uniform near-neutral leachate pH.

5.1.4 Transport Boundary and Initial Conditions

Leachate outlet boundaries have a zero chemical gradient (Type II). Inlet boundaries are specified total flux (Type III). Infiltrating water has a zero DOC concentration, while the DOC concentration of recirculated leachate is the same at the injection nodes as at the extraction node. Initial bulk biodegradable solids concentrations ($B_{0,a}$ and $B_{0,p}$) and initial biomass concentrations (X_0) are summarized in Table 5.1.

5.1.5 Simulation Results

Waste Accretion

Figure 5.1 illustrates vertical profiles of simulated DOC concentration at the end of each year. Since no pumping takes place during the accretion period, the concentration profile is the same at all radii. Notice that the waste column grows by four metres per year. The profiles appear to be very similar to each other, with each curve translated up 4 m from the previous year. The reason is that the waste is added in annual increments, so the top of the waste layer moves up by 4 m each year, producing the same conditions for the new waste each year.

This behaviour is clearly shown by Figure 5.2 which illustrates DOC concentration as a function of time since waste emplacement for each of the six waste layers. The curves closely follow one another, with concentrations increasing for about the first year and a half to a maximum DOC concentration of about 4 000 mg/ℓ, and then gradually decreasing. The secondary hump at year two comes from the influx of high-strength leachate from the waste layer above. The uppermost layer (Layer 6) lacks this secondary hump because there is no additional waste layer above.

The biodegradation parameters used for this simulation (Table 5.1) were selected in order to produce realistic DOC concentration versus time curves (Farquhar, 1989; Ross, 1990 – see Table 5.2). The maximum DOC concentration in the waste ranges from 2800 to 4000 mg/ℓ and is reached at a time from about eleven to fifteen months (Figure 5.2). Thus, the simulated results are reasonable.

Waste Stabilization

Vertical DOC concentration profiles for all four waste stabilization cases at a radius of 5.7 m from the centre line of the domain are illustrated in Figure 5.3. Concentration profiles at different radii are very similar because leachate movement is essentially vertical in the unsaturated zone that constitutes most of the domain. Therefore, concentration profiles at other radii are not shown.

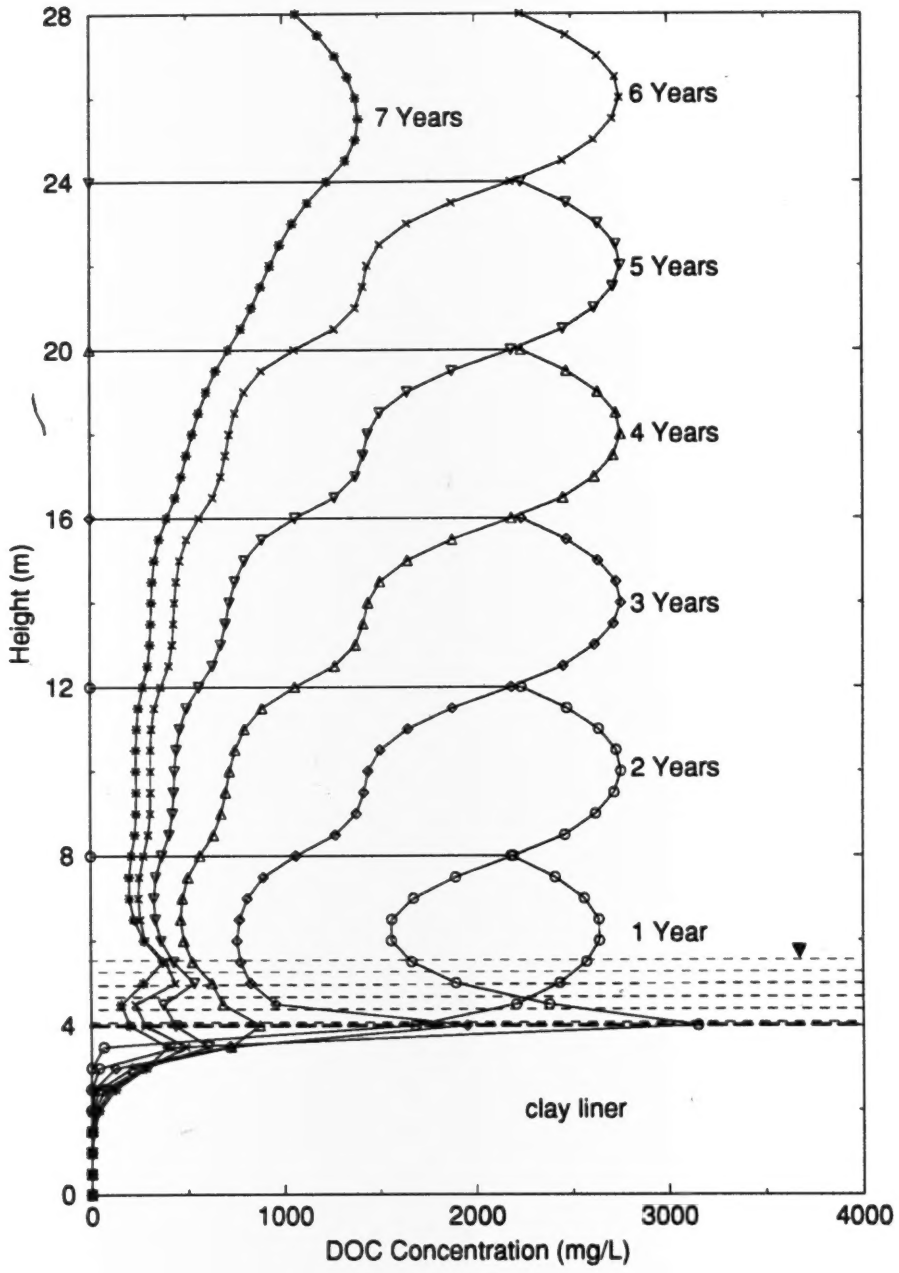

Figure 5.1: Annual profiles of DOC versus z during the waste accretion period. Dashed lines show the position of the water table at 2, 3, 4, 5, 6, and 7 years, from bottom to top. The waste is unsaturated during the first year.

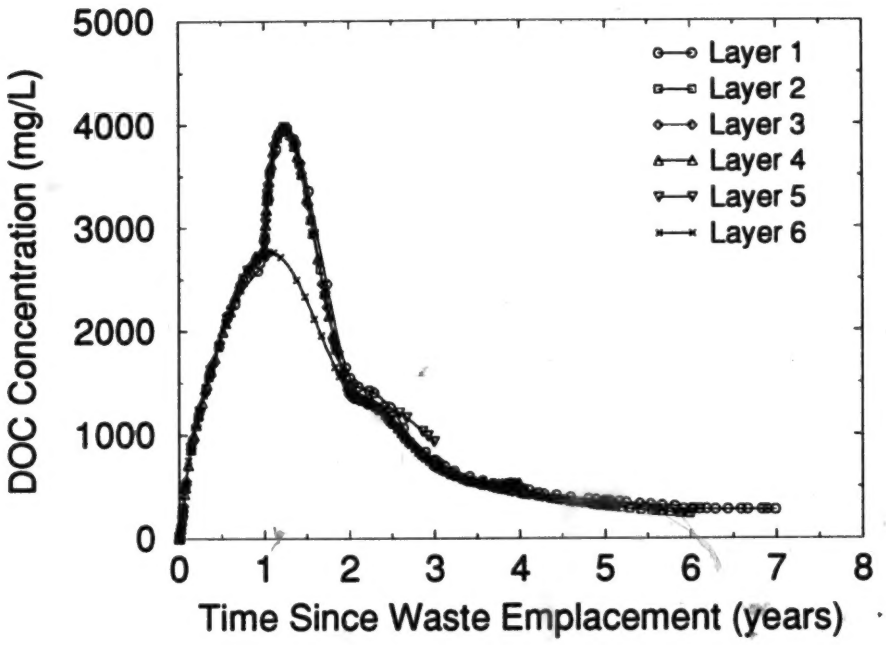

Figure 5.2: DOC concentration as a function of time since waste emplacement at the midpoint of each annual waste layer

All four plots are similar, but some variability is evident. The nonpumping case (Figure 5.3a) plot has relatively high concentrations at the base due to the accumulation of a leachate mound. The no infiltration case (Figure 5.3d) has the most variable vertical concentration gradients due to the lack of infiltration to smear the concentrations. The recirculation case (Figure 5.3c) has the most intense infiltration as well as DOC input at the top of the waste layer and hence the most uniform distribution of DOC.

Figure 5.4 compares DOC concentrations in the lowermost waste layer versus time for the four stabilization scenarios. Figure 5.5 illustrates DOC concentrations for two cases over a longer period for the lowermost (Layer 1) and uppermost (Layer 6) waste layers as well as for the aquitard. Other than the nonpumping case, the concentrations all follow the same trend for the first year of stabilization. Subsequently, the concentrations diverge, with the recirculation case having the highest concentrations and the no infiltration case having the lowest.

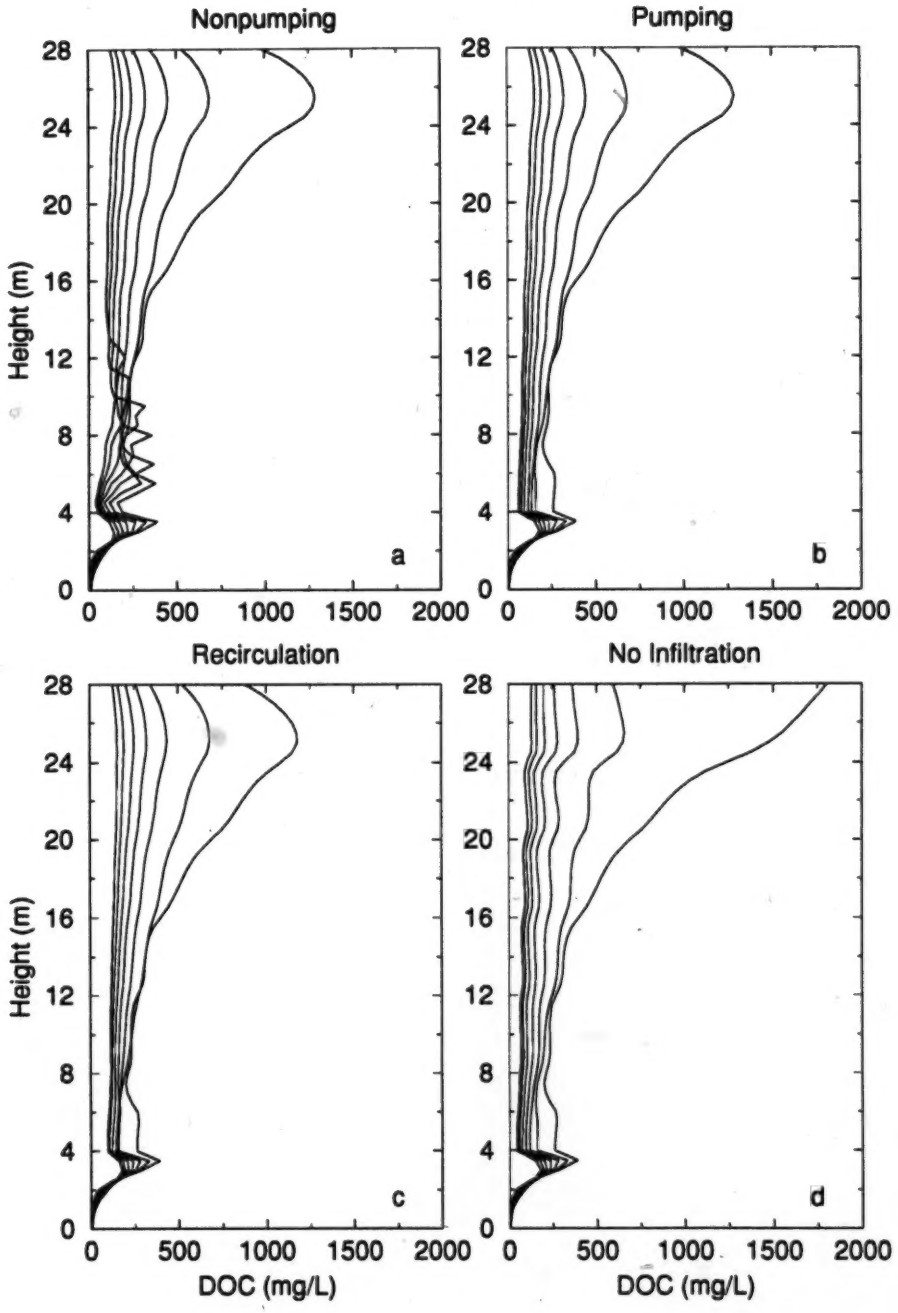

Figure 5.3: Profiles of DOC concentration versus z during the stabilization period for all four stabilization scenarios. Profiles are taken 5.7 m from the axis of rotation at times of 30 days, 1, 2, 3, 4, 5, and 6 years after the start of the stabilization period. Concentrations in each plot decrease with time.

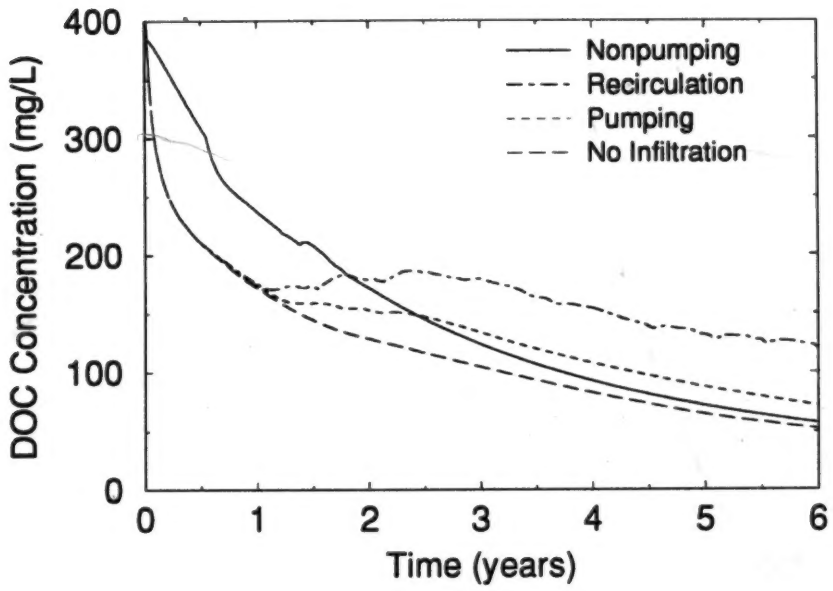

Figure 5.4: DOC concentration in the bottom waste layer at a radius of 5.7 m as a function of time for all four waste stabilization scenarios.

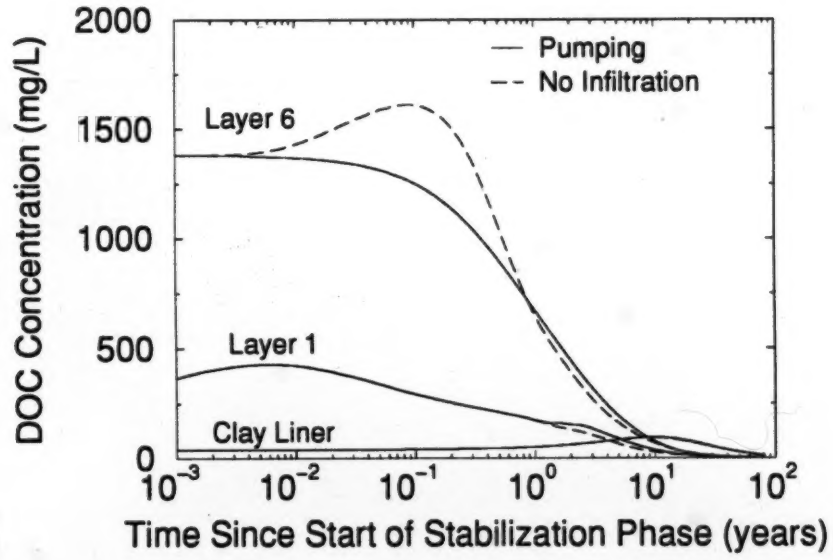

Figure 5.5: DOC concentration as a function of time for the pumping and no infiltration stabilization scenarios. The radius is 5.7 m. Layer 1 is the bottom waste layer (emplaced at the start of year 1) and layer 6 is the uppermost waste layer (emplaced at the start of year 6).

Case	$B_a/B_{0,a}$	$B_p/B_{0,p}$	X/X_0	X'/X'_0
1. Nonpumping	0.16	0.57	1.5	2.6
2. Recirculation	0.16	0.57	1.5	2.6
3. Pumping	0.18	0.59	1.4	2.5
4. No Infiltration	0.21	0.61	1.4	2.4

Table 5.3: Comparison of solids consumption ($B_a/B_{0,a}$ and $B_p/B_{0,p}$) and biomass production (X/X_0 and X'/X'_0) for the four stabilization scenarios after seven years of waste stabilization. See text for discussion.

The nonpumping case has the highest initial concentrations, but also has the most rapid initial biodegradation. Therefore, the the concentrations drop below those for the recirculation case after about two years of stabilization.

Differences in DOC concentrations arise from differences in biodegradation rates between the scenarios. The moisture content is highest for the nonpumping case; therefore, solids biodegradation is also the highest. Conversely, the case with no infiltration has the lowest moisture content, hence the slowest biodegradation rate.

The speed of biodegradation can be inferred from Table 5.3 which summarizes the biodegradable solids consumption and biomass production after six years of waste stabilization. The smallest ratio of B/B_0 and largest ratio of X/X_0 indicates the fastest biodegradation. The differences in the numbers are relatively small, indicating that the overall simulated landfill biodegradation rate is not very sensitive to the choice of stabilization scenario. Possible reasons for this low sensitivity will be discussed in the next section.

5.1.6 Discussion

The model produced reasonable curves of DOC concentration versus time using model parameters based on the literature survey described above. For the parameters chosen, waste biodegradation was the major control on the distribution of DOC, with advection and dispersion having less influence.

Hydraulic and chemical coupling between the two model domains was quite

strong. This strong coupling suggests that an equivalent single domain could likely be defined that would give realistic results. The single-domain modeling approach is preferred when reasonable due to the greatly reduced computational burden. On the other hand, large-scale heterogeneities, such as regions of construction debris and heterogeneities caused by seasonal variations in the waste-input stream, are certain to influence leachate movement and waste biodegradation at the landfill scale. This large-scale structure of waste needs to be characterized in order to improve the understanding of waste stabilization processes.

The low model sensitivity to the various waste stabilization scenarios was somewhat surprising. Much of this low sensitivity likely came from limitations in the numerical model. The waste was treated as a homogeneous two-domain porous medium for this illustrative example. As discussed above, the waste at a landfill site is typically a highly heterogeneous mixture of household garbage, yard waste, construction debris, etc. C-Flow is able to handle heterogeneous waste properties, but field data are required in order to incorporate waste heterogeneity into a physically-realistic model.

A second factor that reduces model sensitivity is the constitutive relationship between moisture content and biodegradation rate. The biodegradation rate is assumed to be linearly proportional to the moisture content in C-Flow. The biodegradation rate may actually be a much stronger function of the moisture content. It will be necessary to study experimental waste biodegradation data to improve this constitutive relationship.

5.2 Regional-Scale Application

The second example illustrates the potential for an unlined landfill site to contaminate groundwater. The domain geometry is adapted from Cooley (1983), based on the work of Winter (1976) in the Finger Lakes region of New York State. Figure 5.6 illustrates the domain geometry and the hydraulic head distribution. The dimensions are the same as those used by Cooley (1983) except that here the dimensions

Flow Parameters

Parameter	Units	Aquifer	Lake Bed	Landfill
K_x	(m/day)	15	1×10^{-4}	15
K_z	(m/day)	0.03	1×10^{-7}	0.03
θ	(%)	25	25	25

Transport Parameters

Parameter	Units	Aquifer	Lake Bed	Landfill
D_w	(m^2/day)	7×10^{-5}	7×10^{-5}	7×10^{-5}
α_l	(m)	4	4	4
α_t	(m)	0.4	0.4	0.4

Biodegradation Parameters

Parameter	Units	Aquifer	Lake Bed	Landfill
κ_a	(day^{-1})	n/a	n/a	2×10^{-3}
κ_p	(day^{-1})	n/a	n/a	5×10^{-4}
μ	(day^{-1})	1	1	1
K_C	(mg/ℓ)	20 000	20 000	20 000
Y_C	(-)	0.73	0.73	0.73
Y_X	(-)	0.02	0.02	0.02
Y_O	(-)	0.27	0.27	0.27
Y_I	(-)	0.0	0.0	0.0
κ_d	(day^{-1})	0	0	0

Table 5.4: Summary of parameters used for the regional-scale illustrative example. See text for a description of the problem.

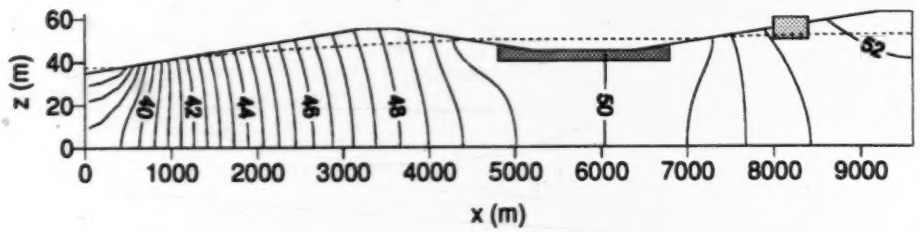

Figure 5.6: Hydraulic head distribution for the regional-scale illustrative example. Equipotentials are shown by the solid lines with values of hydraulic head indicated in metres. The contour interval is 0.5 m. The dashed line shows the position of the water table and surface water bodies.

are given in metres rather than feet. The result is that the length scales for the present example are a factor of 3.3 larger than the true values.

The region of interest is a cross-section through an unconfined aquifer. The domain ranges from a regional topographic low on the left to a regional high on the right. The domain encompasses a local topographic high and a local low. The lows form long, narrow lakes, with the cross-sectional slice taken midway down the lakes, perpendicular to their long axes. The hypothetical landfill site is also assumed to be long in the direction perpendicular to the page. The domain is composed of three units: an unconfined sandy aquifer, silty sediments underlying the upper lake, and the landfill site. The porous medium properties for the three units are summarized in Table 5.4.

5.2.1 Flow Boundary Conditions

The boundary conditions used to obtain the illustrated flow field differ somewhat from those used by Cooley (1983). Cooley assumes that infiltration occurs only on the tops and upper slopes of the hills, while the current model assumes that infiltration occurs everywhere except for the constant head boundaries and active seepage faces. Therefore, flow is somewhat more intensive through the model used for this example. The hydraulic head distribution is not affected much by these relatively minor differences in boundary condition definition.

The lateral domain boundaries are symmetry boundaries; that is, the flow-field and hydraulic-conductivity distributions are considered to be mirrored across the left and right lateral boundaries. In practice, the symmetry-boundary condition is a reasonable approximation as long as the the boundary falls on the centreline of a regional topographic low or a regional topographic high and no significant heterogeneities are present in the immediate vicinity. The bottom boundary is a no-flow boundary, representing a low-permeability barrier to water flow. The top of the domain has a uniform infiltration rate of 0.4 mm/day except where the water table intersects the land surface. A lake extends from $x = 0$ to 400 m with a surface elevation of 37.5 m above the bottom of the aquifer. A second lake extends from $x = 4400$ to 7200 m with a surface elevation of 50 m. Elsewhere on the top boundary, seepage faces form everywhere the water table reaches the land surface.

5.2.2 Transport Boundary and Initial Conditions

The boundary conditions for the transport solution are zero gradient (Type II) on the no-flow and water outlet boundaries (i.e., where water exits the domain) and zero total flux (Type III) on the water inlet boundaries. The initial concentration of bacteria is 10 mg/ℓ within the landfill site and 0.1 mg/ℓ everywhere else. The initial biodegradable solids concentrations in the landfill site are 20 kg/m^3 for the accessible solids and 10 kg/m^3 for the protected solids. All other initial concentrations are zero.

5.2.3 Simulation Results

The steady-state flow solution illustrated in Figure 5.6 was obtained for the boundary conditions described above. This flow field was used for the subsequent transport simulation. The transport solution is presented in Figure 5.7 as a series of snapshots. As the solid organic carbon initially present in the landfill decomposes, it produces carbon dioxide and methane, as well as dissolved organic carbon which is transported to the regional aquifer by the water percolating through the landfill site. Simultaneously, the bacteria in the landfill and in the aquifer further break down the dissolved

organic carbon to carbon dioxide and methane.

Dissolved organic carbon is transported down into the aquifer and along the aquifer for approximately twenty years before contaminated groundwater begins to discharge to the upper lake. The deeper portion of the plume continues to move laterally for decades as it slowly biodegrades. Note that DOC concentrations greater than 1 mg/ℓ persist throughout the aquifer beneath the upper lake even after 200 years. It must be stressed that these results, although based on realistic parameters, must be interpreted with extreme caution considering the absence of field data.

Within the landfill itself, the dissolved organic carbon concentration increases rapidly, reaching a maximum of 6200 mg/ℓ after 340 days of simulation (Figure 5.8). The concentration decreases quite rapidly from 1 to 2 years as the biodegradable solids concentration decreases, reducing the rate of mass input to the aqueous phase, and as the biodegradation rate increases due to the growing microbial population. Low DOC concentrations persist in the landfill site for many years due to continuing biodegradation of the protected solid organic carbon. The simulated concentrations for this problem are within the range suggested by Farquhar (1989) for field conditions.

5.2.4 Mass Fate

The detailed mass balance calculations performed by C-Flow can be used to determine the fate of the biodegradable organic carbon. Of the 30 kg/m^3 of biodegradable solid organic carbon initially present in the landfill, more than 98% was biodegraded to methane (63%) and carbon dioxide (36%) for the biodegradation and transport parameters used in the simulation. Of the remaining mass, 1.5% was transformed to biomass and 0.4% was discharged to the upper lake. Less than 0.1% of the initial mass remained as biodegradable solids or dissolved organic carbon after the 200 year simulation period, indicating that the dissolved organic carbon remaining after 200 years is insignificant to the mass balance. The overall mass balance error for the domain over the entire simulation was 0.35 grams of organic carbon, which is negligible

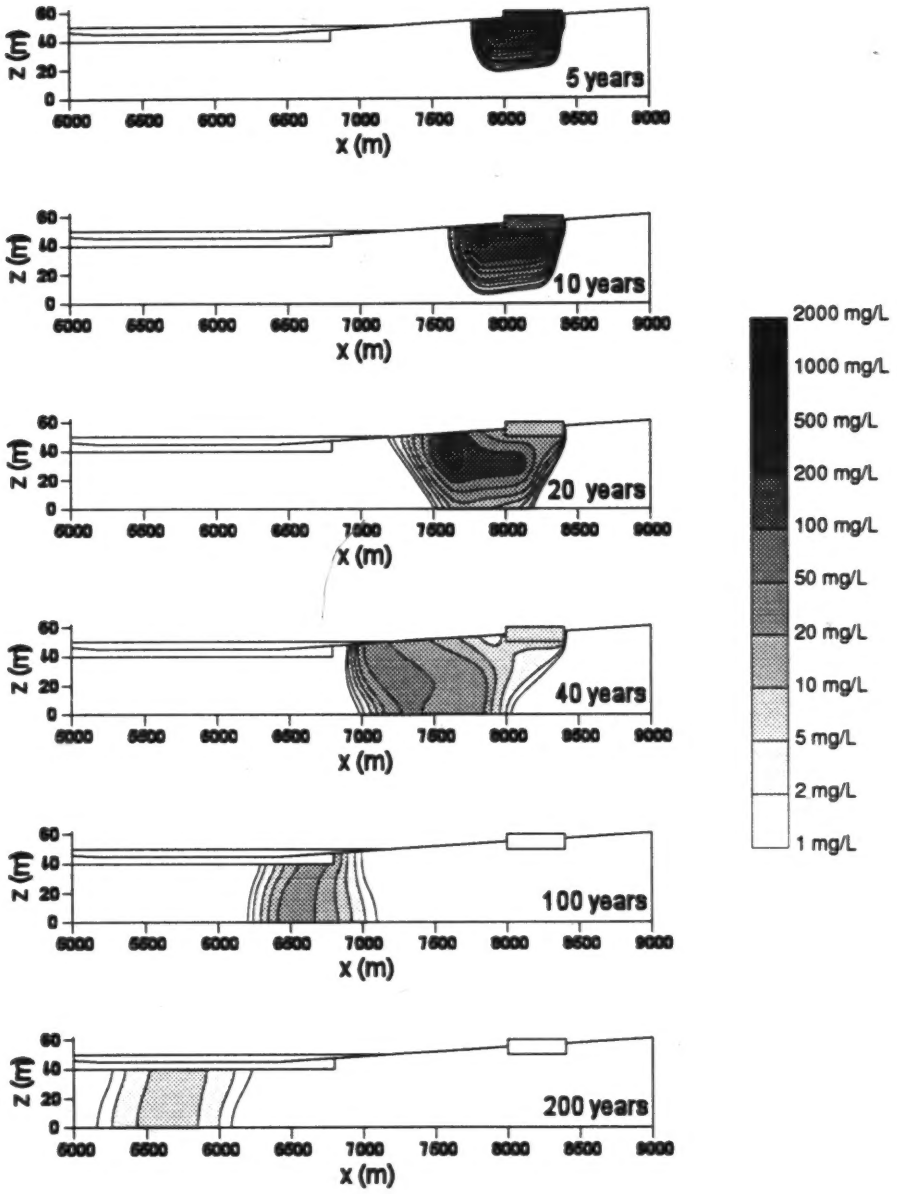

Figure 5.7: DOC concentrations for the regional-scale example. Only the right-hand side of the domain shown in Figure 5.6 is illustrated

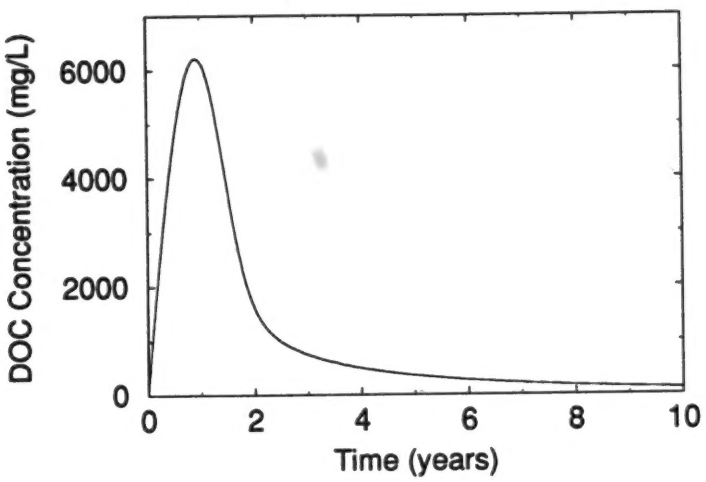

Figure 5.8: DOC concentration within the landfill site versus time

compared to the 1.2×10^5 kg of solid organic carbon biodegraded.

Figure 5.9 illustrates the rate of DOC discharge to the upper lake as a function of time. The contaminant plume first reaches the lake at year 18, with the discharge rate attaining a peak of 41 g/day per metre of shoreline (into the page) at year 33. The mass discharge rate then gradually tails off over the next 100 years. It is likely that the dissolved organic carbon is discharged sufficiently slowly in this simulation to be rapidly diluted by lake water to negligible concentrations.

5.3 Summary

Two applications of C-Flow were presented in this chapter to illustrate some of the capabilities of the model. The model can represent complex boundary conditions and irregular two-dimensional domain geometries. C-Flow simulates simultaneous transient water flow, unretarded dissolved organic carbon transport, and anaerobic biodegradation in variably-saturated porous media. The model allows single-domain and two-domain porous media to be mixed in a single simulation. Time-varying domain configurations and boundary conditions are also readily handled.

In the first example application, C-Flow was used to simulate waste accretion

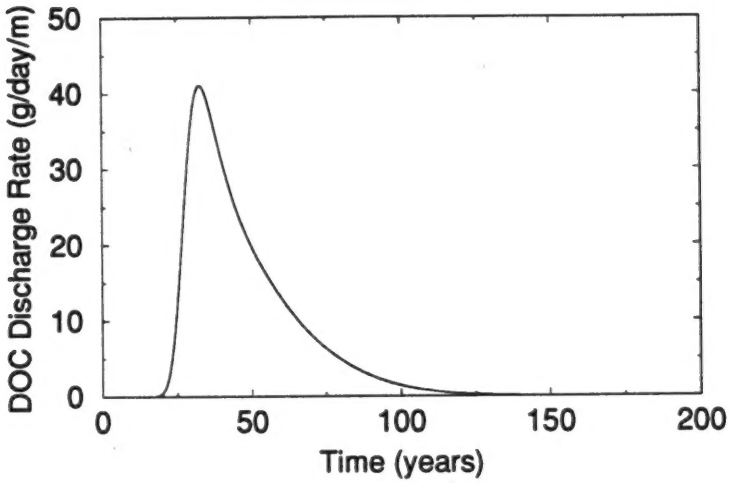

Figure 5.9: DOC discharge rate to the upper lake as a function of time

and subsequent biodegradation and leachate movement at a landfill site. The surprisingly low sensitivity to different stabilization scenarios highlighted the need for better characterization of waste at the landfill scale and for an improved constitutive relationship between moisture content and biodegradation rate. The results also suggested that the dual-porosity formulation may be unnecessary at the landfill scale; larger-scale heterogeneities likely control the distribution and movement of leachate through waste at a landfill site. These conclusions also imply that moisture movement and waste biodegradation experiments need to be conducted at scales larger than that of a dumpster.

In the second example application, the model was used to simulate waste biodegradation and dissolved organic carbon transport through an aquifer underlying an unlined landfill site. For the domain geometry and waste and aquifer properties used in the simulation, DOC concentrations reached a maximum of greater than 1000 mg/ℓ in the aquifer, but the impact to a lake about 1 km downgradient due to the DOC plume was relatively minor. Of course, landfill sites typically contain a variety of hazardous substances which have the potential to cause severe groundwater and surface water contamination. These substances would need to be considered individually.

In both illustrative examples, DOC concentrations within the waste followed the

trends reported in the literature, using biodegradation parameters within the reported ranges. Therefore, the conceptual model of anaerobic biodegradation developed for this thesis seems to be appropriate at the landfill scale. However, it will be necessary to compare results from C-Flow to at least one detailed biodegradation experiment before the model is ready to be used as a predictive tool for landfill site design or management.

Chapter 6

Conclusions

Much of the world's waste is disposed of in landfill sites. Therefore, the processes that occur during municipal solid waste (MSW) biodegradation need to be studied. Although modern North American landfill sites are usually designed to prevent biodegradation, some waste decomposition is inevitable. Over time, the caps and liners used in the design of these landfill sites may leak, allowing surface water to infiltrate into the waste or allowing leachate to escape from the landfill site. Older landfill sites may have no caps or liners, increasing the risk of leachate generation within and leakage from the landfill sites. By studying moisture movement and biodegradation in MSW, the potential intensity and duration of groundwater contamination from landfill sites can be predicted and various design and management schemes evaluated.

In this thesis, conceptual models of the structure of MSW, water flow through the waste, and waste biodegradation were developed. These models were based on experimental and field observations at scales ranging from the bench top to the landfill site. Solid waste was treated as a two-domain continuum; waste-filled garbage bags were assumed to provide most of the water storage capacity of household waste, while the channels between the garbage bags were assumed to rapidly transmit water through waste. Fluid was assumed to be transferred between the two domains by leakage through tears in plastic garbage bags or by diffusion through paper bags.

A two-step model of anaerobic waste biodegradation was developed. Biodegrad-

able solids were assumed to be converted to soluble organic carbon (fatty acids and alcohols), carbon dioxide, and methane by the combined processes of hydrolysis and fermentation. The subsequent rate-limited transformation of dissolved organic carbon (DOC) to carbon dioxide and methane by methanogenic bacteria was also considered. Unretarded transport of DOC by advection and dispersion was accounted for as well. Aerobic biodegradation was not explicitly accounted for since oxygen initially emplaced with the waste in a landfill is rapidly consumed and replenishment of oxygen in the waste is typically limited to the margins of a landfill site.

The conceptual models were used to formulate a set of partial differential equations to quantify the description of water flow and biodegradation in MSW. These equations were implemented in a numerical simulator called C-Flow. The model represents transient, variably-saturated water flow, biodegradation of solid organic carbon, and transport of DOC through a two-dimensional cross section using either Cartesian or axisymmetric coordinates.

Although this thesis focused on processes occurring during waste biodegradation, the mathematical and numerical models that were developed here could readily be applied to other settings. A model verification problem involving pumping from a fractured rock aquifer was one example of an alternative application. Without modification, C-Flow could be applied to other problems involving variably-saturated water flow in a variety of structured porous media. Reactive transport simulations could also be performed for these media, although the transport equations would possibly need to be revised.

Results from C-Flow compared remarkably well with observations from a series of dumpster-scale moisture movement experiments. The model accurately represented the rapid breakthrough and gradual storage of water within waste-filled dumpsters for all eight experiments. The fluid-transfer coefficient was set to a higher level for compacted waste than for uncompacted waste to reflect the improved channel–bag coupling expected for compacted waste. All other model parameters were held constant amoung the eight simulations. The good agreement between the model and

experimental results suggested that the model captured the essence of flow through solid waste at the dumpster scale despite the many simplifications needed to formulate a tractable mathematical description of the flow processes.

Water application rate and waste compaction were key parameters influencing moisture flow through household waste at the dumpster scale. Both breakthrough time and water storage varied markedly with the infiltration rate. Breakthrough time increased from fifteen minutes to two days as the infiltration rate decreased from 25 to 3 mm/h. Accurate representation of the infiltration rate was shown to be necessary to properly simulate water flow at the higher infiltration rate. A cruder approximation was found to be adequate for infiltration of water at the lower rate. Waste compaction was shown to reduce the inter-bin variability and increase water storage.

It was not possible to determine a unique set of parameters that best described the experimental results. Different sets of model parameters produced practically identical simulation results. Any MSW flow parameters determined by inverse modeling should be applied to predictive models only with extreme caution. Site-specific parameters should be obtained by direct measurement whenever possible. Although C-Flow was not applied to any biodegradation experiments, similar cautions are likely to apply.

C-Flow was applied to two field-scale examples to illustrate its capabilities in the simulation of complex reactive transport problems. The model results compared well to observed field-scale behaviour using realistic biodegradation parameters and porous medium properties; however, the simulations were intended only to demonstrate C-Flow and not to guide landfill design or management decisions. Such applications require far more detailed field data than is currently available.

C-Flow did not predict much variation in overall biodegradation rates for various landfill site stabilization schemes, including pumping and recirculation of leachate. This low sensitivity was most likely caused by model limitations arising from a lack of experimental data. The model assumed homogeneous waste; in fact, the flow

properties and biodegradability of waste are typically highly heterogeneous. However, research that focuses on characterizing the large-scale structure of waste is needed before this heterogeneity can be quantified. An additional model limitation was the assumed linear relationship between moisture content and biodegradation rate. This constitutive relationship may have underpredicted the sensitivity of biodegradation rate to moisture content. Again, further experimental research is required in order to quantify the biodegradation rate–moisture content relationship.

This thesis has identified the need for further experimental research. Continued work at the dumpster scale is needed in order to improve the characterization of biodegradation processes in waste. These experiments should include as much detailed measurement as possible to identify the important factors controlling waste biodegradation. For example, this thesis highlighted the need to quantify the relationship between moisture content and biodegradation rate. These small-scale experiments will allow models such as C-Flow to be refined, improving their usefulness as landfill design and management tools.

The following specific parameters should be measured for small-scale moisture movement experiments:

- bulk saturated hydraulic conductivity;
- bulk moisture retention curves (drainage and wetting);
- bulk, channel, and matrix porosities; and
- matrix parameters (i.e., hydraulic conductivities and retention curves), if possible.

The above parameters should also be measured for future biodegradation experiments. The following additional parameters should also be measured:

- initial microbial population;
- microbial population versus time;

- DOC concentration versus time;
- gas production rates, as well as cumulative gas production; and
- trends of biodegradation rate as a function of moisture content.

Field-scale experiments are also required in order to determine the applicability of smaller-scale experimental results to actual landfill sites and to characterize the role of heterogeneity. These experiments will allow the conceptual models developed in this thesis to be tested and refined under more realistic conditions than can be obtained in the laboratory. The design of field-scale experiments is complicated by the extreme heterogeneity of MSW at the landfill scale and the difficulty in obtaining detailed data. However, since the large-scale structure of waste likely controls leachate movement and waste biodegradation at landfill sites, only studies at the landfill scale will be able to quantify the patterns of leachate movement and waste biodegradation.

Complete characterization of waste properties is not practical at the landfill scale. Instead, large scale experiments should likely focus on integrated, readily measured parameters. Some examples of measurable and potentially useful parameters are as follows:

- precipitation data;
- infiltration rates and volumes;
- discharge hydrographs for discrete points at the base of the waste;
- descriptive logs for any boreholes drilled in the waste;
- pumping test data, preferably with many observation points; and
- historical records of the general nature and distribution of waste types at the landfill site.

These parameters should help the development of practical models of overall landfill behaviour. These models will be site-specific, but patterns applicable for landfill sites in general may emerge.

Appendix A

Finite-Element Formulation

This appendix provides details of the finite-element formulation derived in this thesis. The primary-domain equations closely follow the standard Galerkin finite element technique. Numerous textbooks on the subject exist (e.g., Huyakorn and Pinder, 1983; Huebner and Thornton, 1982), so only the final matrix equations are presented. A more thorough derivation of the secondary-domain equations is presented because few numerical models employ spherical coordinates.

A.1 Primary Domain

A.1.1 Flow Elemental Matrices

The elemental conductance matrix for the one-dimensional line elements is

$$[H]^{(e)} = \left(\frac{dw\bar{k}_r K}{L}\right)^{(e)} \begin{bmatrix} 1 & -1 \\ -1 & 1 \end{bmatrix}. \tag{A.1}$$

The capacitance matrix is

$$[V]^{(e)} = \frac{(dwLS_s)^{(e)}}{2} \begin{bmatrix} S_{w1} & 0 \\ 0 & S_{w2} \end{bmatrix}. \tag{A.2}$$

The unsaturated storage matrix is

$$[U]^{(e)} = \frac{(dwL\theta)^{(e)}}{2} \begin{bmatrix} 1 & 0 \\ 0 & 1 \end{bmatrix}. \tag{A.3}$$

The superscript (e) denotes elemental values. The variables are d, the domain thickness in cartesian coordinates, or the effective circumference ($d = 2\pi r$) in axisymmetric coordinates, w, the line element width in the plane of the domain, and L, the element length. The elemental relative permeability, $\bar{k}_r$, is the arithmetic average of the nodal values unless it is upstream weighted, as discussed below. The nodal relative permeabilities are evaluated at the time levels defined by the nodal time-weighting factors. Equations A.2 and A.3 are written for the lumped mass formulation. The consistent mass formulation is also supported. For the consistent formulation, substitute

$$\frac{1}{6}\begin{bmatrix} 2S_{w1} & S_{w2} \\ S_{w1} & 2S_{w2} \end{bmatrix} \text{ for } \frac{1}{2}\begin{bmatrix} S_{w1} & 0 \\ 0 & S_{w2} \end{bmatrix}$$

and

$$\frac{1}{6}\begin{bmatrix} 2 & 1 \\ 1 & 2 \end{bmatrix} \text{ for } \frac{1}{2}\begin{bmatrix} 1 & 0 \\ 0 & 1 \end{bmatrix}.$$

The elemental conductance matrix for two-dimensional triangular elements is

$$[H]^{(e)} = \left(\frac{d\bar{k}_r}{4\Delta}\right)^{(e)} \left(K_{xx} \begin{bmatrix} b_1b_1 & b_1b_2 & b_1b_3 \\ b_2b_1 & b_2b_2 & b_2b_3 \\ b_3b_1 & b_3b_2 & b_3b_3 \end{bmatrix} + K_{zz} \begin{bmatrix} c_1c_1 & c_1c_2 & c_1c_3 \\ c_2c_1 & c_2c_2 & c_2c_3 \\ c_3c_1 & c_3c_2 & c_3c_3 \end{bmatrix} \right) \tag{A.4}$$

where (Huebner and Thornton, 1982)

$$b_1 = z_2 - z_3, \quad b_2 = z_3 - z_1, \quad b_3 = z_1 - z_2,$$
$$c_1 = x_3 - x_2, \quad c_2 = x_1 - x_3, \quad c_3 = x_2 - x_1,$$

z_i are the nodal z-coordinates, x_i are the nodal x-coordinates, and Δ is the elemental area. The capacitance matrix is

$$[V]^{(e)} = \frac{(d\Delta S_s)^{(e)}}{3} \begin{bmatrix} S_{w1} & 0 & 0 \\ 0 & S_{w2} & 0 \\ 0 & 0 & S_{w3} \end{bmatrix}^{j+1}. \tag{A.5}$$

The unsaturated storage matrix is

$$[U]^{(e)} = \frac{(d\Delta\theta)^{(e)}}{3} \begin{bmatrix} 1 & 0 & 0 \\ 0 & 1 & 0 \\ 0 & 0 & 1 \end{bmatrix}. \tag{A.6}$$

Equations A.5 and A.6 are written for the lumped mass formulation. For the consistent formulation, substitute

$$\frac{1}{12}\begin{bmatrix} 2S_{w1} & S_{w2} & S_{w3} \\ S_{w1} & 2S_{w2} & S_{w3} \\ S_{w1} & S_{w2} & 2S_{w3} \end{bmatrix} \text{ for } \frac{1}{3}\begin{bmatrix} S_{w1} & 0 & 0 \\ 0 & S_{w2} & 0 \\ 0 & 0 & S_{w3} \end{bmatrix}$$

and

$$\frac{1}{12}\begin{bmatrix} 2 & 1 & 1 \\ 1 & 2 & 1 \\ 1 & 1 & 2 \end{bmatrix} \text{ for } \frac{1}{3}\begin{bmatrix} 1 & 0 & 0 \\ 0 & 1 & 0 \\ 0 & 0 & 1 \end{bmatrix}.$$

The upstream-weighted elemental relative permeability is

$$\bar{k}_r = \sum_i \eta_i h_i \tag{A.7}$$

where the nodal weights, η_i, are given by

$$\eta_i = \eta_{bal} + \frac{h_i - \bar{h}}{\max(\Delta h_{min}, \Delta h)}, \tag{A.8}$$

where η_{bal} is the nodal weight for balanced relative permeability weighting ($\eta_{bal} = 1/2$ for line elements and $\eta_{bal} = 1/3$ for triangles), $\bar{h}$ is the elemental arithmetic average head, Δh is the hydraulic head variation within the element, and Δh_{min} is the threshold elemental head variation to cause full upstream weighting.

A.1.2 Flow Solution Iteration

Much of the following discussion was adapted from Huyakorn *et al.* (1984), Huyakorn and Pinder (1983) and Huebner and Thornton (1982). Let equation 3.2 be called $\{G\}$. The desired solution is thus

$$G_I(h_1, h_2, ..., h_J, ..., h_{nn}) = 0 \tag{A.9}$$

for all I. The next guess at the solution is obtained by performing a Taylor series expansion about the current approximation, ignoring all but the first order terms:

$$G_I^{i+1} = G_I^i + \left(\frac{\partial G_I}{\partial h_J}\right)^i \delta h_J^{i+1} = \epsilon_I^{i+1} \tag{A.10}$$

where $i+1$ denotes the newest guess at the solution, i denotes the previous guess, $\{\epsilon\}$ is the solution error vector and $\delta h_J^{i+1} = h_J^{i+1} - h_J^i$. Equation A.10 is solved at each iteration. The solution has converged for the time step when $\{\delta h\}$ vanishes to within some small tolerance.

The form of the derivative term in equation A.10 depends on whether or not the dependence of $[H]$ and $\{S_w\}$ on $\{h\}$ is included. Picard iteration ignores this dependence, whereas Newton-Raphson iteration retains it. For Picard iteration

$$\left(\frac{\partial G_I}{\partial h_J}\right)^i = \omega_J H_{IJ} + \frac{1}{\Delta t} V_{IJ} \tag{A.11}$$

For Newton-Raphson iteration

$$\left(\frac{\partial G_I}{\partial h_J}\right)^i = \omega_J H_{IJ} + \frac{1}{\Delta t} V_{IJ} + \frac{1}{\Delta t} U_{IJ} \left(\frac{\partial S_{wJ}}{\partial h_J}\right)^{j+1} + \left(\frac{\partial H_{IK}}{\partial h_J} h_K\right)^{j+\omega} \tag{A.12}$$

where, for line elements,

$$\left(\frac{\partial H_{1K}}{\partial h_J} h_K\right)^{j+\omega} = \omega_J \eta_J \left(\frac{\partial k_{rJ}}{\partial h_J}\right)^{j+\omega} \left(\frac{dwK}{L}\right)^{(e)} (h_1 - h_2)^{j+\omega} \tag{A.13}$$

and

$$\left(\frac{\partial H_{2K}}{\partial h_J} h_K\right)^{j+\omega} = \omega_J \eta_J \left(\frac{\partial k_{rJ}}{\partial h_J}\right)^{j+\omega} \left(\frac{dwK}{L}\right)^{(e)} (h_2 - h_1)^{j+\omega}. \tag{A.14}$$

For triangular elements,

$$\left(\frac{\partial H_{IK}}{\partial h_J} h_K\right)^{j+\omega} = \omega_J \eta_J \left(\frac{\partial k_{rJ}}{\partial h_J}\right)^{j+\omega} \left(\frac{d}{4\Delta}(K_{xx} b_I b_K + K_{zz} c_I c_K)\right)^{(e)} h_K^{j+\omega}. \tag{A.15}$$

The derivative $\partial S_w / \partial h$ is approximated by

$$\frac{\partial S_{wJ}}{\partial h_J} \simeq \frac{S_w(h^i) - S_w(h^{i-1})}{h^i - h^{i-1}} \tag{A.16}$$

unless h^i and h^{i-1} are nearly the same. In that case, the point derivative is used. The derivative $\partial k_r / \partial h$ is calculated by the same technique.

Newton-Raphson iteration usually converges much more quickly than Picard iteration. For small $\{\delta h\}$, Newton-Raphson iteration converges quadratically, whereas Picard iteration converges only linearly (Huyakorn and Pinder, 1983). However, as

shown in equations A.11 to A.15, the Newton-Raphson method requires approximately twice as many calculations as the Picard method for each iteration. Furthermore, the matrix generated by the Newton-Raphson method is asymmetric; the Picard method retains the symmetry of the finite-element formulation (Therrien, 1992; Huebner and Thornton, 1982). The ORTHOFEM v1.04 solver (Mendoza *et al.*, 1994) used by C-Flow solves both symmetric and asymmetric matrix equations, so the form of the global matrix is not important.

A.1.3 Transport Elemental Matrices

The advective-dispersive transport matrix for the one-dimensional line elements is (Frind, 1988) $[R] = [R_D] + [R_V]$ where

$$[R_D]^{(e)} = \left(\frac{dwD}{L}\right)^{(e)} \begin{bmatrix} 1 & -1 \\ -1 & 1 \end{bmatrix} \tag{A.17}$$

and

$$[R_V]^{(e)} = \left(\frac{qd}{2}\right)^{(e)} \begin{bmatrix} -1 & 1 \\ -1 & 1 \end{bmatrix}. \tag{A.18}$$

The mass storage matrix is

$$[T]^{(e)} = \frac{(dwL)^{(e)}}{2} \begin{bmatrix} \theta_{w1} & 0 \\ 0 & \theta_{w2} \end{bmatrix}^{j+1-\omega}. \tag{A.19}$$

The consistent mass formulation is also supported. For the consistent formulation, substitute

$$\frac{1}{6}\begin{bmatrix} 2\theta_{w1} & \theta_{w2} \\ \theta_{w1} & 2\theta_{w2} \end{bmatrix} \text{ for } \frac{1}{2}\begin{bmatrix} \theta_{w1} & 0 \\ 0 & \theta_{w2} \end{bmatrix}.$$

No reactions occur in the line elements, so $[M]$ and $\{P\}$ are not defined.

The dispersive transport matrix for two-dimensional triangular elements is

$$[R_D]^{(e)} = \left(\frac{d}{4\Delta}\right)^{(e)} \left(D_{xx} \begin{bmatrix} b_1b_1 & b_1b_2 & b_1b_3 \\ b_2b_1 & b_2b_2 & b_2b_3 \\ b_3b_1 & b_3b_2 & b_3b_3 \end{bmatrix} + D_{xz} \begin{bmatrix} b_1c_1 & b_1c_2 & b_1c_3 \\ b_2c_1 & b_2c_2 & b_2c_3 \\ b_3c_1 & b_3c_2 & b_3c_3 \end{bmatrix} \right.$$

$$+D_{zz}\begin{bmatrix} c_1b_1 & c_1b_2 & c_1b_3 \\ c_2b_1 & c_2b_2 & c_2b_3 \\ c_3b_1 & c_3b_2 & c_3b_3 \end{bmatrix} + D_{zz}\begin{bmatrix} c_1c_1 & c_1c_2 & c_1c_3 \\ c_2c_1 & c_2c_2 & c_2c_3 \\ c_3c_1 & c_3c_2 & c_3c_3 \end{bmatrix}\Bigg). \tag{A.20}$$

The advective transport matrix for is

$$[R_V]^{(e)} = \frac{q_x d}{6}\begin{bmatrix} b_1 & b_2 & b_3 \\ b_1 & b_2 & b_3 \\ b_1 & b_2 & b_3 \end{bmatrix} + \frac{q_z d}{6}\begin{bmatrix} c_1 & c_2 & c_3 \\ c_1 & c_2 & c_3 \\ c_1 & c_2 & c_3 \end{bmatrix} \tag{A.21}$$

The mass storage matrix is

$$[T]^{(e)} = \frac{(d\Delta)^{(e)}}{3}\begin{bmatrix} \theta_{w1} & 0 & 0 \\ 0 & \theta_{w2} & 0 \\ 0 & 0 & \theta_{w3} \end{bmatrix}^{j+1-\omega}. \tag{A.22}$$

The DOC production array is

$$\{P\}^{(e)} = (\bar{B}_a\kappa_a + \bar{B}_p\kappa_p)\frac{Y_C d\Delta}{3}\begin{Bmatrix} \theta_{w1} \\ \theta_{w2} \\ \theta_{w3} \end{Bmatrix}^{j+1-\omega}. \tag{A.23}$$

The DOC consumption matrix is

$$[M]^{(e)} = \frac{\left(\mu\bar{X}^j d\Delta\right)^{(e)}}{3(K_C + |\bar{C}|)}\begin{bmatrix} 1 & 0 & 0 \\ 0 & 1 & 0 \\ 0 & 0 & 1 \end{bmatrix}. \tag{A.24}$$

Equations A.22 and A.24 are written for the lumped mass formulation. For the consistent formulation, substitute

$$\frac{1}{12}\begin{bmatrix} 2\theta_{w1} & \theta_{w2} & \theta_{w3} \\ \theta_{w1} & 2\theta_{w2} & \theta_{w3} \\ \theta_{w1} & \theta_{w2} & 2\theta_{w3} \end{bmatrix} \text{ for } \frac{1}{3}\begin{bmatrix} \theta_{w1} & 0 & 0 \\ 0 & \theta_{w2} & 0 \\ 0 & 0 & \theta_{w3} \end{bmatrix}$$

and

$$\frac{1}{12}\begin{bmatrix} 2 & 1 & 1 \\ 1 & 2 & 1 \\ 1 & 1 & 2 \end{bmatrix} \text{ for } \frac{1}{3}\begin{bmatrix} 1 & 0 & 0 \\ 0 & 1 & 0 \\ 0 & 0 & 1 \end{bmatrix}.$$

A.2 Secondary Domain

The flow and transport equations used for the spherical secondary domain were derived using the Galerkin finite-element technique with linear basis functions. Line elements can be defined to represent pure radial flow in spherical coordinates. Unlike conventional line elements defined in a cartesian coordinate system, spherical line elements (one-dimensional spherical shell elements) have cross-sectional areas which vary along their length. Near the centre of a sphere, this variation is very large. Therefore, the variation in cross-sectional area along a single element is rigorously accounted for in the following derivation.

A.2.1 Flow Elemental Matrices

Fluid pressure head is the independent variable for flow in the secondary domain. The first step in the following derivation of the finite-element matrices is to write the partial differential equation for flow in a sphere (Equation 2.9):

$$-\frac{1}{r^2}\frac{\partial}{\partial r}\left(r^2 k_r' K' \frac{\partial \psi'}{\partial r}\right) + S_w' S_s' \frac{\partial \psi'}{\partial t} + \theta' \frac{\partial S_w'}{\partial t} = 0. \tag{A.25}$$

Next, the pressure head is substituted with a numerical approximation for each element:

$$\psi' \approx \tilde{\psi}' \tag{A.26}$$

where, for a linear spherical shell element,

$$\tilde{\psi}' = N_1 \tilde{\psi}_1' + N_2 \tilde{\psi}_2' \tag{A.27}$$

and

$$N_1 = \frac{r_2 - r}{r_2 - r_1}, \text{ and } N_2 = \frac{r - r_1}{r_2 - r_1}. \tag{A.28}$$

Next, the Galerkin technique is applied to the spatial derivative:

$$\zeta = \int_{r_1}^{r_2} -\frac{1}{r^2}\frac{\partial}{\partial r}\left(r^2 k_r' K' \frac{\partial \tilde{\psi}_j'}{\partial r}\right) N_i dV_{el}, \; i,j = 1,2 \tag{A.29}$$

where ζ is the error which needs to be minimized globally and $V_{el} = 4/3\pi(r^3 - r_1^3)$ is the volume of the spherical shell between r_1 and r. Therefore $dV_{el} = 4\pi r^2 dr$. Making this substitution in Equation A.29 and performing integration by parts to eliminate the second derivative leads to

$$\zeta = 4\pi \int_{r_1}^{r_2} r^2 k_r' K' \frac{\partial \tilde{\psi}_j'}{\partial r} \frac{\partial N_i}{\partial r} dr + Q_i' \tag{A.30}$$

$$\zeta = \frac{4\pi}{(r_2 - r_1)^2} \tilde{k}_r' K' \int_{r_1}^{r_2} r^2 dr \begin{bmatrix} 1 & -1 \\ -1 & 1 \end{bmatrix} \begin{Bmatrix} \tilde{\psi}_1' \\ \tilde{\psi}_2' \end{Bmatrix} + \begin{Bmatrix} Q_1' \\ Q_2' \end{Bmatrix} \tag{A.31}$$

where Q_i' is the boundary fluid flow rate at local node i. Globally, $\{Q'\}$ sums to zero, except on the outer domain boundary. Finally,

$$\zeta = [H']^{(e)} \begin{Bmatrix} \tilde{\psi}_1' \\ \tilde{\psi}_2' \end{Bmatrix} + \begin{Bmatrix} Q_1' \\ Q_2' \end{Bmatrix} \tag{A.32}$$

where

$$[H']^{(e)} = \frac{4\pi}{3} \frac{(r_2^3 - r_1^3)}{(r_2 - r_1)^2} \tilde{k}_r' K' \begin{bmatrix} 1 & -1 \\ -1 & 1 \end{bmatrix}. \tag{A.33}$$

which is the elemental conductance matrix for the second domain.

The derivation of the storage term follows the same procedure. The error which is to be minimized globally is defined by

$$\zeta = \int_{r_1}^{r_2} -\frac{1}{r^2} \left(\theta \frac{\partial S_w'}{\partial t} + S_w' S_s' \frac{\partial \psi'}{\partial t} \right) N_i dV_{el}, \quad i, j = 1, 2 \tag{A.34}$$

$$= 4\pi \left(\theta \frac{\partial \tilde{S}_{wj}'}{\partial t} + \tilde{S}_{wj}' S_s' \frac{\partial \tilde{\psi}_j'}{\partial t} \right) \int_{r_1}^{r_2} (N_1 + N_2) N_j r^2 dr. \tag{A.35}$$

Substitution of the relationships for N and integration leads to, for the lumped formulation,

$$\zeta = \frac{\pi}{3\Delta t} \begin{bmatrix} \left(r_2 \frac{r_2^3 - r_1^3}{r_2 - r_1} - 3r_1^3 \right) & 0 \\ 0 & \left(3r_2^3 - r_1 \frac{r_2^3 - r_1^3}{r_2 - r_1} \right) \end{bmatrix} \tag{A.36}$$

$$\times \begin{Bmatrix} \theta(\tilde{S}_{w1}'^{j+1} - \tilde{S}_{w1}'^{j}) + \tilde{S}_{w1}' S_s' (\tilde{\psi}_1'^{j+1} - \tilde{\psi}_1'^{j}) \\ \theta(\tilde{S}_{w2}'^{j+1} - \tilde{S}_{w2}'^{j}) + \tilde{S}_{w2}' S_s' (\tilde{\psi}_2'^{j+1} - \tilde{\psi}_2'^{j}) \end{Bmatrix}. \tag{A.37}$$

Therefore,

$$[V']^{(e)} = \frac{\pi S_s'}{3}\begin{bmatrix} \left(r_2\frac{r_2^3-r_1^3}{r_2-r_1} - 3r_1^3\right)\tilde{S}_{w1}' & 0 \\ 0 & \left(3r_2^3 - r_1\frac{r_2^3-r_1^3}{r_2-r_1}\right)\tilde{S}_{w2}' \end{bmatrix} \tag{A.38}$$

and

$$[U']^{(e)} = \frac{\pi\theta}{3}\begin{bmatrix} \left(r_2\frac{r_2^3-r_1^3}{r_2-r_1} - 3r_1^3\right) & 0 \\ 0 & \left(3r_2^3 - r_1\frac{r_2^3-r_1^3}{r_2-r_1}\right) \end{bmatrix}. \tag{A.39}$$

Similar equations could be derived for the consistent formulation.

A.2.2 Transport Elemental Matrices

The dispersive transport matrix is obtained directly by variable substitution in Equation A.33. The resulting elemental dispersion matrix equation is

$$[R_D']^{(e)} = \frac{4\pi}{3}\frac{(r_2^3 - r_1^3)}{(r_2 - r_1)^2}\tilde{D}'\begin{bmatrix} 1 & -1 \\ -1 & 1 \end{bmatrix}. \tag{A.40}$$

The elemental capacitance matrix equation is similarly obtained from Equation A.38:

$$[T']^{(e)} = \frac{\pi}{3}\begin{bmatrix} \left(r_2\frac{r_2^3-r_1^3}{r_2-r_1} - 3r_1^3\right)\theta_{w1}' & 0 \\ 0 & \left(3r_2^3 - r_1\frac{r_2^3-r_1^3}{r_2-r_1}\right)\theta_{w2}' \end{bmatrix}. \tag{A.41}$$

The advective transport matrix is defined by

$$[R_V']^{(e)} = \frac{\pi q}{3(r_2 - r_1)^2)}\begin{bmatrix} -(r_2^4 - r_1^4) & (r_2^4 - r_1^4) \\ -(r_2^4 - r_1^4) & (r_2^4 - r_1^4) \end{bmatrix}. \tag{A.42}$$

The volumetric DOC production array is

$$\{P'\}^{(e)} = \frac{4\pi}{r_2 - r_1}\theta_w' Y_C'(\bar{B}_a'\kappa_a' + \bar{B}_p'\kappa_p')\begin{Bmatrix} \frac{1}{12}r_2^4 - \frac{1}{3}r_2r_1^3 + \frac{1}{4}r_1^4 \\ \frac{1}{4}r_2^4 - \frac{1}{3}r_1r_2^3 + \frac{1}{12}r_1^4 \end{Bmatrix}. \tag{A.43}$$

The DOC consumption matrix is

$$[M']^{(e)} = \frac{4\pi}{r_2 - r_1}\frac{\mu'\bar{X}'^j}{3(K_C' + |\bar{C}|)}\begin{bmatrix} \frac{1}{12}r_2^4 - \frac{1}{3}r_2r_1^3 + \frac{1}{4}r_1^4 & 0 \\ 0 & \frac{1}{4}r_2^4 - \frac{1}{3}r_1r_2^3 + \frac{1}{12}r_1^4 \end{bmatrix}. \tag{A.44}$$

References

Arigala, S.G., Tsotsis, T.T., Webster, I.A., Yortsos, Y.C., and Kattapuram, J.J. 1995. Gas generation, extraction, and transport in landfills. *Journal of Environmental Engineering*, **121**(1), 33–44.

Attal, A., Akunna, J., Camacho, P., Salmon, P., and Paris, I. 1992. Anaerobic degradation of municipal wastes in landfill. *Water Science and Technology*, **25**(7), 243–253.

Barlaz, M.A., Schaefer, D.M., and Ham, R.K. 1989. Bacterial population development and chemical characteristics of refuse decomposition in a simulated sanitary landfill. *Applied and Environmental Microbiology*, **55**(1), 55–65.

Barlaz, M.A., Ham, R.K., and Schaefer, D.M. 1990. Methane production from municipal refuse: a review of enhancement techniques and microbial dynamics. *Critical Reviews in Environmental Control*, **19**(6), 557–584.

Bear, J. 1979. *Hydraulics of Groundwater*. New York: McGraw-Hill.

Bear, J., and Braester, C. 1987. Comments on "A three-dimensional finite-element model for simulating water flow in variably saturated porous media" by Peter S. Huyakorn et al. *Water Resources Research*, **23**(8), 1705–1706.

Bejan, A. 1993. *Heat Transfer*. Toronto: Wiley.

Brooks, R.H., and Corey, A.T. 1964. *Hydraulic Properties of Porous Media*. Fort Collins, Colorado: Colorado State University. Hydrology Paper No. 3.

Cassell, D.K., and Klute, A. 1986. *Methods of Soil Analysis, Part 1. Physical and Mineralogical Methods Agronomy Monograph no. 9.* Second edn. Madison: American Society of Agronomy Soil Science Society of America. Chap. 23. Water Potential: Tensiometry.

Celia, M.A., and Binning, P. 1992. A mass conservative numerical solution for two-phase flow in porous media with application to unsaturated flow. *Water Resources Research*, **28**(10), 2819–2828.

Celia, M.A., Bouloutas, E.T., and Zarba, R.L. 1990. A general mass conservative numerical solution for the unsaturated flow equation. *Water Resources Research*, **26**(7), 1483–1496.

Cooley, R.L. 1971. A finite difference method for unsteady flow in a variably saturated porous media: application to a single pumping well. *Water Resources Research*, **7**(6), 1607–1625.

Cooley, R.L. 1983. Some new procedures for numerical solution of variably saturated flow problems. *Water Resources Research*, **19**(5), 1271–1285.

Farquhar, G.J. 1989. Leachate: production and characterization. *Canadian Journal of Civil Engineering*, **16**(3), 317–325.

Fessenden, R.J., and Fessenden, J.S. 1986. *Organic Chemistry.* Third edn. Monterey, California: Brooks/Cole. 1129 pp.

Fetter, C.W. 1993. *Contaminant Hydrogeology.* New York: Macmillan Publishing Company.

Freeze, R.A., and Cherry, J.A. 1979. *Groundwater.* Toronto: Prentice-Hall.

Frind, E.O. 1982. Simulation of long-term transient density-dependent transport in groundwater. *Advances in Water Resources*, **5**(2), 73–88.

Frind, E.O. 1988. Solution of the advection-dispersion equation with free exit boundary. *Numerical Methods for Partial Differential Equations*, **4**(4), 301–313.

Gilmour, S.L. 1996. *Numerical Simulation of Hydrocarbon and Oxygen Transport and Microbial Biodegradation During Bioventing: Application to a Field Study and Sensitivity Analysis.* M.Sc. thesis, University of Alberta, Edmonton. 136 pp.

Gönüllü, M.T. 1994. Analytical modeling of organic contaminants in leachate. *Waste Management and Research*, **12**(2), 141–150.

Gurijala, K.R., and Suflita, J.M. 1993. Environmental factors influencing methanogenesis from refuse in landfill samples. *Environmental Science and Technology*, **27**(6), 1176–1181.

Hassanizadeh, S.M., and Gray, W.G. 1993. Thermodynamic basis of capillary pressure in porous media. *Water Resources Research*, **29**(10), 3389–3405.

Huebner, K.H., and Thornton, E.A. 1982. *The Finite Element Method for Engineers.* Second edn. Toronto: Wiley. 623 pp.

Huyakorn, P.S., and Pinder, G.F. 1983. *Computational Methods in Subsurface Flow.* Orlando, Florida: Academic Press.

Huyakorn, P.S., Thomas, S.D., and Thompson, B.M. 1984. Techniques for making finite elements competitive in modeling flow in variably saturated porous media. *Water Resources Research*, **20**(8), 1099–1115.

Huyakorn, P.S., Springer, E.P., Guvanasen, V., and Wadsworth, T.D. 1986. A three-dimensional finite-element model for simulating water flow in variably saturated porous media. *Water Resources Research*, **22**(13), 1790–1808.

HydroSOLVE. 1996. *AQTESOLV for Windows: User Guide Version 1.15.*

Jury, W.A., Gardner, W.R., and Gardner, W.H. 1991. *Soil Physics.* New York: Wiley.

Korfiatis, G.P., Demetracopoulos, A.C., Bourodimos, E.L., and Nawy, E.G. 1984. Moisture transport in a solid waste column. *Journal of Environmental Engineering*, **110**(4), 780–796.

Lee, J.J., Jung, I.H., Lee, W.B., and Kim, J.O. 1993. Computer and experimental simulations of the production of methane gas from municipal solid waste. *Water Science and Technology*, **27**(2), 225–234.

Lee, N., Kusuda, T., Shimaoka, T., Matsufuji, Y., and Hanashima, M. 1994. Pollutant transformations in landfill layers. *Waste Management and Research*, **12**, 33–48.

Lenhard, R.J., and Parker, J.C. 1987. A model for hysteretic constitutive relations governing multiphase flow: 2. Permeability-saturation relations. *Water Resources Research*, **23**(12), 2197–2206.

Lenhard, R.J., Parker, J.C., and Kaluarchchi, J.J. 1991. Comparing simulated and experimental hysteretic two-phase transient fluid flow phenomena. *Water Resources Research*, **27**(8), 2113–2124.

Marticorena, B., Attal, A., Camacho, P., Manem, J., Hesnault, D., and Salmon, P. 1993. Prediction rules for biogas valorisation in municipal solid waste landfills. *Water Science and Technology*, **27**(2), 235–241.

Mendoza, C.A., Therrien, R., and Sudicky, E.A. 1994. *ORTHOFEM User's Guide: Version 1.04*. Department of Geology, University of Alberta, Edmonton, Alberta. Internal Report.

Millington, R.J., and Quirk, J.P. 1961. Permeability of Porous Solids. *Transactions of the Faraday Society*, **57**, 1200–1207.

Moench, A.F. 1984. Double-porosity models for a fissured groundwater reservoir with fracture skin. *Water Resources Research*, **20**(7), 831–846.

Mualem, Y. 1976. A new model for predicting the hydraulic conductivity of unsaturated porous media. *Water Resources Research*, **12**(3), 513–522.

Neuman, S.P. 1974. Effect of partial penetration on flow in unconfined aquifers considering delayed response of the water table. *Water Resources Research*, **10**(2), 303–312.

Nozhevnikova, A.N., Nekrasova, V.K., Lebedev, V.S., and Lifshits, A.B. 1993. Microbial processes in landfills. *Water Science and Technology*, **27**(2), 243–252.

Oweis, I.S., Ellwood, R.B., and Greene, D.S. 1990. Hydraulic characteristics of municipal refuse. *Journal of Geotechnical Engineering*, **116**(4), 539–553.

Owens, J.M., and Chynoweth, D.P. 1993. Biochemical methane potential of municipal solid waste (MSW) components. *Water Science and Technology*, **27**(2), 1–14.

Parker, J.C., and Lenhard, R.J. 1987. A model for hysteretic constitutive relations governing multiphase flow: 1. saturation-pressure relations. *Water Resources Research*, **23**(12), 2187–2196.

Ross, W.R. 1990. Factors influencing the chemical characteristics of landfill leachates. *Water-S.A.*, **16**(4), 275–280.

Rowe, R.K., and Nadarajah, P. 1996. Estimating leachate drawdown due to pumping wells in landfills. *Canadian Geotechnical Journal*, **33**(1), 1–10.

Spiegel, M.R. 1968. *Mathematical Handbook of Formulas and Tables*. Toronto: McGraw-Hill. 271 pp.

Springer, E.P., Huyakorn, P.S., Guvanasen, V., and Wadsworth, T.D. 1987. Reply to comments on "A three-dimensional finite-element model for simulating water flow in variably saturated porous media" by Peter S. Huyakorn et al. *Water Resources Research*, **23**(8), 1707.

Theis, C.V. 1935. The relation between the lowering of the piezometric surface and the rate and duration of discharge of a well using groundwater storage. *Transactions of the American Geophysical Union*, **2**, 519–524.

Therrien, R. 1992. *Three-Dimensional Analysis of Variably-Saturated Flow and Solute Transport in Discretely-Fractured Porous Media*. Ph.D. thesis, University of Waterloo, Waterloo. 136 pp.

Uguccioni, M., and Zeiss, C. 1997. Comparison of two approaches to modeling moisture movement through municipal solid waste. *Journal of Environmental Systems*, **25**(1), 41–63.

Uguccioni, M.A. 1995. *Moisture Movement Through Municipal Solid Waste*. M.Sc. thesis, University of Alberta, Edmonton. 157 pp.

van Genuchten, M.T. 1980. A closed-form equation for predicting the hydraulic conductivity of unsaturated soils. *Soil Science Society of America Journal*, **44**(5), 892–898.

van Genuchten, M.T. 1981. Analytical solutions for chemical transport with simultaneous adsorption, zero-order production and first-order decay. *Journal of Hydrology*, **49**(3-4), 213–233.

Wall, D.K., and Zeiss, C. 1995. Municipal Landfill Biodegradation and Settlement. *Journal of Environmental Engineering*, **121**(3), 214–224.

Warren, J.E., and Root, P.J. 1963. The behavior of naturally fractured reservoirs. *Society of Petroleum Engineers Journal*, **3**, 245–255.

Waterloo Hydrogeologic. 1994. *PRINCE: User Guide Version 3.0*. Princeton Analytical Models of Flow and Mass Transport.

Westlake, K., Archer, D.B., and Boone, D.R. 1995. Diversity of cellulolytic bacteria in landfill. *Journal of Applied Bacteriology*, **79**, 73–78.

Winter, T.C. 1983. The interaction of lakes with variably saturated porous media. *Water Resources Research*, **19**(5), 1203–1218.

Zeiss, C., and Major, W. 1993. Moisture flow through municipal solid waste: patterns and characteristics. *Journal of Environmental Systems*, **22**(3), 211–231.